Nanobeam Cavities for Reconfigurable Photonics

Thesis advisor: Marko Lončar Parag B Deotare

Nanobeam cavities for Reconfigurable Photonics

Abstract

We investigate the design, fabrication, and experimental characterization of high quality factor photonic crystal nanobeam cavities, with theoretical quality factors of 1.4×10^7 in silicon, operating at $\sim 1550\,nm$. By detecting the cross-polarized resonantly scattered light from a normally incident laser beam, we measure a quality factor of nearly 7.5×10^5. We show on-chip integration of the cavities using waveguides and an inverse taper geometry based mode size converters, and also demonstrate tuning of the optical resonance using thermo-optic effect.

We also study coupled cavities and show that the single nanobeam cavity modes are coupled into even and odd superposition modes. Using electrostatic force and taking advantage of the highly dispersive nature of the even mode to the nanobeam separation, we demonstrate dynamically reconfigurable optical filters tunable continuously and reversibly over a $9.5\,nm$ wavelength range. The electrostatic force, obtained by applying bias voltages directly to the nanobeams, is used to control the spacing between the nanobeams, which in turn results in tuning of the cavity resonance. The observed tuning trends were confirmed through simulations that modeled the electrostatic actuation as well as the optical resonances in our reconfigurable geometries.

Finally we demonstrate reconfiguration of coupled cavities by using optical gradient force induced mechanical actuation. Propagating waveguide modes that exist over wide wavelength range are used to actuate the structures and in that way control the resonance of a localized cavity mode. Using this all-optical approach, more than 18 linewidths of tuning range is demonstrated. Using an on-chip temperature self-referencing method that we developed, we determined that 20% of the total tuning was due to optomechanical reconfiguration and the rest due to thermo-optic effects. By operating the device at frequencies higher than the thermal cut-off, we show high speed operation dominated by just optomechanical effects. Independent control of mechanical and optical resonances of our structures, by means of optical stiffening, is also demonstrated.

Contents

Listing of figures

To my parents, Saroj and Bhaskar Deotare
and my wife, Rama Thakar

Acknowledgments

First and foremost, I would like to thank my academic advisor, professor Marko Lončar for his guidance, patience and support throughout my stay at Harvard. He not only gave me freedom to choose my dissertation area but also created a healthy environment where ideas could flourish without worrying about any financial or time constraints. Marko's benevolence, which extends beyond scientific research, and vision, have truly shaped my thinking and approach towards life. I truly appreciate Marko's jovial and generous nature. Working with him during the initial years to setup the lab was a memorial experience, and I am really grateful to him for valuing my thoughts and respecting my decisions. He has taught me to respect every small idea, and my learnings from him throughout my stay at Harvard go much beyond science.

I will cherish, my five years at Harvard throughout my life. I truly enjoyed the classes, labs and my interaction with great intellectual minds. In particular, it was a pleasure to interact with professor Federico Capasso, professor Evelyn Hu and professor Joost Vlassak and I have greatly benefited from their insights. I am also thankful to Federico for his guidance regarding my career. Thanks are also due to my colleagues who over the period became my close friends. I thank

them for all the enjoyable discussions and great time I spent with them. In particular, I would like to thank Dr. Irfan Bulu, Dr. Murray McCutcheon, Qimin Quan and Yinan Zhang for helping me out with the designs and simulations. I am also thankful to Dr. Mughees Khan and Ian Frank for their help with nano-fabrication. I would also like to thank my friends Jennifer Choy, Raji Shankar, Birgit Hausmann, Ian Burgess, Pui-Chuen Hui, Leonard Kogos and Tom Babinec for their help through out my stay at Harvard. It has been a pleasure to work with all of you and an honor to be your friend. Thanks to all the staff at Harvard's Center for Nanoscale System, especially Dr. Jiangdong Deng, Yuan Lu, Ling Xie, Noah Clay, John Tsakirgis and Dave Lange for their help through out my tenure at Harvard.

Outside Harvard, I am thankful to professor Franz Kaertner for his valuable insights. I also thank Rob Ilic for his help resolving my fabrication crisis. Thanks are also due to my past teachers, especially my primary and high school director, Commodore Lauji Mehta (J. N. Petit Technical High School, Pune), who taught me the importance of discipline in life, professor B. N Chaudhari (Govt. College of Engineering, Pune), for his guidance in the earlier part of my life and professor Jun Kameoka, for his support and guidance at Texas A & M university. I thank all my friends, relatives, and well wishers for their support.

Last but not the least, I thank my family. My parents, who have been my inspiration and have always supported, helped and stood by me through out my life. My father, who taught me to dream and it's today that I see its importance, my mother, in believing in me and my wife, for her love, patience and constant support. This thesis is for them.

Cambridge, 11th May 2012

I learnt that successful optical experiments
require good focus and alignment,
of light as well as mind

1 Introduction

THE LAST CENTURY experienced a revelation in communications with the invention of optical fibers and lasers. The idea to use photons instead of electrons as a medium to transfer information over long distances at high speed became realistic, and a new area of research emerged as industry and researchers explored various ways to

manipulate light. Advances in active and passive optical components revolutionized communications as physical distances no longer hindered knowledge transfer. Today, long distance communication is dominated by optical fibers, the best optical waveguides known to man, which allow information to be efficiently transfered at rates higher than $40\,Gbits/s$. However, short distance communication is still dominated by electrons and information is transfered using copper wires (interconnects). Ohmic losses in these wires account for more than 50 % of the consumed energy causing excessive heating. Poor heat dissipation capabilities due to high device densities, limits the speed of operation to a few GHz. This last mile problem has forced researchers to actively look for alternatives. For the past decade, researchers have been looking into optical interconnects as an efficient alternative for copper interconnects. Optical interconnects not only reduce ohmic losses but also allow for large operation bandwidth and can take advantage of wavelength division multiplexing (WDM) technique to transfer information at an extremely high rate.

Short distance communication can be divided into two parts (i) between two processing units (example: in a computing cluster) and (ii) between multiple cores of a processor (on-chip). Enormous effort to cost effectively implement the matured technology used for long distance communication to solve the former issue is underway. However the latter demands new breakthroughs in technology due to

its on-chip requirements. These optical interconnects require on-chip, integrable passive and active optical devices like light sources, waveguides, amplifiers, filters, modulators, routers, switches, etc. which will allow for on-chip manipulation of light. This on-chip manipulation of light is of great importance not only for data communications and optoelectronics, but also applications in nonlinear optics, biochemical sensing and cavity quantum electrodynamics (QED).

1.1 Microcavities

Optical resonators enhance the probability of light-matter interaction due to their ability to store photons for many optical cycles [1], which makes them indispensable for sensing and cavity QED applications. The ability to store photons however, also allows to design filters, routers, modulators, delay lines, memory and switches which can find their use in optical interconnects. Due to the ability to confine light in small areas and the advancement of microfabrication technology, optical resonators can be shrunk to micron scale. These optical microcavities are ideal for on-chip manipulation of light. Our work reported in the following chapters, is based on an high quality factor (Q), small mode volume nanobeam optical resonator.

Quality factor is a dimensionless quantity used to characterize a resonator's or oscillator's bandwidth centered around its resonant

frequency. It relates the rate of loss of energy to the stored energy inside a resonator. Hence a high Q resonator stores energy for longer period of time and has a smaller bandwidth compared to a low Q resonator. High Q makes it ideal for its use as a filter. If one can implement a method to reconfigure such a filter, it will not only be useful for switching applications, like signal routing and modulation, but also serve as a wavelength trimming technique. Compared to electronic devices, optical devices are far more sensitive to fabrication tolerances making post fabrication trimming mandatory for their operation. Various trimming or reconfiguration methods based on thermo-optic [2–4] , free carrier injection [5], electromechanical and optomechanical effects have been proposed and studied. Due to the mechanical flexibility of our devices, we will look into electromechanical and optomechanical [6–14] based effects to mechanically deform and reconfigure the optical resonator. Electromechanical based reconfiguration is extremely efficient since it requires zero hold power (the power to hold the device in a reconfigured state) while optomechanical reconfiguration allows for faster operation speeds with no additional footprint requirements. At the same time, both the techniques have negligible effect on the Q of the devices, which is an important desirable merit for reconfiguration technique.

Our aim is to design devices useful for optical interconnects,

keeping in mind technologically relevant issues. Data processing capability, ease of information access and storage makes electronics indispensable. Given this and the robust silicon technology, an alternative based on silicon disruptive technology will be hard to be absorbed in the semiconductor industry and hence we have used silicon as the material for our devices. Real estate for on-chip devices is also expensive and has been an additional motivation for exploring optomechanics based reconfiguration as it does not require additional footprint area for contact electrodes, needed in the case of free carrier or electromechanical based techniques.

Chapter 2 talks about the design, fabrication and characterization of a photonic crystal nanobeam cavity (PCNC). On-chip integration using waveguides is also discussed in the chapter. We also look into coupled cavity structures as two of the reconfiguration principles discussed later are based on the dispersion of the cavity resonance on the separation of the two coupled cavities. We also demonstrate an on-chip spectrometer as a potential application of PCNC, using thermo-optic effect based reconfiguration.

Chapter 3 discusses reconfiguration of the devices using electrostatic forces. This reconfiguration technique is ideal as a post trimming technique as it requires negligible hold power.

Finally, in Chapter 4 we discuss reconfiguration using optomechanical effects. Here we not only look into static

reconfiguration but also dynamic reconfiguration and demonstrate its use in signal routing and modulation. Using novel on-chip temperature sensing scheme we estimate the contribution of optomechanical effects to the total reconfiguration of the system. We also show that independent control over optical and mechanical properties of the device can be achieved using optomechanical reconfiguration.

Bragg taught me,

not to worry about obstacles in life

since they are periodic, I really wouldn't see them

2

Photonic Crystal Nanobeam Cavities

TRAVELING-WAVE BASED RESONATORS, and micro-toroid resonators in particular, have been used to achieve some of the largest $Q's$ to date [1]. However, for many applications involving

processes like spontaneous emission, nonlinear optical processes and strong coupling, figure of merit is proportional to the ratio between resonator's Q and mode volume (V_{mode}), which can be quite large in traveling-wave geometries. Higher Q/V_{mode} is desired to improve light matter interactions. Therefore, standing-wave optical resonators, capable of having very small mode volume, have been explored as an attractive alternative [1]. These structures, based on a Fabry-Perot geometry, typically consist of the region in which light can propagate (e.g. an optical waveguide), terminated at both its ends with optical mirrors. The mirrors are often in the form of $1D$ Bragg mirror, as in the case of vertical cavity surface emitting laser (VCSEL). Bragg mirrors are periodic structures in which the refractive index varies with quarter wavelength periodicity. In 1987 Bragg mirror idea (periodic variation of refractive index) was extended to $3D$ by Yablonovitch [15] and John [16] who proposed $3D$ photonic crystals as a platform suitable for realization of ultimate cavities with wavelength-scale mode volumes, ultra-high Qs and a complete bandgap and hence perfect reflectivity in all directions. Unfortunately, fabrication of these $3D$ periodic optical structures has proven to be challenging and in spite of great effort no ultra-high Q small mode volume cavity based on $3D$ photonic crystals has been realized to date. This prompted researchers to consider alternative approaches, based on lower-dimensionality photonic crystals. In

particular, planar photonics crystals, based on $2D$ periodic lattices realized in thin semiconductor membranes [17] received considerable interest due to the ease of fabrication and compatibility with standard planar micro-fabrication technology. State of the art fabrication, combined with creative cavity designs, have resulted in wavelength scale optical cavities with $Q > 10^6$ (experimental) and Q/V_{mode} values larger than traveling wave resonators.

Recently, it has been demonstrated that photonic crystals with even lower dimensionality, resembling some of the early distributed feedback (DFB) cavity designs, can be used to realize cavities with performance rivaling and even outperforming those based on $2D$ planar photonic crystals. These photonic crystal nanobeam cavities (PCNCs), based on chirped 1-D optical lattices, also have physical footprint which is exactly the same as that of an optical waveguide and therefore represent the smallest cavity geometry that can be made using dielectric materials only [18–22]. Furthermore, nanobeams enable realization of high-Q small-V_{mode} cavities even in low index materials (e.g. SiO_2, polymers) [23, 24] thus vastly increasing the library of photonic materials suitable for realization of ultra-high Q/V_{mode} cavities. This is because one dimensional periodic structures with an index contrast always have a bandgap, which might not exist for 2D and 3D structures with low index contrast. The near-field of PCNC cavities is highly accessible which allows for easy light material

interaction which is useful for sensing [23], optical trapping [25] and optomechanics [6, 7]. PCNCs can be easily and naturally integrated with optical waveguides for efficient delivery of light [20, 26]. Cavities that support ultra-high Q modes with both TE and TM polarization [27] can be easily realized. All of these features, many of which are hard to achieve using $2D$ photonic crystals, make photonic crystal nanobeam cavities an ideal platform for practical applications.

2.1 Design

2.1.1 Iterative Approach

The idea of waveguide based micro-cavities has been around for more than fifteen years. It was first proposed at MIT [28] in 1995 and then experimentally realized two years later [29] . The device consisted of a waveguide segment surrounded with two lattices of holes that played the role of Bragg mirrors. Light trapping was achieved in the system via combination of Bragg scattering (in longitudinal direction) and total internal reflection (in two transverse directions), resulting in an optical resonance. The theoretical value of Q was calculated to be 280 whereas the experimentally measured value was 265 (Fig. 1c). Such a low value of Q was due to the sub-optimal design. In particular, light scattering at the interface between the Bragg mirror and the central cavity region, due to the mismatch in the effective mode indices of the

two regions, was responsible for low Q.

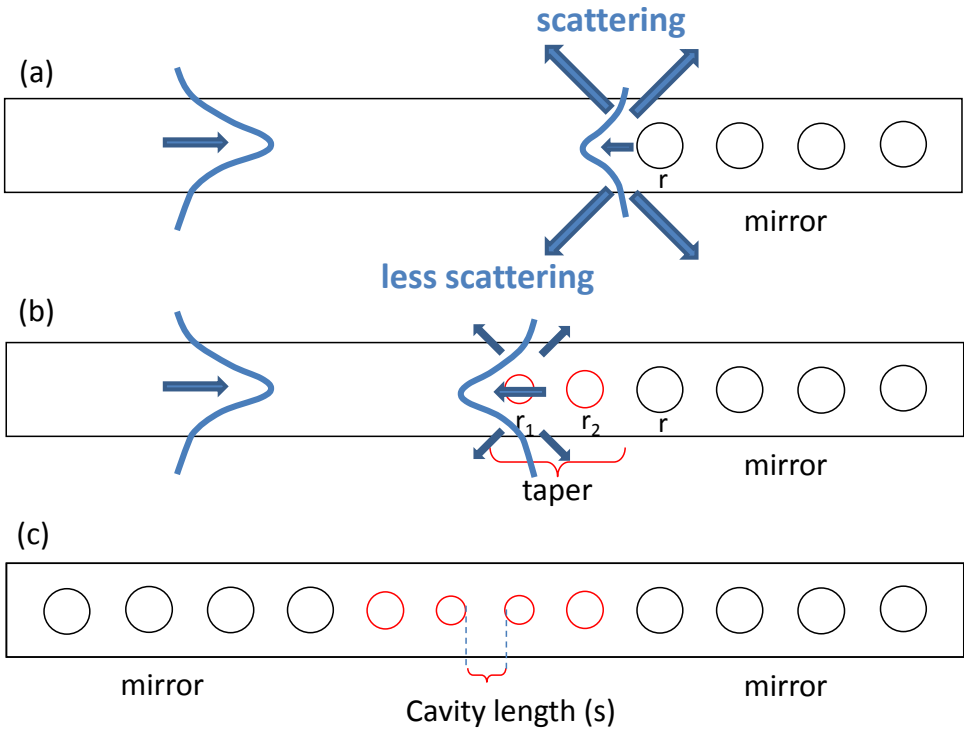

Figure 2.1.1: Light scattering at waveguide-mirror interface.(a) and (b) Schematic showing the reduced scattering loss due to tapering of holes. (c) Photonic crystal nanobeam cavity formed by using two tapered mirrors.

Conceptually, the cavity can be viewed as a wavelength-scale Fabry-Perot cavity with photonic crystal mirrors, which reflect and thus trap the nanobeam waveguide mode. Because the cavity mode penetrates some distance into the mirror, it is crucial that the fields do not abruptly terminate at the mirror boundary, as this would lead to considerable scattering loss. In order to increase the Q of the cavity it is necessary to taper the propagating mode of the cavity region into

the exponentially decaying mode of the Bragg mirror [21, 30]. This mode matching, analogous to the impedance matching problem in electronics, can be achieved using a multi-hole taper towards the cavity (refer Fig. 2.1.1) [30]. By doing so, the waveguide mode index can slowly be reduced to match the Bragg index which significantly reduces the scattering and provides exponential increase in cavity Q, at an expense of slight, linear, increase in the cavity mode volume. By increasing the number of holes used in the taper, near adiabatic conversion between the two modes could be achieved. By putting two such engineered, tapered (chirped) mirrors back to back, ultra high-Q cavity could be realized (refer Fig. 2.1.1c). The effect of tapered holes on the Q and mode volume was first studied in the silicon nitride material system for operation in visible [21]. It was seen that drastic increase in Q could be achieved for an optimal value of the cavity length (s) (refer Fig. 2.1.1c), defined as the distance between two central holes in the structure. The Q values depended strongly on the precise cavity length (this is due to dependence of scattering loss on the cavity length. This can also be viewed as an effect for satisfying the fabry perot cavity resonance condition), which puts stringent requirement on the fabrication quality needed for the realization of ultra-high Q cavities.

The design process consists of engineering three elements: (a) the photonic crystal mirror, (b) the taper, and (c) the cavity length. A

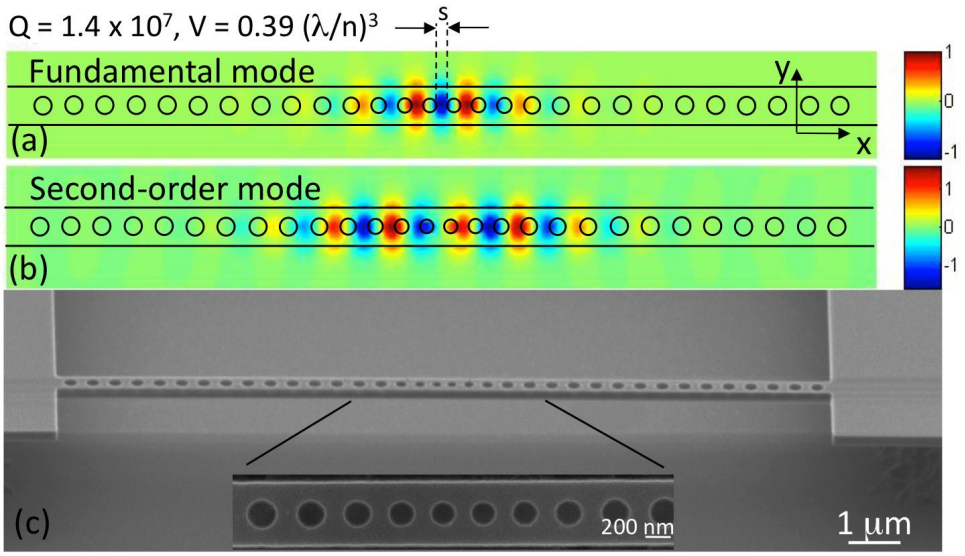

Figure 2.1.2: Mode profile and SEM image of cavity designed using iterative method. (a) and (b) Mode field profile of the first and second order mode. (c) SEM image of the fabricated structure in silicon.

free-standing silicon nanobeam of thickness 220 nm (constrained by our experimental wafer) and width 500 nm supporting a TE mode was chosen. The cavities were designed using the three-dimensional finite-difference time-domain method (Lumerical Solutions, Inc.). The photonic crystal mirror parameters, namely the hole spacing $a = 430\,nm$ and radius $r = 0.28a$, were chosen to center the resulting stop-band around the wavelength of interest ($\sim 1550\,nm$). The reflectivity of the mirror was characterized by launching a waveguide mode pulse and monitoring the reflection spectrum. The 1D photonic band gap extended from 1200-1700 nm. For the taper section, we incorporate a five-hole linear taper. With the tapered mirrors designed to minimize reflection loss from the incident lowest-order

waveguide mode, the cavity length was scanned to optimize the Q of the fundamental cavity mode. The Q was calculated by the definition $Q = \omega_0(Energy\ stored/Power\ loss)$ and was validated in the lower Q structures by monitoring the time-domain ring down of the simulated fields. The optimal structure supported a fundamental mode at $\lambda = 1560\,nm$ with a Q of 1.4×10^7 and an ultrasmall mode volume of $V = 0.39(\lambda/n)^3$. The mode profiles is plotted in Fig 2.1.2a. The cavity also supports higher order modes with different symmetries, one of which is shown in Fig 2.1.2b and which has a reasonable Q of 120000 and mode volume $V = 0.71(\lambda/n)^3$.

2.1.2 Deterministic Approach

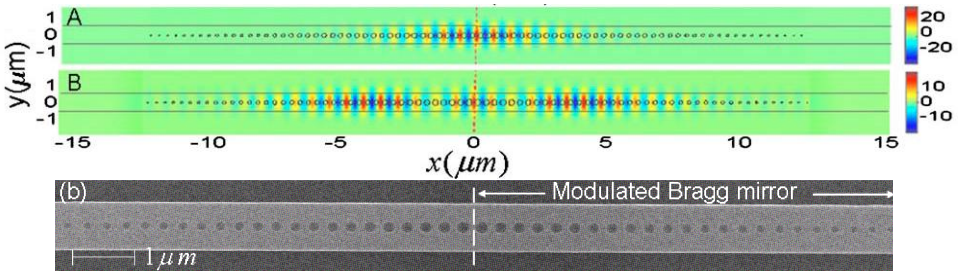

Figure 2.1.3: Mode profile and SEM image of cavity designed using deterministic method. (a) and (b) Mode field profile of the first and second order mode. (c) SEM image for a fabricated device

There have been quite a few variations in the design of the periodic structure of the ultra-high Q nanobeam cavity, including ladder cavities [31] with rectangular holes, bookshelf/domino structures [31], and parabolic width-taper cavity [32]. However, the working principle

of all of these approaches is the same and is based on efficient effective index matching between cavity and mirror regions. Another common feature of all the different design strategies is that they involve extensive parameter search (taper hole radii, cavity length, etc) and trial-and-error based optimization in order to find the optimal taper profile (the radius and spacing of the holes in the taper section). To overcome these limitations and streamline the design process, thus significantly reducing the time needed for the design of ultra-high Q structures, a deterministic method to design ultrahigh Q cavities has recently been proposed and experimentally demonstrated [26, 33]. This approach not only gets rid of trial-and-error based shifting and resizing of holes, but also results in cavities that feature high transmission at the cavity resonance: $Q > 10^7$ with transmission of 97 % [33]. The key design rules for this approach are: (i) a Gaussian-like field attenuation profile, provided by linear increase in the mirror strength. This is because, the energy of spatial harmonics within the light cone is minimized (i.e., the Q maximized) if the field attenuation inside the mirror has a Gaussian shape. Mode field profiles for such a cavity is shown in Fig. 2.1.3.(ii) zero cavity length, because the energy of spatial harmonics within the light cone is minimized at $s = 0$ and (iii) constant length of each mirror segment (period=a) to achieve a increasingly linear mirror strength. In contrast to earlier iterative design (Fig. 2.1.2), these cavities consist of

air holes with decreasing radii which allows for high transmission at an expense of slightly larger mode volume.

2.2 Ultra High-Q Photonic Crystal Nanobeam Cavities

In order to validate the designs, devices were fabricated in a silicon-on-insulator (SOI) material platform using state of the art nanofabrication technology (for fabrication details, please refer to the Appendix). SEM images of the fabricated structure for cavities designed with the iterative and deterministic approaches described earlier are shown in Fig. 2.1.2c and Fig. 2.1.3c respectively. The cavities designed using the iterative approach were probed using a free space cross polarization technique (the deterministic cavities were probed using butt coupling technique discussed later in the chapter) popularly known as resonance scattering (refer to the Appendix). This technique is relatively straightforward to implement but suffers from poor in- and out-coupling of light in particular in the case of high-Q cavity modes. The experimental results are shown in Fig. 2.2.1. We expect that as the cavity becomes longer, the resonance should redshift due to the increase in the effective index of the cavity. This behavior is well modeled by our simulations, and we see a similar overall trend in our experimental results shown in Fig. 2.2.1c.

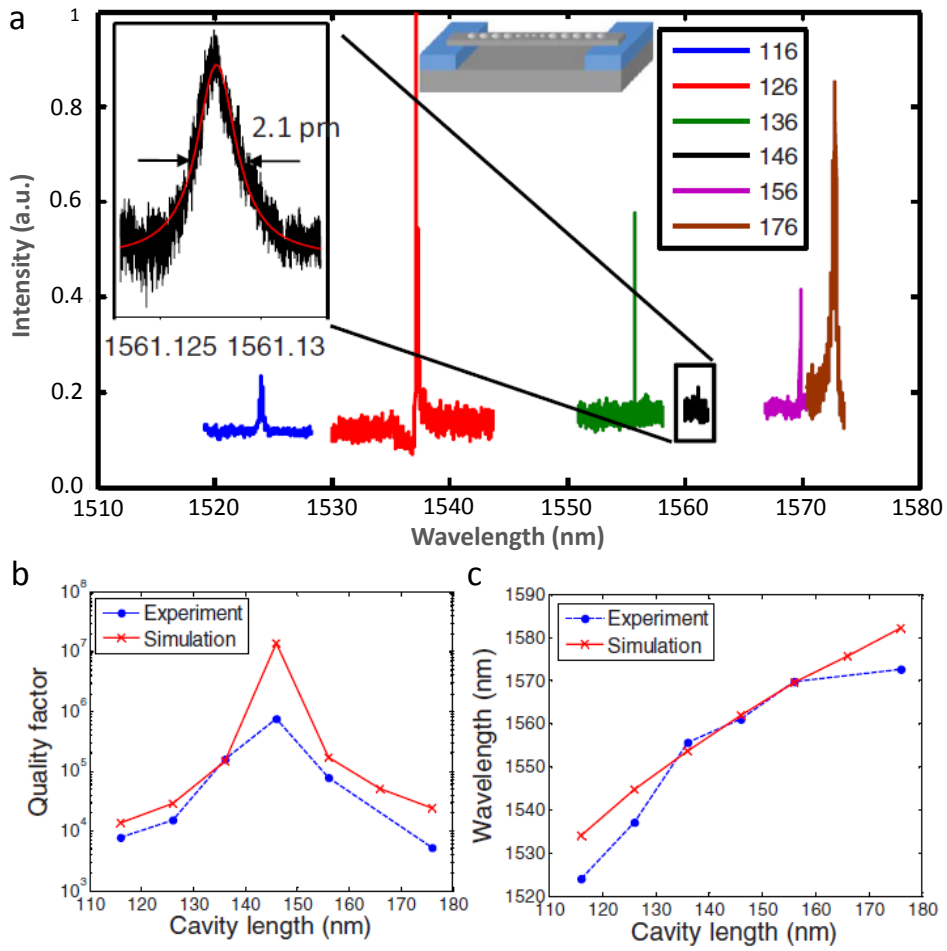

Figure 2.2.1: Experimental results for suspended single cavity system. (a) Resonant scattering spectra for a range of cavity lengths ($s = 116 - 176\,nm$) normalized by a background spectrum taken on the beam away from the cavity. (b) Measured and simulated ($Q's$) as a function of cavity length (s). (c) Mode resonance wavelength as a function of s.

Detailed investigation of fabricated structures using scanning electron microscopy (SEM) revealed that deviations from theoretical results can be attributed to fabrication-related disorders, and in particular to proximity effects during e-beam lithography. The cavity Q also follows the predicted trend. As expected, for large and small s, the Q is modest ($Q < 10000$), and it reaches a record high value of $Q = 750000$ when $s = 146\,nm$. We also found that the cavity resonance was very sensitive to the excitation location, and disappeared with submicron displacements of the cavity. This is consistent with the expected small mode volume of our cavities. We fabricated a range of structures with scaled dimensions $-6\,\%, -3\,\%, +3\,\%, +6\,\%$ to account for imperfections introduced during fabrication and to effectively bracket the design parameters. We found that the structures scaled by $-3\,\%$ most closely matched our simulations, and the spectra from these cavities are the ones presented in Fig. 2.2.1a. It is interesting to note that cavities with a higher Q were more difficult to characterize using our resonant-scattering setup as a result of the reduced contrast between the resonant feature and the coherent nonresonant background, which is possibly due to the stronger photon confinement.

We also tested the nanobeam resonators before the final release HF vapor etch (HFVE) step. Nonsuspended on-substrate cavities are more robust and are suitable for such applications as sensing and operation in fluids. Figure 2.2.2 shows the experimental results for

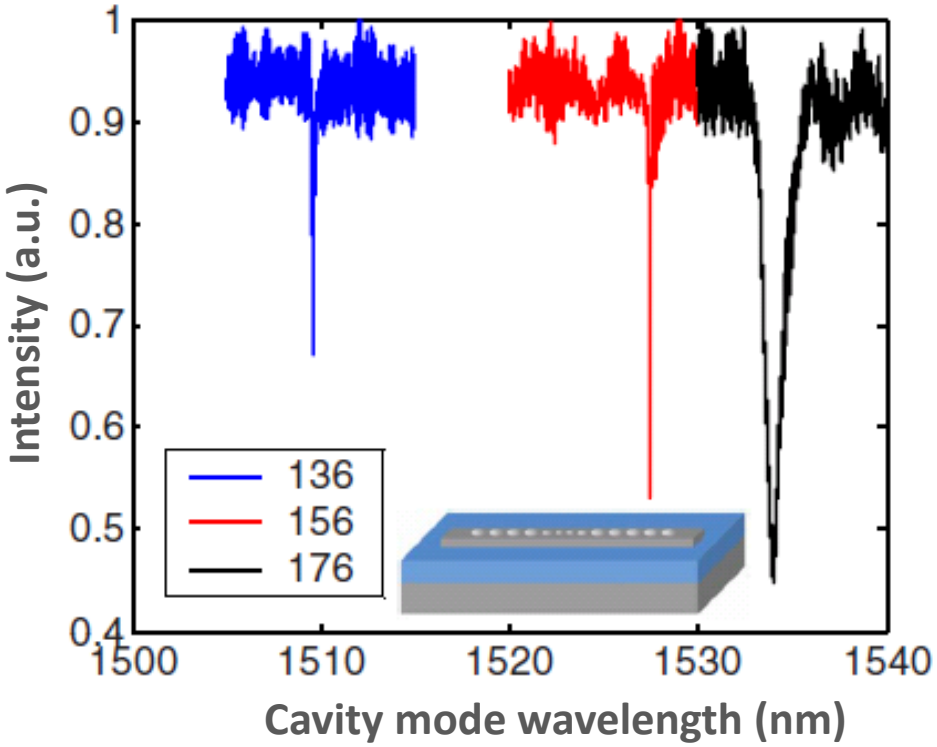

Figure 2.2.2: Resonant scattering spectra for on-substrate single cavity system (not undercut). The $Q's$ are 18000, 27500, and 17000 for the $s = 136, 156,$ and $176\,nm$ cavities, respectively.

several resonator designs with varying cavity spacing, s, taken before the cavities were released from the substrate. The highest Q that we were able to obtain was 27500 for a cavity with $s = 156\,nm$. Higher Q results have been previously reported in different on-substrate PCNC. We note, however, that our cavities were optimized for free-standing operation, and therefore the modest $Q's$ are not surprising.

2.3 High-Q Transverse Electric/Transverse Magnetic Cavities

PCNCs can be engineered to have both transverse electric (TE) and transverse magnetic (TM) stopbands [34], provided the nanobeam is thick enough to support TM guided modes. High Q cavity modes can be designed for both polarizations simultaneously by using an appropriate lattice tapering. By tuning the aspect ratio of the nanobeam (namely the height and width), the energy separation of the modes can be tuned. Dual-polarized nanocavities have many potential applications in chip-scale nonlinear optics. In particular, systems for single-photon frequency conversion in III-V materials [35, 36]. These devices also raise the intriguing prospect of photonic crystal quantum cascade lasers for which the radiation is TM-polarized.

PCNCs can be designed to have both TE and TM modes with Q's

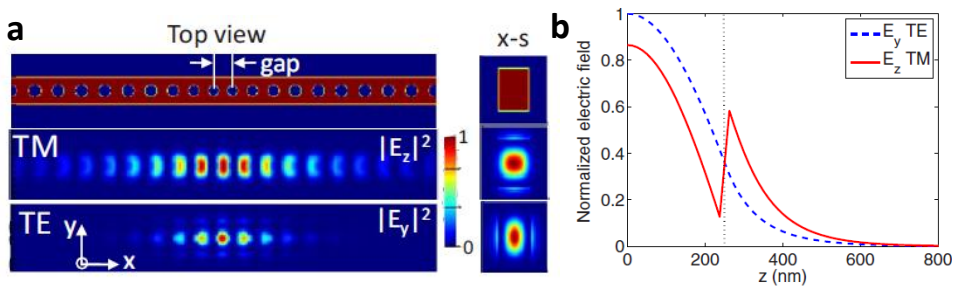

Figure 2.3.1: Simulation study of transverse electric/transverse magnetic cavities. (a)Field intensity profiles $|E_z|^2(|E_y|^2)$ for the TM (TE) modes shown from the top and in cross-section (x-s). The TM mode has a larger mode volume, and its field extends significantly above the cavity. (b) Comparison between the dominant electric field components of the two modes (normalized to the same energy) as a function of distance perpendicular to the device plane (z=0 denotes the middle of the cavity, and the dashed line marks the top surface).

exceeding 10^6 but this requires a very thick structure with thickness:width:period ratio of 3:1:1 [34]. Given the available silicon device layer thickness of 500 nm and the operating wavelength near 1500 nm, the cavities were designed with TE and TM modes with bare (intrinsic) Q of 7×10^6 and 1.2×10^5, and mode volumes of 0.56 and 1.37, respectively. The nanocavities have a designed width of $380 - 400\,nm$, hole pitch $a = 330\,nm$, radius $r/a = 0.265$, and a symmetric six-period taper to a pitch of $0.84a$ in the center of the cavity. The TE and TM modes are separated by 50 nm with the TE mode at higher energy. The field intensity profiles for the modes extracted from three-dimensional (3D) finite-difference time-domain (FDTD) simulations are shown in Fig. 2.3.1a.

Because TM modes have the dominant electric field component

oriented orthogonal to the device plane, they must be excited via evanescent or end-fire waveguide coupling techniques. They cannot be readily probed from free-space, since, like an electric dipole, they do not radiate parallel to the axis of the dipole moment. By contrast, in our geometry, the TE-cavity is only weakly coupled to a tapered optical fiber. This is due to the rather thick nanobeam, which causes the overlap with the fiber mode to be significantly reduced from what is typically the case for thin nanobeams. To understand this polarization-dependent coupling, consider the electric field strength of both TE and TM modes as a function of z from the middle of the cavity, as plotted in Fig. 2.3.1b. In the evanescent region (to the right of the dashed line), the TM E-field is about twice the magnitude of the TE E-field, which is a consequence of the field boundary conditions. Since the electric field of the TM mode is dominantly perpendicular to the silicon/fiber interface, it must satisfy the boundary condition $\epsilon_1 E_{z,1} = \epsilon_2 E_{z,2}$, where 1 denotes the silicon and 2 the fiber. On the other hand, the TE mode fields are oriented parallel to the interface, and must therefore be continuous across the boundary, i.e., $E_{y,1} = E_{y,2}$. By this simple argument, we expect an enhanced fiber coupling to the TM modes.

In light of these observations, we use two complimentary techniques in order to probe our TE-TM cavities. First, we employ a tapered fiber optical set-up. We pull an SMF-28 telecom fiber heated with a

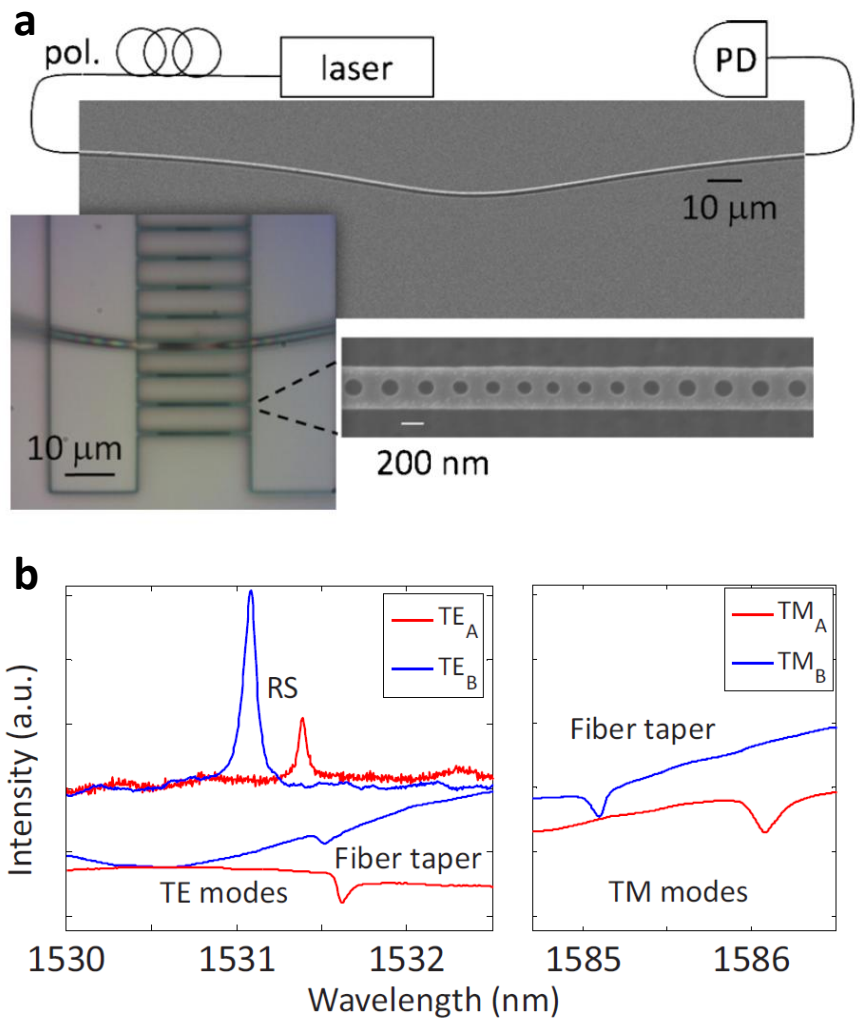

Figure 2.3.2: Characterization of transverse electric/transverse magnetic cavities using resonant scattering and tapered fiber technique. (a) SEM image of a dimpled fiber taper and a schematic of the optical set-up (PD photodiode). The optical image (left) shows the dimpled fiber taper in direct contact with a nanobeam cavity, which is shown in greater detail in the SEM inset. (b) Spectra from two cavities, A and B, each of which supports high Q modes at both TE and TM polarizations ($Q_{TE,A} = 28000, Q_{TE,B} = 18000, Q_{TM,A} = 10000$, and $Q_{TM,B} = 19000$). The fiber taper spectra reveal both features, whereas the RS spectra resolve only the TE modes, since they couple to radiation normal to the device plane. The color of each spectrum indicates the cavity being probed (red A, blue B). In the left panel, the fiber spectra are red shifted due to the presence of the fiber.

hydrogen torch to a diameter close to $1\,\mu m$. The fiber is mounted in a U-shaped configuration, which self-tensions the taper region and allows the fiber to be brought into close proximity with the sample surface. We then dimple the fiber by using a bare fiber as a mold, and applying pressure to the narrowest part of the taper while heating the contact region. The dimple, which is typically about $10\,\mu m$ in depth, as shown in Fig. 2.3.2a, creates a local evanescent probe to the nanocavity of interest. The tapered fiber is spliced into an optical set-up, and its location with respect to the sample is precisely positioned using motorized stages with $50\,nm$ encoder resolution (Surugu Seiki). The photodiode signal (Thorlabs Det010FC with a $1\,k\Omega$ load resistor) is passed through a low noise Stanford pre-amplifier and low-pass filtered at $1\,kHz$ before computer acquisition.

The second spectroscopy technique we use is a cross polarized resonant scattering (RS) set-up described earlier, in which light incident from normal to the plane of the sample is strongly focused by a 100X objective and the reflected signal detected in the cross polarization. This method allows us to confirm the polarization of the modes detected by the tapered fiber, since it is only sensitive to the TE modes. The cavities were fabricated with standard e-beam lithography and reactive ion etching methods, as described previously. Figure 2.3.2b shows spectra from two different high-Q, TE-TM nanocavities. The cavities are nominally identical except that the

filling fraction of the air holes of cavity A (red) is slightly smaller than that of cavity B (blue). These cavities are not actually fabricated according to the optimal design, but are intentionally detuned in order to lower the Q of the TE mode and increase its visibility in the spectra. This is achieved by reducing the gap between the two central holes by 20 nm (see Fig. 2.3.1a). However, the Q's still exceed 10^4 for each of the modes in the figure. We used a similar detuning method in previous work to predictably shift the Q and operating wavelength of our nanobeam cavities. Using SEM images of the fabricated structure, we perform 3D FDTD simulations of cavity A, and predict unloaded Q's of $Q_{TE,A} = 27000$ and $Q_{TM,A} = 60000$.

Measurements from both the fiber taper and RS set-ups are shown in the same graph. The TE mode of cavity A at $1531.4\,nm$ has a bare Q of 28000, as determined by RS, in good agreement with the simulated value (cf. cavity B, $Q^{exp}_{TE,B} = 18000$). The TM modes near $1585\,nm$ have loaded Q of ~ 10000, less than the predicted intrinsic Q value, which reflects in part the extent to which the fiber loads the cavity. As expected, the TE modes of the cavities can be probed using both experimental methods, whereas the TM modes couple only to the fiber taper. The fiber transmission spectra are acquired by touching the fiber to the cavity (as visible in the optical image in Fig. 2.3.2a), which was found to provide greater stability and repeatability compared to evanescent coupling from the air. In the

fiber data, the modes are revealed as dips since light which is dropped from the fiber into the cavity can couple into other losschannels of the cavity (e.g., scattering into free space). In the RS spectra, the modes appear as peaks on the nonresonant background although both dips and Fano features are possible . The Lorentzian lineshapes in the RS spectra are centered at the bare unloaded cavity resonance, and their widths give the unloaded Q of the cavities. The fiber spectra are slightly redshifted due to the perturbative effects of the silica fiber, and the amount of the shift depends on how exactly the fiber contacts the particular cavity.

Although the strength of the fiber coupling to both the TE and TM modes is similar in Fig. 2.3.2b, in general we observe a greatly enhanced coupling to the TM modes compared to the TE modes in our fabricated structures. Figure 2.3.3a shows a single spectrum (cropped to highlight the modes of interest) in which the coupling to the TE mode is only about 1 -T=0.05, whereas for the TM mode it is 1-T=0.3. We have not observed transmission drops greater than 1-T=0.1 (T =0.9) for the TE modes, whereas drops of 0.30.4 are quite typical for TM modes. This polarization-dependent coupling is not surprising in light of the field profiles shown in Fig. 2.3.1b.
Figure 2.3.3b shows TM spectra from a sequence of three cavities similar to the one in Fig. 2.3.3a, all of which exhibit large coupling of $1 - T = 0.30.4$ (T=0.6 0.7). Each of these cavities has a width of 360

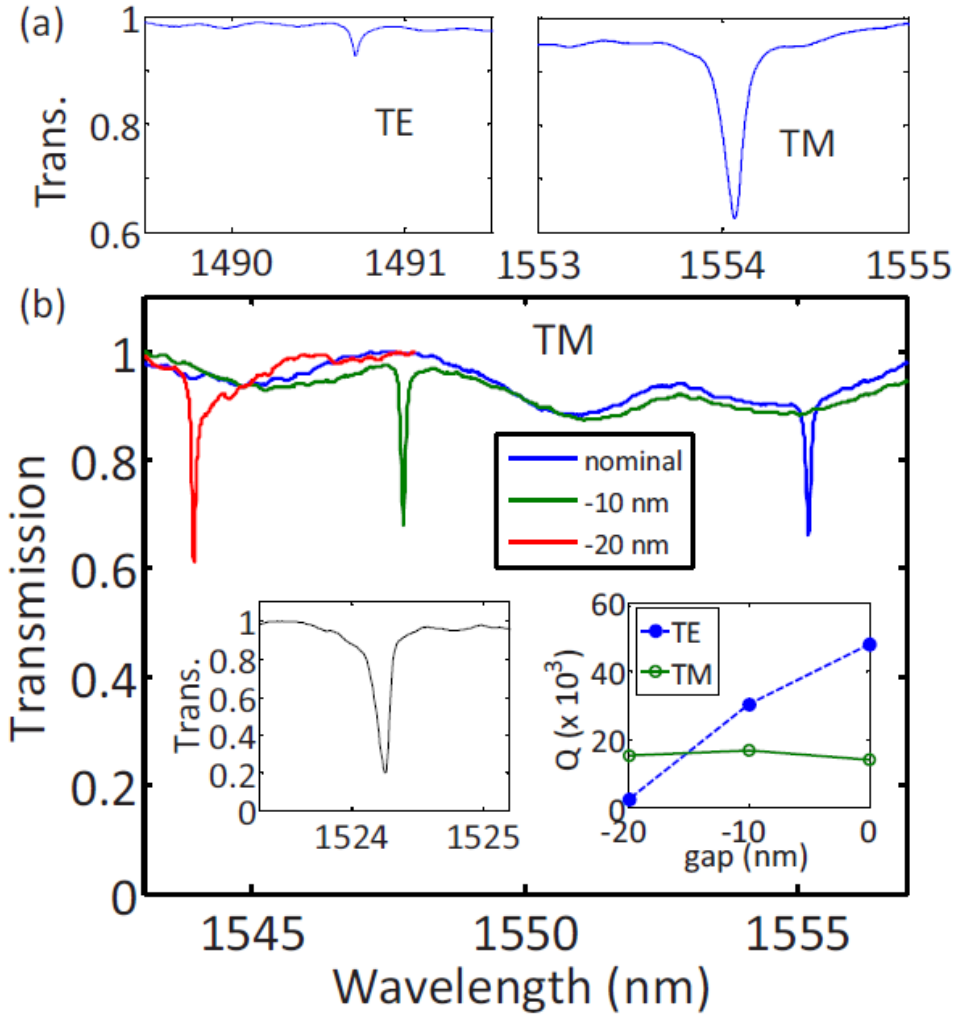

Figure 2.3.3: Experimental results of transverse electric/transverse magnetic cavities. (a) TE-TM spectrum highlighting the polarization dependent coupling. (b) TM spectra from three cavities which are well coupled to the fiber taper ($1 - T = 0.30.4$). The spacing (gap) between the central two holes of the cavity (see legend) varies the resonant wavelength but has little effect on the TM Q (see right inset), in contrast to the TE modes (Q_{TE} extracted from RS data). The left inset shows the very large coupling (1-T=0.8) of another similar TM cavity mode. The spectra are all acquired with the fiber in contact with the cavity.

nm, r /a=0.27, and a six-hole cavity taper, as described earlier. The three cavities differ only in the gap between the central two holes of the cavity. The resonance blueshifts as the gap is decreased, as expected. The Q ($\sim$ 15000) varies little for the TM modes over this range, whereas the TE modes are highly sensitive to the gap (see inset) due to their tight confinement in the cavity center. These trends agree well with FDTD modeling and our previous work; overall, the measured Q values are lower than in simulation due to fabrication imperfections. The dip can be as large as 1-T=0.8 (T=0.2), as shown in the left inset of Fig. 2.3.3a while maintaining a Q greater than 10^4, which is very promising for fiber-coupled applications. A more detailed analysis of the polarization-dependent coupling using coupled mode theory supports the simple argument based on Figure 2.3.1b, and shows that the TM mode in thick membrane cavities is much better phase-matched to the fundamental fiber mode than the TE mode. We foresee such TE-TM nanocavities playing an enabling role in integrated applications, such as nonlinear wavelength conversion and quantum-cascade lasers.

2.4 Waveguide Integration

In order to improve the signal to noise ratio and realization of integrated on-chip networks, we explored the butt coupling technique.

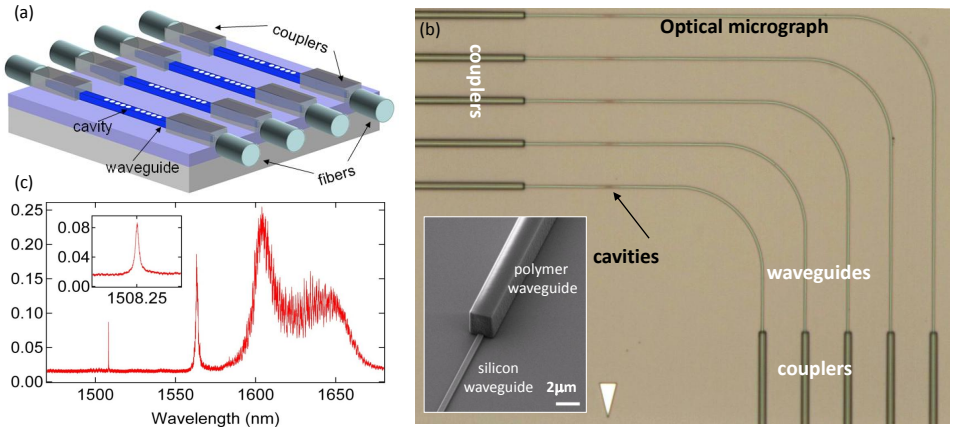

Figure 2.4.1: Waveguide integration of nanobeam cavities. (a) Schematic showing butt coupling technique using spot-size converter couplers based on polymer waveguides and inverse-tapered silicon waveguides. (b) Optical micrograph showing the fabricated device with the in and out coupling pads, silicon waveguide and PCNC. Inset shows a SEM image of the polymer coupling pads (c) Transmission from a devices similar to the one shown in (b).

This technique takes advantage of spot-size converters to couple light from a tapered optical fiber into the on-chip optical waveguide (refer Fig. 2.4.1a). In this case, the converter is in the form of polymer (SU-8 photoresist) waveguides (ref Appendix B) whose cross section and resulting mode profile is comparable to the spot emerging from the tapered lensed optical fiber. Light is then adiabatically coupled from the polymer waveguide into the silicon waveguide using the inverse taper geometry, and then from the silicon waveguide into the nanobeam cavity using the adiabatically tapered photonic crystal. Efficient coupling of light from waveguide into the cavity is achieved by using a hole taper similar to the one described earlier. Light transmitted through the system is collected by a second spot-size

converter and tapered fiber. Fig. 2.4.1b shows an optical micrograph of such a fabricated structure with the input coupling pads, silicon waveguides, cavities and output coupling pads. The inset shows the zoomed-in SEM image of the polymer coupling pad. Coupling efficiencies as high as 80 % over more than 150 nm could be achieved using this technique. The transmission spectrum shown in Fig. 2.4.1c features the excellent quality of signal to noise achieved using the above technique. The inset shows the zoomed region around the cavity resonance. It should be noted that the cavities were modified for waveguide integration to improve the transmission by including the tapering after the Bragg mirrors.

This method is ideal for testing cavities designed using the deterministic approach given that high transmission is one of the merits of the design. A typical transmission spectrum through such a cavity is shown in Fig. 2.4.2a. A nonlinear bistable lineshape is also observed, as shown by the power dependent spectra in Fig. 2.4.2b. We fitted the experimental data using the following expression, typical of a nonlinear bistability:

$$T = \frac{P_{out}}{P_{in}} = \frac{Q_{total}^2/Q_{wg}^2}{1 + [P_{out}/P_0 - 2(\lambda - \lambda_0)/\gamma_0]^2} \tag{2.1}$$

where $P_0 = 3gQ_{total}Q_{wg}[\omega/(2nc)]^2\chi^{(3)}$ is the measured power in the presence of a third-order nonlinearity, g is a nonlinear feedback

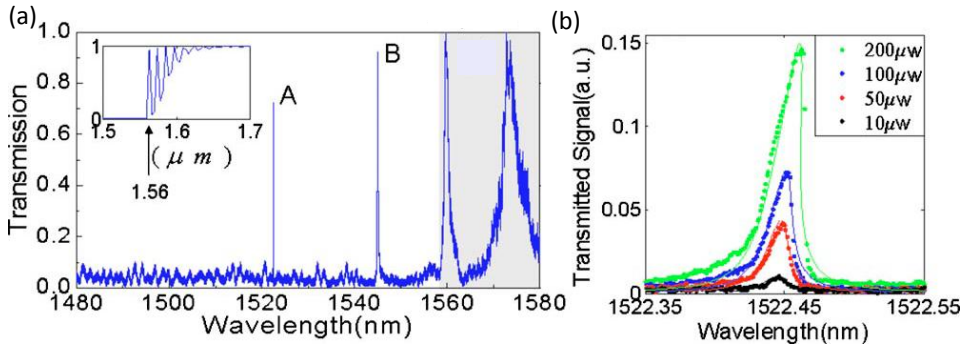

Figure 2.4.2: Experimental results for cavities designed using deterministic approach. (a) Transmission spectrum of the cavity with input power $100\ \mu W$. The signal is normalized by the band edge modes (shaded region), which have unity transmission, as verified by 3D-FDTD simulations shown in the inset. Due to the very large photon life time of our ultrahigh Q cavity ($\tau_{photon} = Q/\omega \sim 1\ ns$) it becomes nearly impossible to model transmission through the cavity (resonant tunneling) using the 3D-FDTD method directly. Hence, the high-Q cavity mode does not appear in the simulated spectrum shown in the inset. (b) Zoom-in of the transmitted signal of the fundamental mode at different input power levels (measured at the fiber tip). The dots are experimental data and the lines are the fitted curves using Eqn.

parameter introduced by [37] and γ_0 is the natural cavity linewidth. $g \sim 1/V_{eff}$ is a measure of the field confinement in the nonlinear region. From the fits, we obtained an experimental $Q = 80000$ (Q_{total}) and an on-resonance transmission $T = 73\,\%$ for the on-substrate and polymer capped cavity. This corresponds to a $Q_{sc} = 500000$ (Q_{sc}: scattering Q) ($T = Q_{total}^2/Q_{sc}^2$), which is comparable to our previously reported results for a freestanding PCNC.

2.5 Coupled Cavities

There is also much recent excitement about the possibility of entangling optical and mechanical degrees of freedom in waveguides [8, 11, 12, 38] and coupled-cavity devices [6, 10, 39]. To achieve optomechanical coupling, the cavities require a small mass and a flexible platform. These two properties are inherent to PCNCs. In addition, coupled nanobeam cavity structures could facilitate adiabatic wavelength conversion in a similar manner to that predicted for a double-layer photonic crystal slab cavity, for which it was shown that broad bandwidth dynamic resonance tuning could be realized while maintaining the high Q of the cavity mode [40]. So we studied the static tuning of double cavity modes in nanobeam cavities by varying the cavity separation, thereby demonstrating a proof-of-principle of this effect. In this work, we studied coupled PCNC consisting of two parallel suspended beams separated by a

small gap, each patterned with a one-dimensional line of holes, as shown in Fig. 2.5.1a and b. We experimentally explored the resonances in coupled nanobeam silicon structures as the coupling strength was varied via the nanobeam separation. We investigated both on substrate and freestanding devices using the freespace optical probe technique (resonant scattering), which does not perturb the cavities. Fig. 2.5.1c shows ten such beams allowing for possible CROW (coupled resonator optical waveguides) applications.

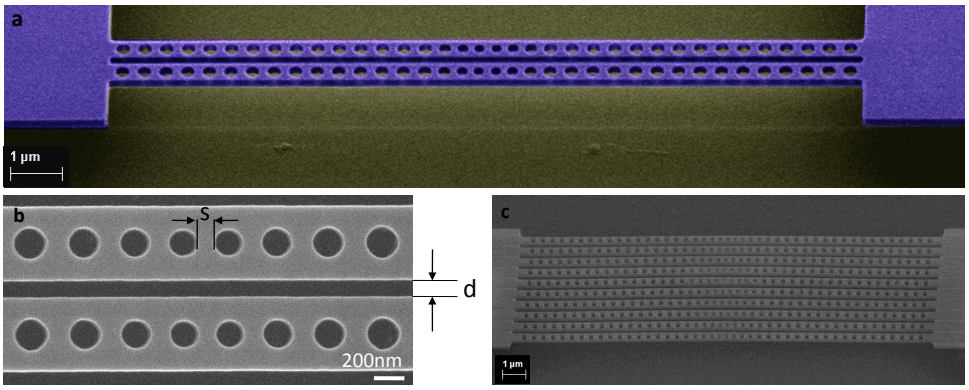

Figure 2.5.1: SEM images of coupled nanobeam cavities. (a) and (b) Double nanobeam cavity, showing the separation $d = 100\,nm$ and cavity length $s = 146\,nm$. (c) SEM image showing 10 coupled nanobeam cavities.

We created double cavity structures by positioning two PCNCs side-by-side and varying the air gap between them. As expected from the physics of coupled harmonic oscillators, coupling generates modes which are symmetric and antisymmetric superpositions of the single cavity basis states, as shown in Fig. 2.5.2. The frequency splitting between the modes is dependent on the strength of the coupling,

which in this case is determined by the size of the gap. The mode profiles, $Q's$, and resonant wavelengths are shown in Fig. 2.5.2a and b as a function of the gap, d, between the nanobeams. The data was simulated with a three dimensional, finite-difference, time-domain code. For small d, there is a strong coupling between the cavities. This leads to a large wavelength splitting between the modes, with the even mode at longer wavelength, which is typical of coupled resonators. The wavelength of the odd mode changes little with d, whereas the even mode disperses rapidly to longer wavelengths as d decreases. This asymmetry indicates the presence of second-order cross- and self-coupling effects between the coupled resonators in addition to the first-order effects of the index perturbation [41]. As d shrinks below $100\,nm$, the field intensity of the gap antinode grows and becomes the dominant feature in the mode. At the same time, the Q declines, since the PhC tapering is not optimized for the significant redistribution of the mode energy into the slot between the nanobeams. These factors imply that the even mode would be a sensitive probe of the interbeam distance, and thus useful for optomechanical applications. It would also be useful in biosensing and chemical-sensing, as the gap antinode would be highly sensitive to perturbations in the external environment.

In contrast to the significant alterations of the even mode, the odd mode is similar in profile to a superposition of two uncoupled single

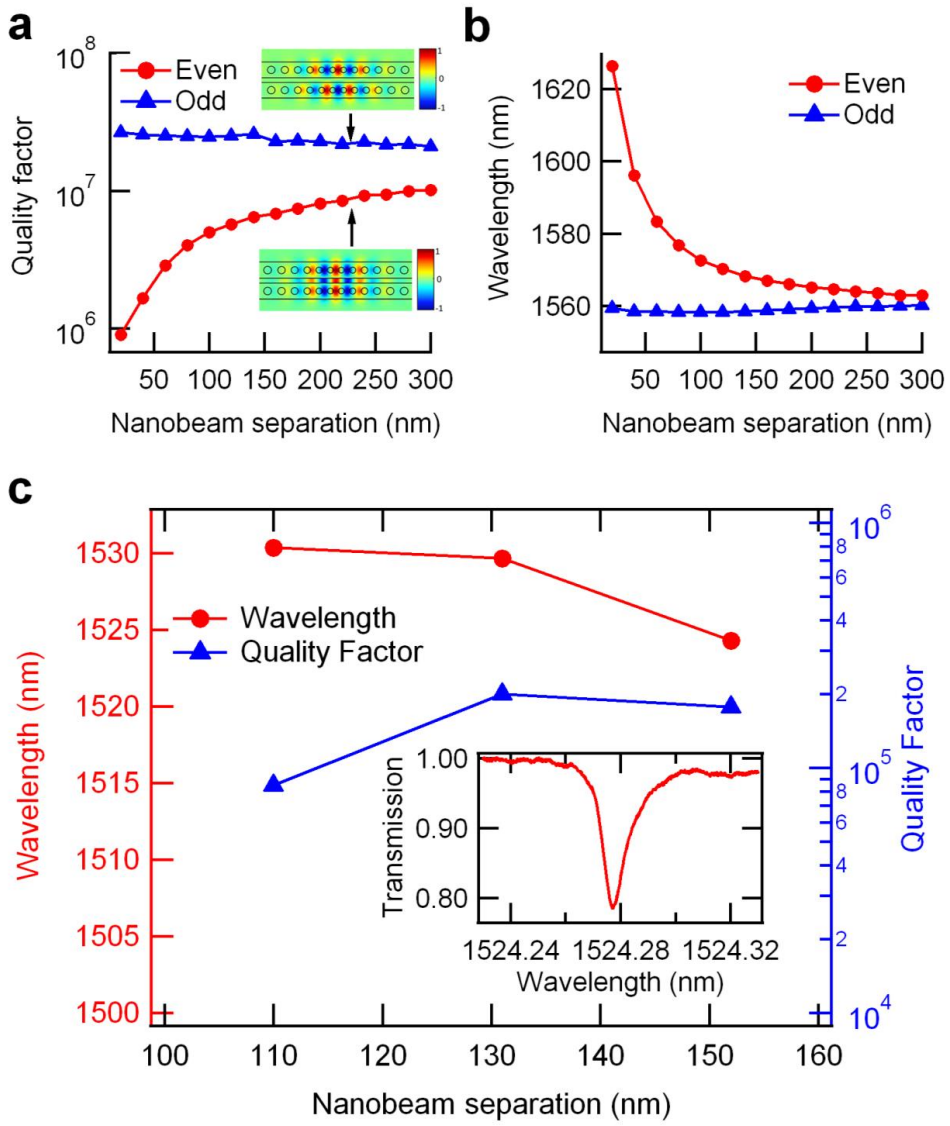

Figure 2.5.2: Simulated and experimental results of suspended coupled nanobeam cavities for various spacings. (a) Q's of even and odd coupled nanobeam modes. Insets show Ey components of the modes. (b) Mode wavelengths as a function of separation, showing large dispersion of the even mode.(c) Mode wavelength and Q for different nanobeam separations. The resonant scattering spectrum for the 150 nm double cavity is shown in the inset

cavity modes. The relatively flat odd mode dispersion is likely due to the opposing effects of the first- and second-order coupling terms. The Q, however, is substantially higher than that of the even mode and in fact is approximately twice the Q of a single nanobeam cavity 1.4×10^7. Intuitively, this is consistent with the larger mode volume, $V = 0.7(\lambda/n)^3$, which is about twice that of the single cavity; the more extended real-space distribution of the fields results in a more localized k-space distribution, and therefore a reduction in the radiative components within the light cone. Also, it is likely that this mode does not couple well outside due to destructive interference. We experimentally probed our double nanobeam cavities using a cross-polarized resonant scattering technique (see Appendix B). Because the resonant excitation field drives the (E_y) fields in the coupled nanobeams in phase, this technique is primarily sensitive to the even mode. We note that in principle, the field gradient of the focused spot could be exploited to excite the odd mode, as could butt coupling or evanescent waveguide coupling techniques [20, 42, 43]. Figure 2.5.2c shows the resonant wavelength and Q of the even mode for three different nanobeam separations. The mode redshifts as d decreases, in agreement with our simulations Fig. 2.5.2b, although the data (refer Fig. 2.5.2c) may reflect additional small contributions from e-beam proximity effects and fabrication imperfections (dimensions change by a few nanometers but this change is not same along the

length of the nanobeam and hence difficult to quantify). The Q varies between 1×10^5 and 2×10^5. Although this is more than an order of magnitude lower than predicted by simulations, this is a highly useful range for applications and we expect increases as the fabrication quality of our structures improves.

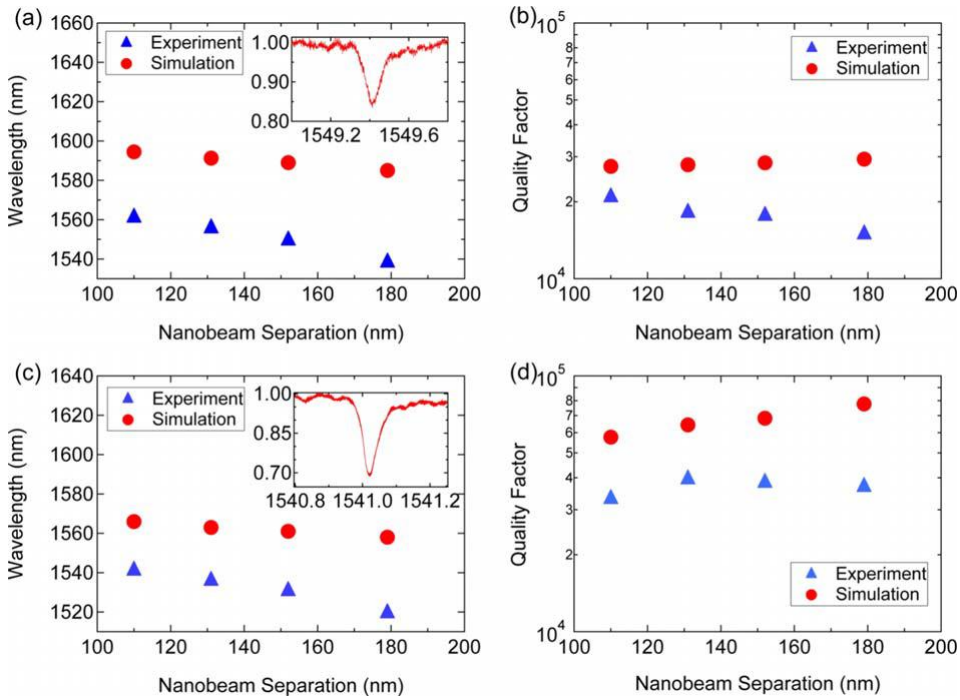

Figure 2.5.3: Comparison between on-substrate and suspended coupled nanobeam cavities. Wavelength and Q as a function of measured separation for on-substrate [(a) and (b)] and freestanding [(c) and (d)] double nanobeam cavities. The insets show typical spectra normalized by reference spectra taken away from the cavity. The simulations in [(a) and (b)] do not include the residual $\sim 40\,nm$ FOx resist layer (the FOx resist was not removed for these cavities, since any etch process would also remove the substrate.), which has a negligible effect on the Q and shifts the wavelength by only a few nanometers

We also investigated the effect of the substrate on the cavity modes.

As mentioned above, for small d, the even mode field intensity is concentrated in the space between the cavities. This slot mode could be useful for biosensing and chemical sensing, but to be robust in a liquid environment such a device would require the structural stability provided by a substrate. Due to the limited tuning range of our laser, these data were obtained from cavities with a spacing (s) of 136 nm, which is smaller than our optimal, high Q design of 146 nm data shown in Fig. 2.5.2c. In Fig. 2.5.3a and b, we present the results of our resonant scattering spectroscopy for unreleased, on-substrate nanobeam cavities (i.e., supported by SiO_2). The FOx resist was not removed for these cavities, since any etch process would also remove the substrate. However, we estimate that the resist layer remaining on top of the silicon nanobeams has a thickness less than 40 nm. The resonant wavelength and Q of the even mode are plotted as a function of d. The resonance blue shifts with increasing d as the effective index of the cavity mode decreases. The experiment shows a larger dispersion than the simulation, likely reflecting the increasing role of e-beam lithography proximity effects for small gaps. The measured $Q's$ of $1.5 - 2.0 \times 10^4$ are remarkably high for supported cavities, considering that the designs were optimized for freestanding nanobeams. Given the robust structure, high $Q's$, and field intensity in the gap, the supported double nanobeam cavity is a promising approach to scalable, on-chip sensing applications. Figures c and d

show the experimental data for the same cavities after the sacrificial SiO_2 substrate was removed. The modes are blue shifted compared to the results of Fig. 2.5.3a, as expected from the decreased effective index of the air cladding compared to the oxide. The $Q's$, however, are increased by a factor of ~ 2 due to the reduced leakage into the substrate. We note, however, that our cavities were optimized for free-standing operation, and therefore the modest $Q's$ are not surprising.

2.6 Applications

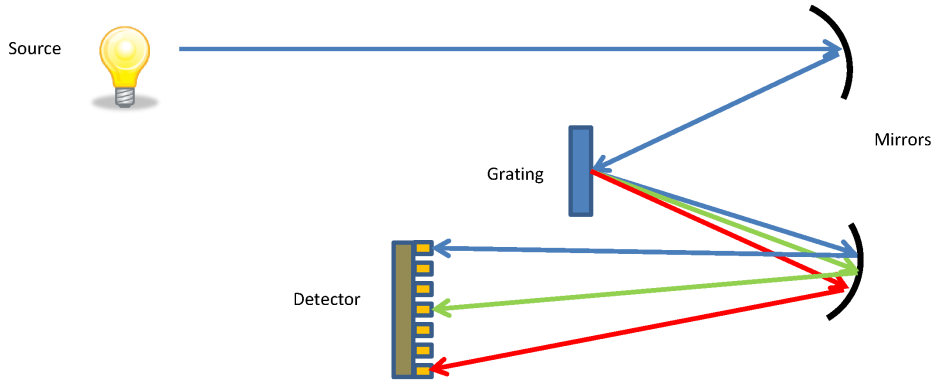

Figure 2.6.1: Schematic of a grating spectrometer.

Ultra high Q and small mode volume make PCNCs ideal for applications in optoelectronics, sensing and QED. One application of PCNC that we demonstrate is a compact, fully integrated, on-chip spectrometer [44] operating in the telecom region. Figure 2.6.1 shows

the schematic of the working principle of a spectrometer based on dispersive component. Light is bounced off a grating and the dispersed light is detected using a linear array of detectors. The resolution of such a spectrometer scales with size as higher resolutions require a longer optical path. The realization of a microspectrometer relies on the successful replacement of the dispersive element with a micro component. Significant progress has been made in integrated microspectrometers based on arrayed-waveguide gratings [45], superprism-based spectrometers [46], grating spectrometers [47, 48], and diffractive grating spectrometer combined with thermo-optically tuned microring resonators [49]. Here, we show a robust, on-chip spectrometer based on an array of PCNCs tuned to operate at slightly different wavelengths. Since each device will resonate at one particular wavelength, the spectrum of the incoming light can be reconstructed by detecting signal from the individual devices. However, this arrangement will give discrete spectrum and also suffer from fabrication tolerances. To overcome these issues, we propose on using microheaters which will thermally tune the resonance of the individual cavities to achieve a continuous spectrum. Also, due to scalability of photonic crystals, such a spectrometer can be designed to operate in any range of electromagnetic spectrum with a compatible material system.

We realized spectrometer that consists of 32 PCNCs, with

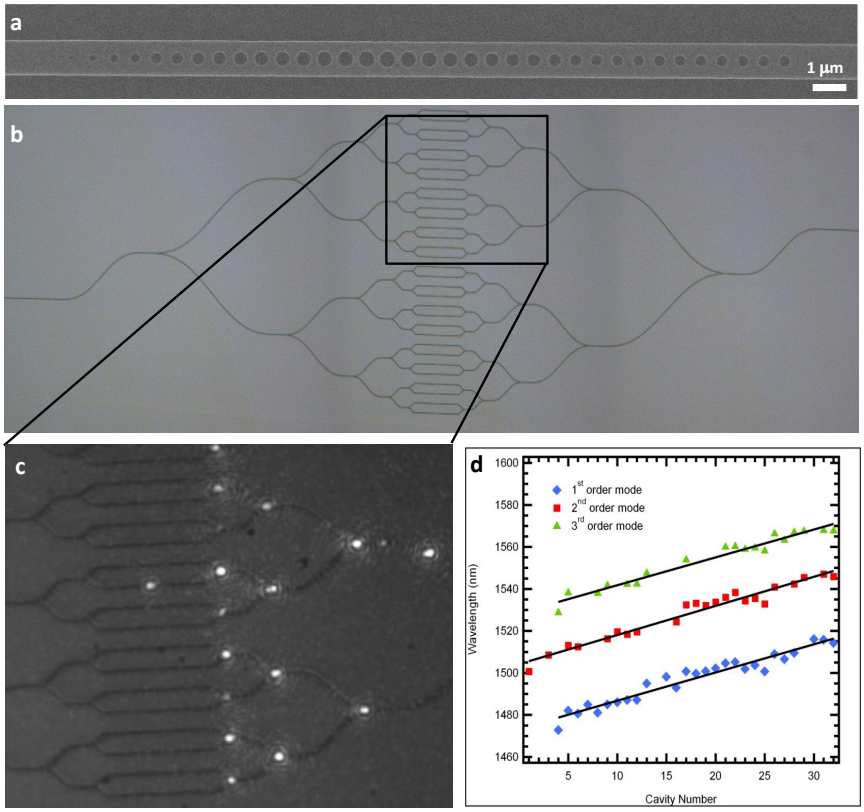

Figure 2.6.2: On-chip spectrometer using nanobeam cavities. (a) SEM image of 1 of the 32 PCNCs used in the spectrometer. (b) Optical micrograph showing the 32 devices. (c) Top view taken using an IR camera with only once cavity resonating at the input light wavelength. (d) Experimental data for the 32 devices showing the first three modes.

resonances 1 nm apart using the deterministic approach. The measured linewidth of each cavity was 120 pm which is at par with the resolutions obtained using a grating spectrometer. The cavities were designed to scatter light in the vertical plane. This was achieved by extending the Bragg mirror on one side as seen in the SEM image in Fig.2.6.2a. This allowed us to view the scattered light using a

sensitive IR camera. The cavities were fabricated on a SOI platform with a device layer of 220 nm and a buried oxide of 2 μm. The devices were fabricated using the process outlined in Appendix A. A PMMA layer was spun to cover the devices as they were designed to have symmetric cladding. An optical micrograph of the fabricated structure is shown in Fig. 2.6.2b. The incoming light is split using multiple Y splitters and coupled into individual cavities. The device was characterized using a tunable IR laser source and a sensitive InGaAs detector. Figure2.6.2c shows an IR image of the cavity section with monochromatic input light from a laser. As expected, scattering of light is observed only from one cavity. Figure 2.6.2d plots the first three modes for each of the cavities. The solid line shown the expected wavelengths for each of the modes. Results show an excellent agreement with theoretical values. The slight divergence from the solid line was attributed to the fabrication tolerances.

However, in order to be useful for spectral analysis, the fabrication tolerances need to be corrected by some post fabrication trimming. This was achieved by using thermo optic tuning (thermo optic coefficient of silicon (dn_{Si}/dT): $1.86 \times 10^{-4}\ K^{-1}$) of the cavity resonance by using electrical micro-heaters above each device [50]. This not only corrects for the fabrication error but also reduces the amount of devices necessary to cover a given spectral region. Figure 2.6.3a shows an optical image of the micro-heater fabricated

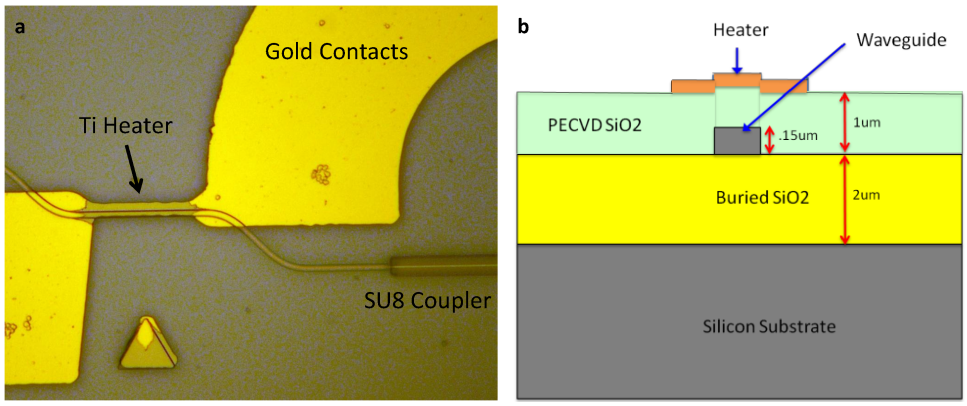

Figure 2.6.3: Thermal reconfiguration of nanobeam cavities using micro-heaters. (a) Optical micrograph showing the device with microheaters. (b) The cross section schematic of the device.

over the PCNC and Fig. 2.6.3b shows the cross section of the Ti heater section. An additional PECVD step was carried out after fabricating the SU-8 coupling pads (refer to Appendix A), to deposit 1 μm of oxide followed by a photolithography step to define the heaters and electrodes. The oxide layer was needed to avoid any unwanted loss of light due to its interaction with the heaters. Titanium (100 nm) and gold (200 nm) were evaporated, followed by a lift-off in Acetone. Another photolithography step was carried out to remove gold above the heater region. This was necessary to achieve a highly resistive heating element which resulted in maximum voltage drop, and hence heating above the device. Finally, the sample was cleaved through the $SU8$ pads and the facets were polished to achieve optically flat surfaces. Thermal tuning of more than 7 nm was achieved for one device. The resistance of the heater was measured to

be around 150 Ω. Fig. 2.6.4 shows the detuning of the mode for various applied voltages. Since electrical power is converted to heat, the detuning is linear with the square of the voltage value.

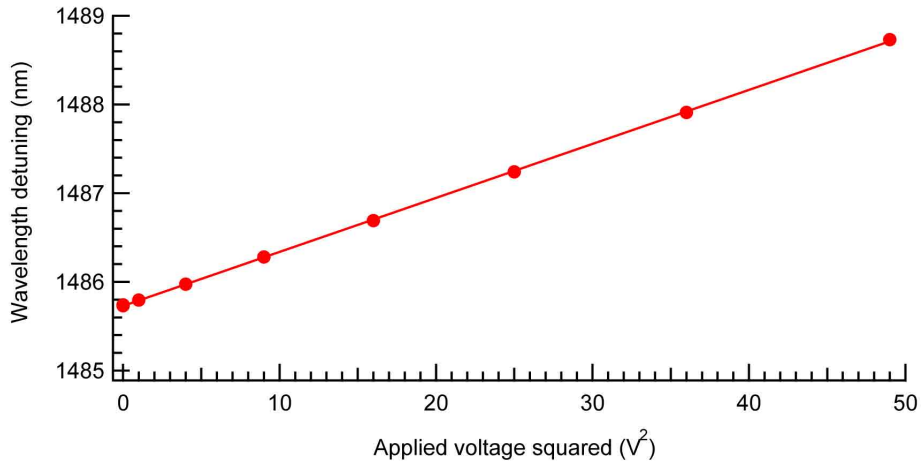

Figure 2.6.4: Experimental results showing thermal detuning of the cavity mode. The x-axes is plotted as square of the applied voltage to show the linear relationship of mode detuning with heat

As a proof of concept, we tried to measure a spectral line of acetylene by noting the transmission while thermally tuning the cavity resonance. The thermal response curve for the cavity under test was first determined by applying different voltages to the heater and noting the detuning of the cavity by scanning a tunable laser. Light from a broadband super luminescence diode (SLD) source was then allowed to pass through an acetylene absorption chamber and the transmitted light was then coupled to a PCNC with a microheater)(refer Fig. 2.6.5a). An optical filter was used to filter out

the light transmitted outside the bandgap. The transmitted light was then noted while the cavity resonance was scanned by applying voltage to the microheater. Figure 2.6.5b shows one absorption spectral line measured using a conventional bench-top grating spectrometer with a 0.1 nm resolution (red curve). The blue curve was obtained by thermally tuning the resonance of a PCNC (linewidth = 0.12 nm) across the spectral line. We see that good agreement with the data obtained from a conventional spectrometer validates the working of our ultra compact PCNC based spectrometer.

2.7 Conclusion

In conclusion, we have designed and fabricated ultrahigh-Q PCNC using a five-hole taper design with a measured Q of 7.5×10^5. We reported the use of the resonant scattering method for measuring PCNC cavities. We have also experimentally demonstrated high Q, dual-polarized TE-TM PCNCs in silicon. The modes are separated by 50 nm, and have Q's greater than 10^4. Such high Q cavities may find their use in applications like biosensing, nonlinear wavelength conversion and quantum cascade lasers.

We also studied coupled nanobeam cavities in which by varying the spacing of two nanobeam, we experimentally demonstrated a resonant wavelength shift of 20 nm due to intercavity coupling in dual cavities

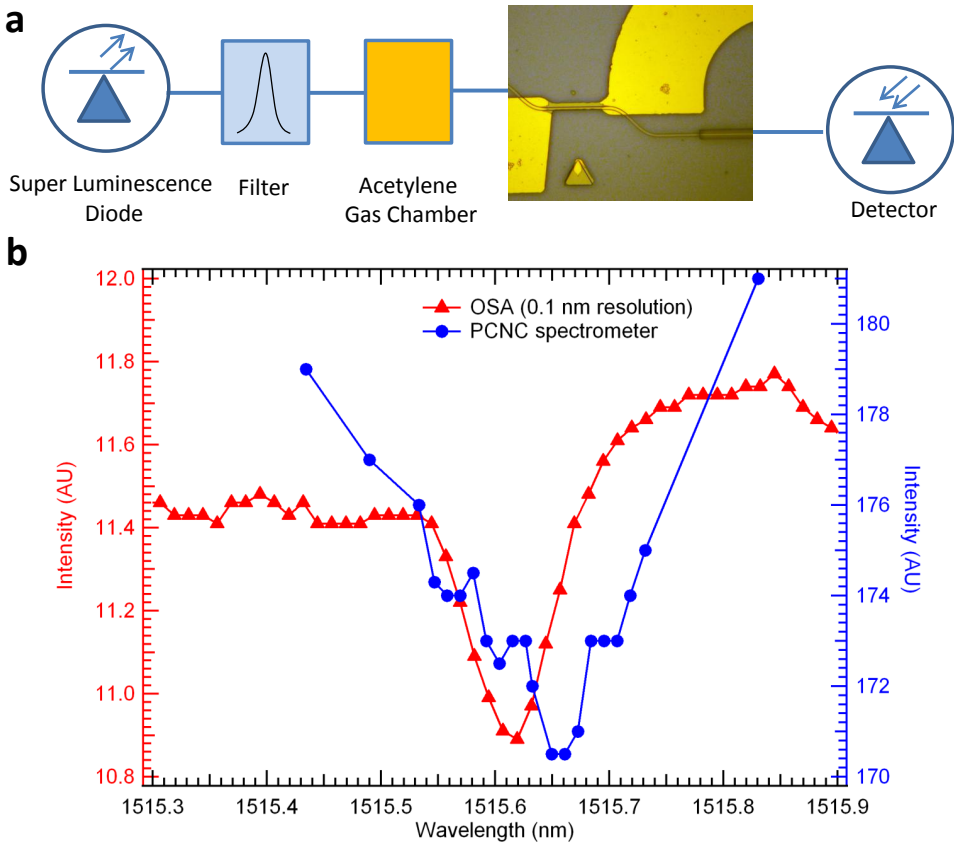

Figure 2.6.5: Measurement of absorption spectrum of Acetylene. (a) Schematic of the experimental setup.(b)Results showing the absorption spectrum line of acetylene obtained using a conventional bench top optical spectrum analyzer and the on-chip spectrometer.

while maintaining a relatively constant Q. This effect would be magnified for coupled nanobeams with smaller separations. The devices on silicon dioxide have also been studied and show decent $Q's$, on the order of 10^5. The ability to tune the resonant wavelength of a cavity without adverse effects on the Q opens up potential areas for research in optomechanics, adiabatic frequency conversion, and sensing. We also studied waveguide integrated devices and demonstrated a compact, on-chip spectrometer and showed reconfiguration capability using thermo-optics effects by implementing micro-heaters over the devices.

Electrostatics taught me to control my desires,

as there's always a fear to be pinched-off

3

Electrostatic Force Reconfiguration

MANY OF THE APPLICATIONS mentioned and discussed earlier involving photonic crystal cavities, are limited by fabrication tolerances and the inability to precisely control the resonant wavelength of fabricated structures. Various techniques for post-fabrication wavelength trimming [51, 52] and dynamical

wavelength control - using, for example, thermal effects [2–4] , free carrier injection [5], low temperature gas condensation [53], and immersion in fluids [54] - have been explored. However, these methods are often limited by small tuning ranges, high power consumption, and the inability to tune continuously or reversibly. PCNCs can be viewed as a doubly clamped nanobeam, the simplest NEMS device, perforated with a one-dimensional lattice of holes. By combining nano-electro-mechanical systems (NEMS) and nanophotonics, we demonstrate reconfigurable photonic crystal nanobeam cavities that can be continuously and dynamically tuned using electrostatic forces.

When two PCNCs are placed in each other's near field, as shown in Fig. 2.5.1, their resonant modes couple, resulting in two supermodes with resonant frequencies that are highly dependent on the spacing between the nanobeams. This can be attributed to two major factors. Firstly, the coupling between the two resonators increases with the reduction in the lateral separation between the nanobeams, which results in a greater splitting between the two supermodes. Secondly, as the nanobeams are drawn closer together, the higher order effect of the coupling-induced frequency shift [41] becomes significant (especially for separations $< 100\,nm$) causing red shifting in both of the supermodes. The net effect of these two factors is that the even supermode experiences a considerable red shift as the separation is reduced, while the wavelength of the odd supermode stays relatively

constant (the two effects cancel out). The strong dependence of the wavelength of the even supermode on the separation between the two nanobeams renders coupled-PCNCs highly suited for applications in motion and mass sensing. In addition, the strong optical fields that exist in the air region between the coupled-PCNCs make these devices excellent candidates for biochemical sensing applications. Finally, by simultaneously taking advantage of both the optical and mechanical degrees of freedom of such these cavities, a plethora of exciting optomechanical phenomena can be realized.

3.1 Simulations

We take advantage of the mechanical flexibility of coupled PCNC to realize reconfigurable optomechanical devices that can be electrostatically actuated [55]. By applying a potential difference directly across the nanobeams, an attractive electrostatic force can be induced between the two nanobeams, resulting in a decrease of the gap between the nanobeams, as can be seen in Fig. 3.1.1 a and b. This, in turn, results in the change of the resonant wavelength of the two supermodes. Self-consistent optical, electrical and mechanical finite-element simulations were used to model the deflection of the nanobeams due to the electrostatic forces, and their influence on the optical eigenfrequencies [Fig. 3.1.2a]. Figure 3.1.2b shows the

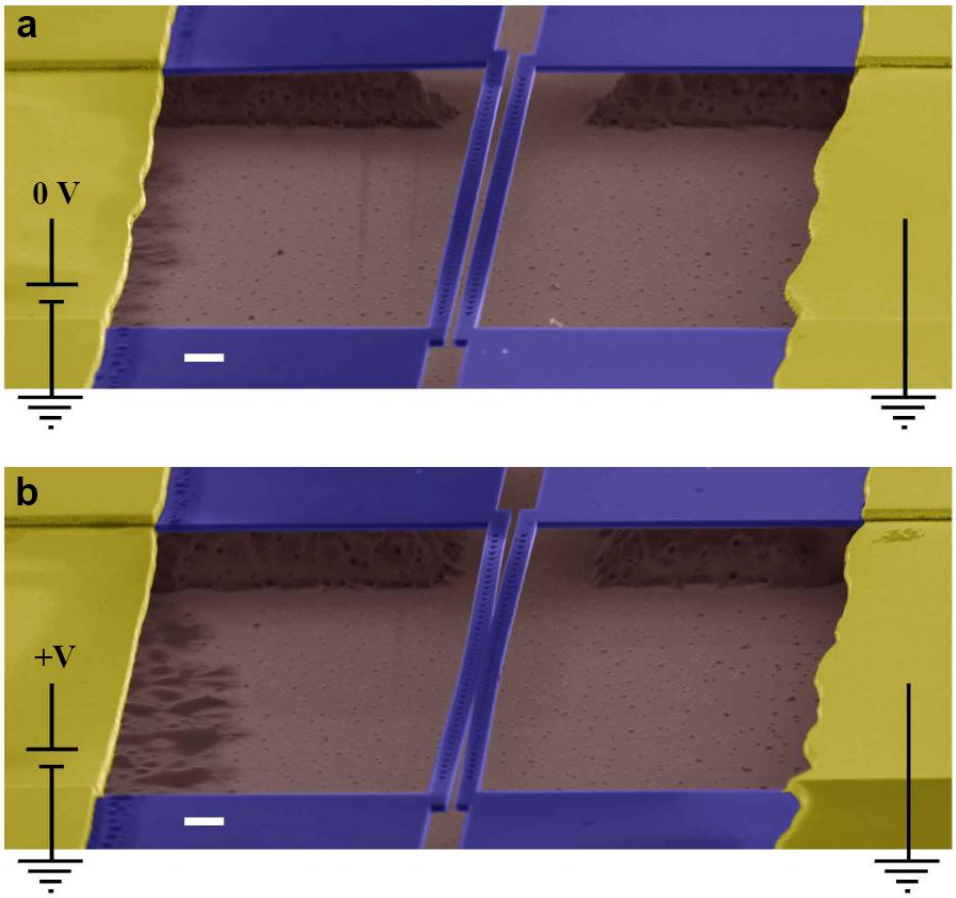

Figure 3.1.1: Coupled photonic crystal nanobeam cavities for electrostatic reconfiguration.(a) SEM image of a representative fabricated structure. The suspended silicon is in contact with gold electrodes seen at the edge of the image and is supported by islands of SiO_2 (scalebar $= 1\,\mu m$). (b) SEM image showing the deflection of the nanobeams due to electrostatic actuation.

dependence of the nanobeam separation (red curve) on the applied voltage, as well as the actuating force (blue curve) for different bias voltages, in the case of a device with 77 nm initial separation between nanobeams. It can be seen that nanobeam separation, measured at the middle of the nanobeams, can be reduced to 50 nm with $\sim 5\,V$ of external bias. The influence of the electrostatically-controlled nanobeam separation on the resonances of two supermodes is shown in Fig. 3.2.1(a). We found that, in our system, the even supermode red shifts while the odd supermode experiences very little dispersion (remains effectively stationary). This is in good agreement with our previous results (chapter 2), where the dependence of the supermode eigenfrequencies on lithographically-defined separations (static tuning) was studied.

3.2 Experimental Results and Discussion

Figure 3.2.1(b) shows the experimental results for the nanobeam cavities, illustrating the dependence of the even and odd supermode eigenfrequencies on the applied bias voltage. Very good agreement with numerical modeling can be observed. The experimentally measured resonant wavelengths were within 2 % of the simulated ones, and the tuning trend matched very well with the theoretical predictions. The slight discrepancy can be attributed to several

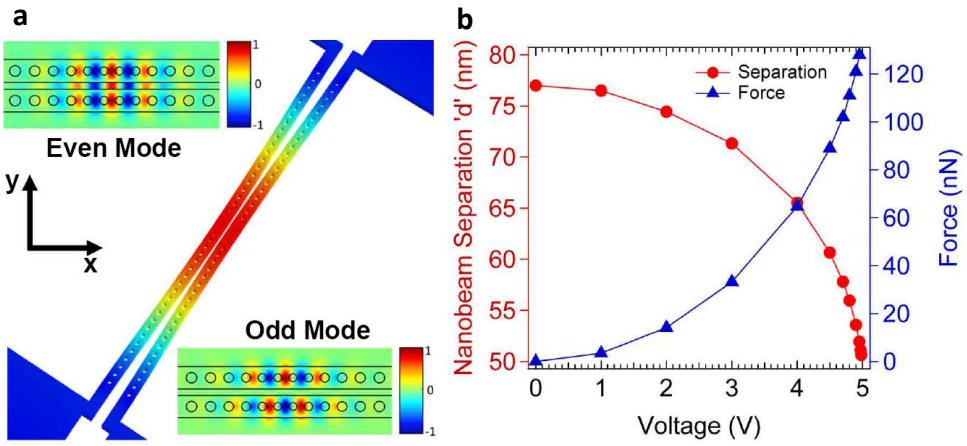

Figure 3.1.2: Simulation of generated electrostatic force and deflection of nanobeams. (a) Finite element simulations showing nanobeams deflected due to an applied potential. The insets depict the E_y component of the optical supermodes of the coupled cavities. (b) Simulation data: the red curve shows the lateral separation of a pair of nanobeams, measured at the center of the structure, as a potential is applied across them, while the blue curve shows the force generated due to the applied voltage.

effects, including the uncertainty in the refractive index of the doped silicon device layer, variations in the layer thickness, and uncertainty in the amount of tensile stress in the device layer of the SOI ($\pm 25\, MPa$, according to SOITEC). The optical Q-factor of the modes was determined by a Fano fit [56] to the scattered waveform. The Q factor of the even mode was around $13,000$ while that of the odd mode was around $50,000$. In this work, we intentionally designed and fabricated cavities with a lower Q, in order to facilitate experimental characterization via the resonant scattering approach. The signal-to-noise ratio for low Q cavities is higher since more light can be scattered into, and subsequently detected from, these cavities.

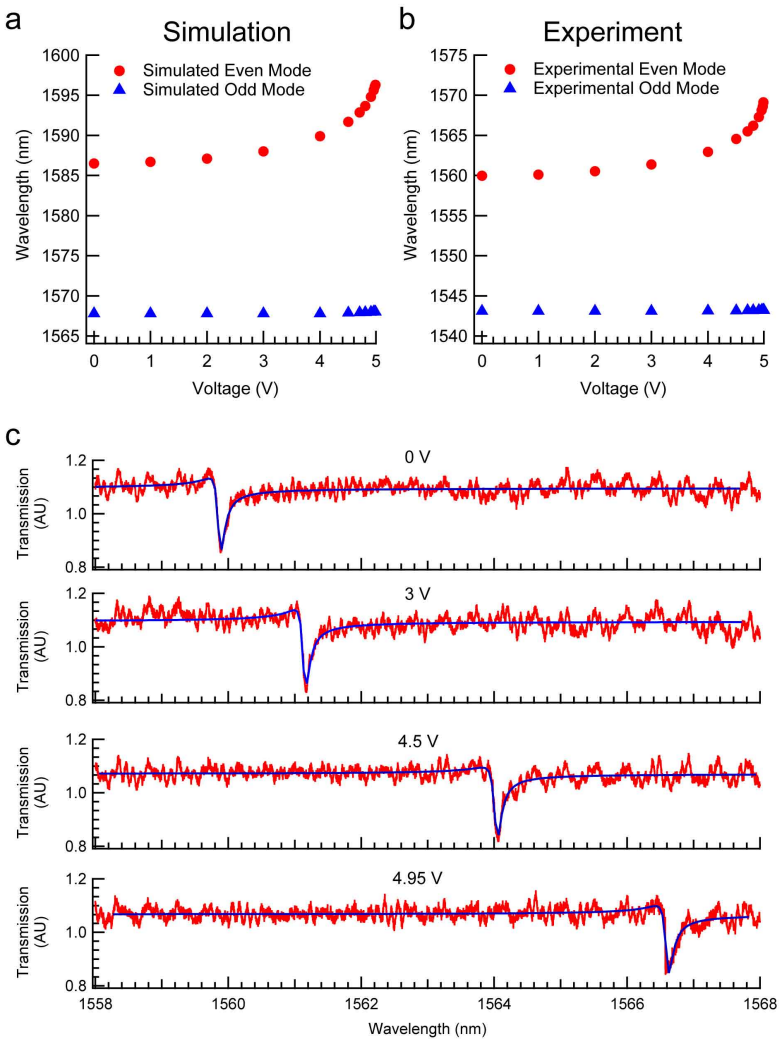

Figure 3.2.1: Experimental results for electrostatic tuning of coupled photonic crystal nanobeam cavity. (a) Finite element simulations showing the dependence of the even (shown in red) and odd (blue) supermode resonance on the applied bias voltage. (b) Experimental data showing the measured resonances for even and odd supermodes. The trend seen in the experimental data matches well with the simulated results. The slight discrepancy in the absolute value of resonant wavelength can be attributed to uncertainty in the thickness and refractive index of the device layer of the SOI wafer, as well as the amount of tensile stress in the nanobeams. (c) Detected spectrum and Fano fits at different applied voltages.

It is important to emphasize that the Q factors did not change observably across the whole tuning range. This is in stark contrast to tuning via free-carrier injection, which results in significant reduction in the cavity Q-factor due to free-carrier absorption. Figure 3.2.1(b) also shows that the odd mode does not tune with applied voltage, which is consistent with our earlier work (chapter 2). In our best devices, we were able to shift the resonant wavelength of the even supermode up to $9.6\,nm$ when less than $6\,V$ of external bias voltage was applied [Fig. 3.2.2(a)]. This wide tuning range is nearly 80 times larger than the linewidth of the cavity resonance in the present design, and this ratio can be further improved by increasing the Q-factor of the fabricated cavities. Figure 3.2.2(a) also shows the sensitivity plot for the measured cavity, defined as the change in the resonant wavelength for a given voltage change. By operating the system at a bias of $\sim 5.7\,V$, sensitivities as large as $50\,nm/V$ can be measured. In other words, in this regime, as little as a $5\,mV$ change in the bias voltage would result in a wavelength change larger than the full-width at half-maximum (FWHM $\sim 0.1\,nm$) of the cavity resonance. This is advantageous for the realization of applications such as low power optical switches and reconfigurable filters/routers. The high sensitivity of our devices can be attributed to two factors: (i) the dependence of the wavelength shift on the change in separation is intrinsically nonlinear, and much larger shifts are obtained as the

nanobeam separation becomes smaller, as in the case of higher voltages; (ii) the electrostatic force experienced by the nanobeams is quadratic with the applied bias voltage as well as inversely proportional to the nanobeam separation. At this point it is worth clarifying that the stiffness of the nano-beams are heavily dependent on their geometries. This means that by making the beams thinner or longer the sensitivity ($d\lambda/dV$) can be increased significantly. However, the tuning mechanism would not have changed. Additionally there is a limit to this weakening of the beams because they need to be able to support their own weight and survive the fabrication process. It is important to emphasize that in the steady state, when the system is reconfigured and the nanobeams are deflected to their final position, the system is not drawing any power from the bias source. This is of great practical interest for the realization of reconfigurable devices and systems, as mentioned earlier. The high sensitivities and high Q-factors of coupled-PCNCs are also suitable for precision motion measurements in NEMS devices, since a strong modulation of the optical signal can be achieved, even for tiny displacements of the nanobeams. By utilizing an electrical feed-through port on a scanning electron microscope (SEM), we were able to observe the real-time deflection of the devices due to the applied bias voltage. Figure 3(b) shows SEM images of the two nanobeams with increasing voltages applied across them (refer supplementary material for video). The

images are shown for nanobeams with a large initial separation ($V_{bias} = 0$) of 100 nm, in order to render the motion of the nanobeams more distinctly. The bending of the nanobeams at the center of the structure can easily be observed, and matches well with our theoretical predictions [Fig. 3.1.2b]. After the pull-in voltage [57] is exceeded, the two beams can become permanently stuck together due to van der Waals interactions. Finally, we note that the difference in steady-state performance of our structures when operated in vacuum (inside the SEM chamber) and in the atmospheric conditions (resonant scattering setup) is negligible, as in either case the structure is operated well below the breakdown voltage. An inherent limitation of the speed of this tuning method is the RC time constant(resistance $\times$ capacitance) of the parallel nanobeams. The resistance offered by the silicon nanobeams is on the order of 10^{13} (the resistivity of the SOI device layer is rated at $1 - 10\Omega - cm$), and the capacitance is on the order of 10^{-17} F, resulting in RC time constants in the 100 μs range. Experimentally, however, we observed slower device response (second) which can be attributed to parasitic capacitances (e.g. between large metal contacts and substrate) and resistances (e.g. due to lateral contact between metal and Si). This response time could be readily improved by improving the contact conductivity by doping the silicon. Doping would increase the absorption loss in silicon and limit the Q. Doping concentrations of $10^{18} cm^{-3}$ would limit the Q values to

the order of 10^5, which would be sufficient for most of the switching applications and reduce the resistivity by more than 2 orders of magnitude. More importantly, the performance of the system could be even further improved by utilizing alternative actuation methods such as dielectrophoretic force [58] that do not depend on the RC time constant of the coupled nanobeams. In that case, the response time would be limited by the mechanical response.

3.3 Conclusion

In summary, we have demonstrated reconfigurable optical filters that can be dynamically and reversibly tuned using electrostatic forces over $\sim 10\,nm$ wavelength range when less than $6\,V$ of external bias is applied to the structure. This work will serve as a basis for exciting applications ranging from reconfigurable and programmable photonics (e.g. filters, routers, switches, lasers), motion and mass sensing, RF photonics, and so on. The tuning method is stable and remarkably reproducible, provided that the voltage is not raised beyond the point of pull-in. By allowing precision wavelength trimming of devices, this method also provides higher tolerances for fabrication errors, enabling diverse applications in optomechanics, cavity quantum electrodynamics, and optical signal processing.

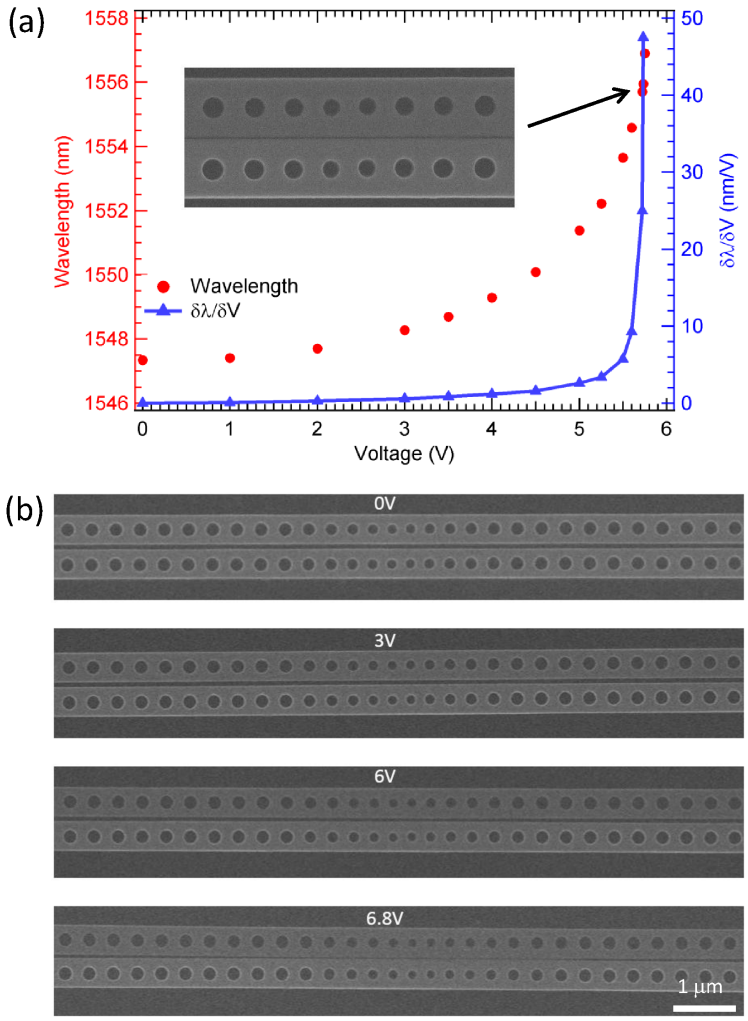

Figure 3.2.2: Sensitivity of the coupled-cavity resonance and the visualization of nanobeam deflection due to applied voltage. a, Experimental results showing the resonant wavelength of the even supermode as the bias voltage is stepped up to $6\ V$ (red curve). Tuning up to $9.6\ nm$ is obtained in this cavity. The blue curve shows the sensitivity of the same cavity resonance to the applied voltage. A high sensitivity of $50\ nm/V$ is obtained when cavity is operated around with a bias $6\ V$. The results are obtained for a cavity with initial ($V\ =\ 0$) nanobeam separation of -70 nm. b, Scanning electron microscopy images showing deflection of a pair of nanobeams under different bias voltages. The lower nanobeam remains grounded, while the potential on the upper nanobeam is increased as indicated

If light can bend objects,

imagine what your mind can do!

4

Optical Gradient Force Reconfiguration

In this chapter, we will discuss a fully integrated, reconfigurable optical filter that can be programmed using internal optical forces. As seen in the earlier chapter, PCNCs [18, 20, 29, 31, 59] are

well suited for the realization of optomechanical systems due to their small footprint, wavelength scale and high quality factor (Q) optical modes [59], small mass, and flexibility. These features allow for manipulation of optical signals as well as mechanical properties of PCNCs at low powers [60], a property which is of interest for dynamic signal filtering, [61] routing, and modulation [62]. We have seen in the earlier chapter that when two such resonators are placed in close proximity their optical modes couple resulting in sharp, wavelength-scale, optical resonances, which can be highly sensitive to the separation between the nanobeams [6, 60, 63]. In addition, the structure supports propagating waveguide modes that can be excited over a wide wavelength range. These waveguide modes give rise to attractive (or repulsive) optical forces between the nanobeams, which in turn affects their mechanical configuration and results in the shift of the optical resonance of the filter [8, 12, 38, 64]. In contrast to previous work, [10, 65–67] this waveguide-pump approach enables the use of broadband source in terms of actuation and tuning of the filter resonance.In addition, the devices are fully integrated and fabricated in a technologically relevant silicon-on-insulator platform. One drawback of Si, when compared to e.g. Si_3N_4 [10, 65–67], is significant two-photon absorption that results in heating of the structure and its thermo-optic tuning. In order to elucidate the interplay between optomechanical and thermo-optic effects on the tunability of the

silicon based optomechanical systems, we propose and demonstrate a novel temperature self-referencing approach that takes advantage of higher order resonances of the structure. Furthermore, slow thermal response time of our device, much slower than optomechanical response time, allows us to explore pure optomechanical effects by operating at high frequencies (higher than thermal cut-off).

4.1 Design

We designed the PCNC's using a deterministic approach [26, 33], with a hole-to-hole spacing of 360 nm, a nanobeam width of 440 nm, and nanobeam separation of 70 nm. The devices were fabricated on a silicon-on-insulator (SOI) substrate with a silicon device layer of 220 nm and a buried oxide layer of 3 μm. For details regarding fabrication please refer to appendix A. A SEM image of the final fabricated device is shown in Fig. 4.1.1 with the inset showing the released cavity region. This region supports propagating and localized modes with even ($TE+$) and odd ($TE-$) symmetry with respect to the x-mirror plane. Mode profiles of localized modes are shown in the inset of Fig. 4.1.2. The dispersion of the even (red color) and odd (blue) mode, plotted in Fig. 4.1.2, as a function of the spacing between the nanobeams shows that the even mode is highly sensitive to the spacing while the odd mode is not [63]. Optomechanical

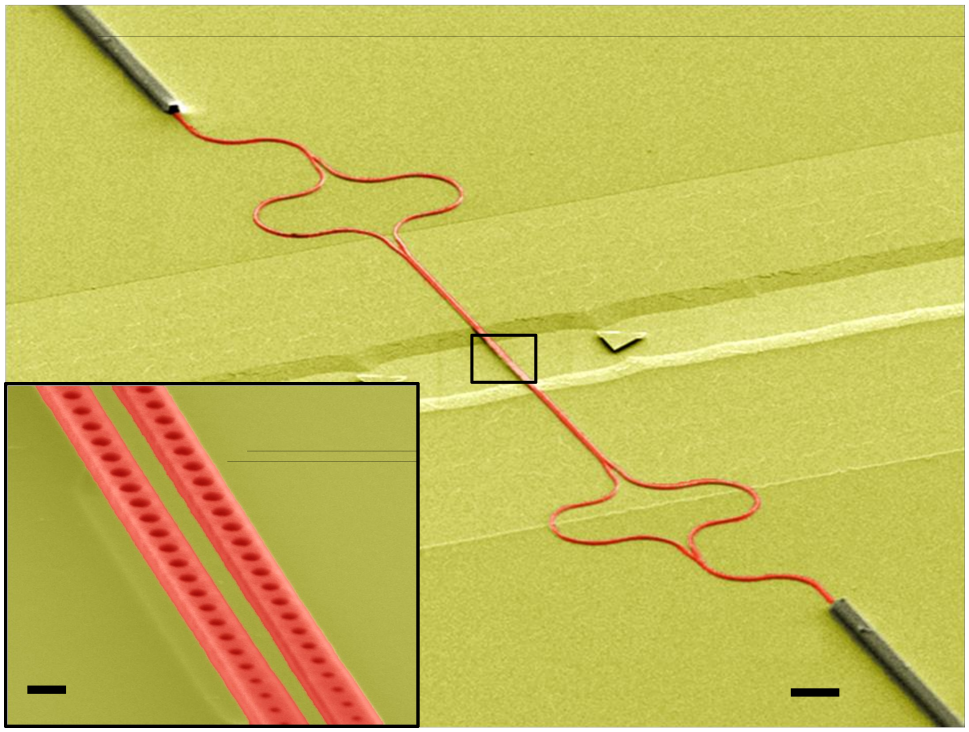

Figure 4.1.1: Scanning electron image of waveguide integrated coupled nanobeam cavities. The image shows the complete device with the SU-8 coupling pads, balanced Mach Zehnder Interferometer (MZI) arms, silicon waveguides and the suspended nanobeam cavity region. Scale bar corresponds to $10\ \mu m$. The inset shows the suspended nanocavity in the region given by the black box (inset scale bar corresponds to 400 nm).

coupling coefficients (g_{om}) were calculated to be $96\,GHz/nm$ for the even mode, and g_{om} of $0.73\,GHz/nm$ for the odd mode (for $70\,nm$ separation). g_{om} is defined as the change in the resonance frequency due to a change in the separation of the coupled nano-beams.

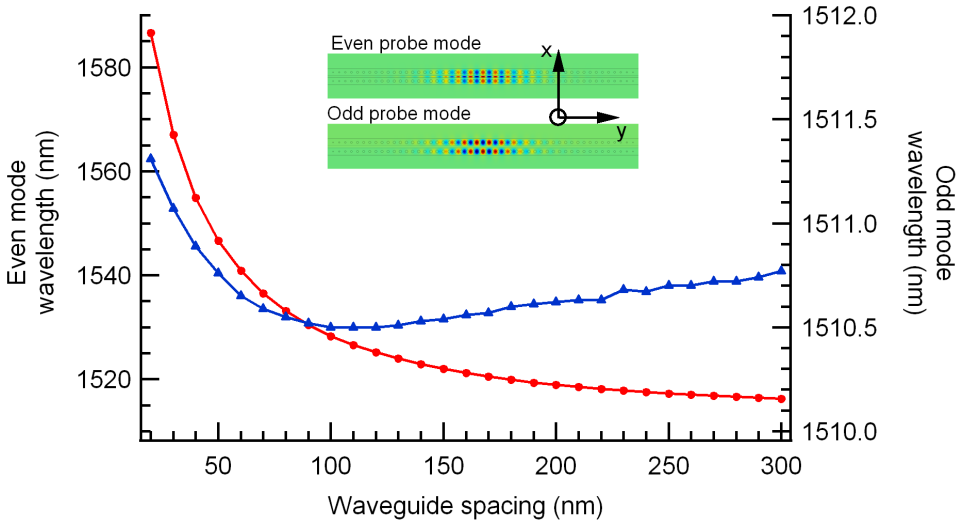

Figure 4.1.2: Dispersion of even and odd mode for various waveguide spacings. The red filled circles and blue filled triangles show the dispersion of the even and odd cavity modes for various spacing between the two cavities. The even mode is highly dispersive while the odd mode is not. The device under test had a gap of $70nm$ corresponding to an optomechanical coupling coefficient (gom) of $96\ GHz/nm$ for the even mode and $0.73\ GHz/nm$ for the odd mode. The inset shows the profiles of dominant electric field component of the two modes. The cavity modes are localized near the center of the nanobeams.

Fig. 4.1.3 shows a theoretical transmission spectrum of the device under excitation by the even symmetry electric-field guided mode, as well as the resulting optical force. If one were to use one of the high-Q modes as the control mode in order to actuate and tune the resonance

wavelength of the filter mode, the localized cavity modes would result in extremely large optical force due to the ultra-high quality factors associated with them [6]. This, however, comes at the expense of a very small operational bandwidth due to self-detuning of the control mode. Furthermore, reconfiguration of the filter results in shift of the high-Q cavity resonance, and wavelength-tracking mechanism is needed to keep the pump laser in tune with the structure. This situation, analogous to common gain-bandwidth trade off issues in electronics (e.g. in amplifiers), can be overcome by taking advantage of broadband waveguide modes [8] supported at the long-wavelength range of our structure, where the optical force is approximately constant over a large wavelength range (Figure 4.1.3).

Our structure therefore combines unique advantages of both waveguide-based [8] and cavity-based [6, 10, 66] optomechanical systems, and has the following unique features: i) The wavelength of the pump beam can be chosen over a wide wavelength range, so wavelength tracking is not needed to keep the pump in tune with the structure during the reconfiguration process. Furthermore, broad-band light sources (such as LEDs) can be used as a pump and the same pump signal can be used to reconfigure a number of filters that operate at different wavelengths (possible applications in filter bank reconfiguration); ii) The wavelength scale, high-quality factor, localized modes have excellent sensitivity to mechanical motion, and

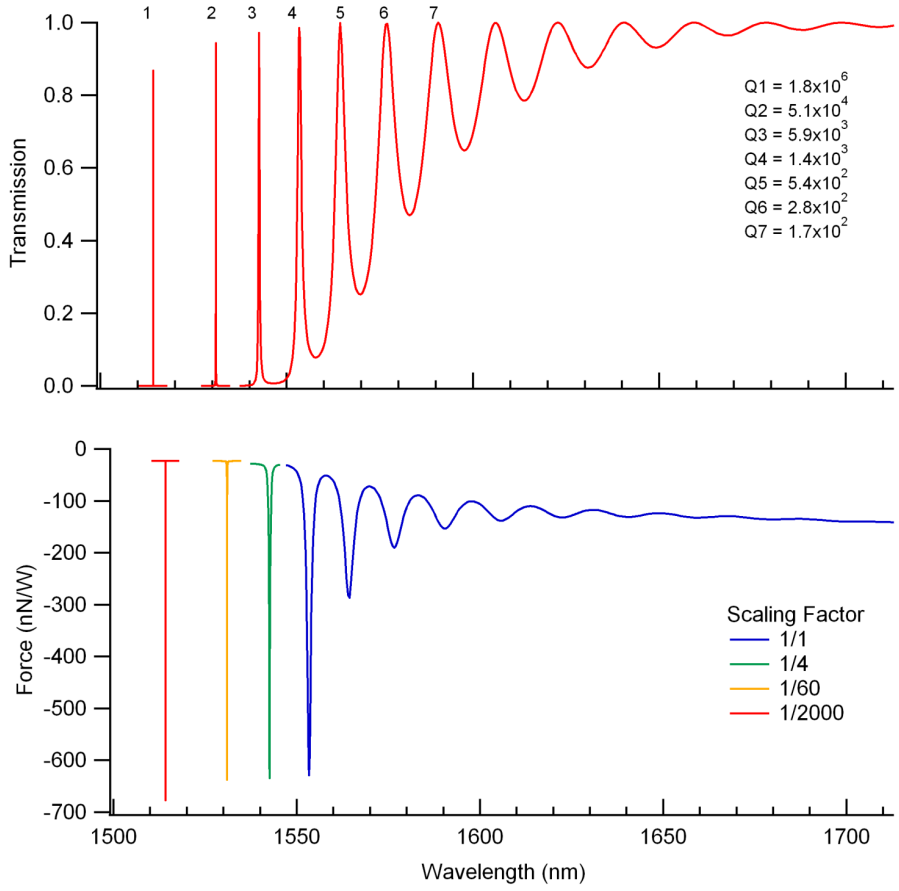

Figure 4.1.3: Simulated transmission and generated optical force for the even electric-field profile. The corresponding optical force is in nN/W generated by the even mode for various pump wavelengths. The negative sign indicates the attractive nature of the force. The force for the first three modes has been rescaled (multiplied by a scaling factor) for better comparison. The transmission spectrum and the mutual optical force between the nano-beams for low-Q modes ($Q < 10^4$) were calculated using finite-element simulations. The two highest-Q modes with quality factors 1.8×10^6 and 5.1×10^4 were treated using temporal coupled mode theory.

tuning over several filter linewidths can be achieved using modest pump powers. Therefore operation at mechanical resonances (which also can require operation in vacuum) is not required [8]. iii) Independent control of optical and mechanical degrees of freedom (optical and mechanical resonance) of the structure is possible; iv) An inherent temperature self-referencing scheme can be used to individually evaluate the contributions from thermo-optical and optomechanical effects to the observed detuning in our filters. We do this by taking advantage of cavity modes with odd lateral symmetry which are in-sensitive to mechanical reconfiguration (Fig. 4.1.2) [60, 63], but have comparable thermo-optic sensitivities comparable to the even cavity modes.

4.2 Optomechanical Coupling Coefficient (g_{om})

Optomechanical coupling coefficient (g_{om}) is defined as the change in the resonance frequency due to a change in the separation of the coupled nanobeams. Frequency noise calibration technique with a direct detection method was used to experimentally determine g_{om} and verify the accuracy of our theoretical model. A calibration signal of known modulation depth was generated by modulating the probe using a phase modulator at a frequency close to the mechanical resonance as shown in Fig. 4.2.1. It must be noted that a phase

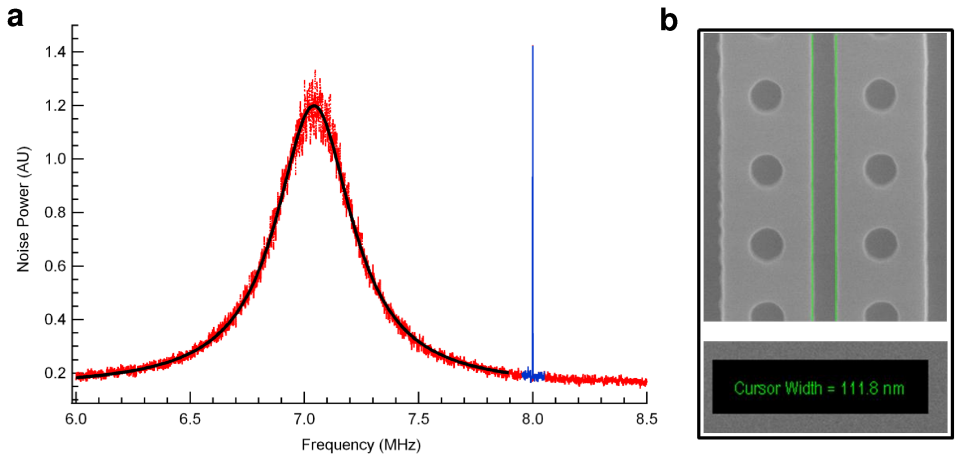

Figure 4.2.1: Measurement of optomechanical coupling coefficient. (a) Power spectral density spectrum showing the fundamental mechanical mode along with the calibration signal. The black line is the Lorentzian fit for the mechanical mode while the blue line is a Gaussian fit for the calibration signal. g_{om} was estimated to be 35 GHz/nm (b) SEM image of the device used for g_{om} measurement.

modulator is essential and cannot be substituted by an amplitude modulator. The peak amplitude of the calibration signal and the mechanical resonance was noted. A correction to the measured mechanical resonance peak as reported in ref [68] was applied before estimating the g_{om}. The gap between the nanobeams for the device under test was measured to be 111.8 nm. The theoretical value of g_{om} for this gap was $38 \pm 3\, GHz/nm$ (error associated due to measuring dimensions from SEM image). The measured value obtained using the noise calibration approach was found to be 35 GHz/nm. Such excellent agreement between the experimental and simulation value confirms the accuracy of our model and justifies the use of the

theoretically calculated value of g_{om} in our modeling. We note that g_{om} increases as the separation between nanobeams decreases. For example, if the gap is reduced to $70\,nm$, g_{om} increases to $96\,GHz/nm$

4.3 Static Measurement

The devices were probed using the butt coupling technique with two lensed fibers. Unlike tapered fiber probing [42], this type of characterization method remains invariant under any mechanical oscillations of the suspended waveguides and can be easily integrated for on-chip applications. Light from a tunable laser was amplified using an Erbium doped fiber amplifier (EDFA) and used as the pump while another tunable laser was used to probe the structure. A schematic of the experimental setup is shown in Fig. 4.3.1a.

A measured transmission spectrum of the device (a device similar to the one shown in Fig. 4.1.1a) is shown in Fig. 4.3.1b with the fundamental even mode at $1507.72\,nm$ (The slight discrepancy in the measured and simulated resonance wavelength shown in Fig. 4.1.3 is due to the error associated in the measurement of device dimensions using a SEM image). The shaded portion under the transmission curve denotes the pump region which lies outside the bandgap of the photonic crystal. We note that due to the limited tuning range of the pump EDFA, in our experiments the pump is not positioned in the

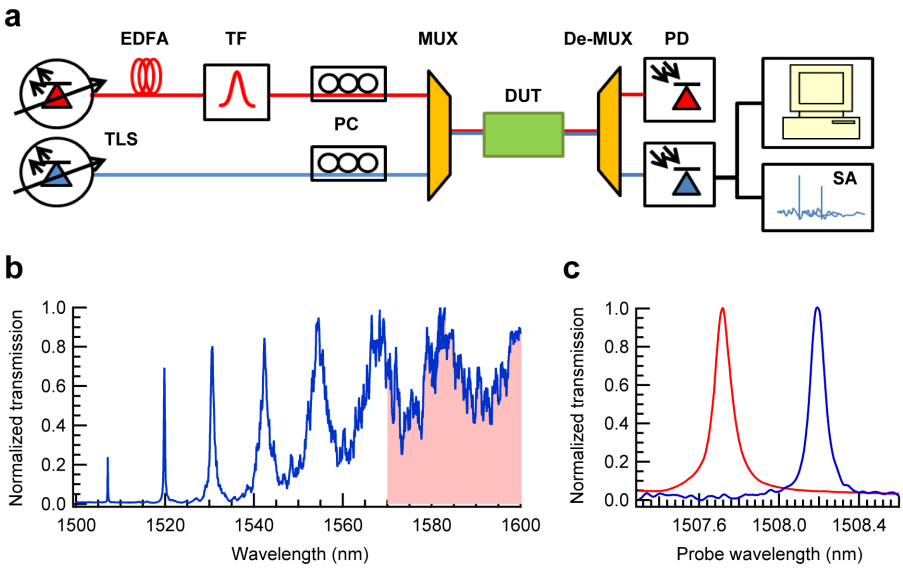

Figure 4.3.1: Experimental results for waveguide pump, cavity-probe system. (a) Schematic of the pump-probe characterization setup used in the experiment. The cavity resonance was probed using a tunable laser (Santec TLS 510) and a fast, sensitive InGaAs detector (New Focus). Another tunable laser was used as the pump and was amplified using a high power output EDFA (L Band Manlight). The input and output WDMs (wavelength division multiplexer) (Micro Optics) ports were designed to operate in the $1470 - 1565\,nm$ and $1570 - 1680\,nm$ ranges. The mechanical response of the devices was studied using a real time spectrum analyzer (Tektronix RSA 3300). TLS: tunable laser source, EDFA: Erbium doped fiber amplifier, TF: tunable filter, PC: polarization controller, MUX: multiplexer, De-MUX: de-multiplexer, PD: photo detector, DUT: device under test, SA: spectrum analyzer. (b) A transmission spectrum of the fabricated cavity. The transmission has been normalized to the maximum value outside the bandgap. The fundamental even mode is found to be near $1507\ nm$ with a Q of 15000. The shaded region shows the operating range of the EDFA used to amplify the pump. The pump has a waveguide like mode profile since it is outside the bandgap and is used to induce mechanical deformation to detune the even mode cavity resonance. (c) Cavity resonance was tuned from $1507.72\,nm$ to $1508.19\,nm$ when $6\,mW$ of pump power at $1583\,nm$ was used. Red and blue curves correspond to $0\,mW$ and $6\,mW$ of pump power. The transmission in this case has been normalized to the maximum value of the cavity resonance. Cavity tuning was due to contribution from thermo-optical, nonlinear optical and optomechanical effects.

flat part of the transmission spectrum. Therefore, the pump benefits from the light confinement and low-Qs of extended resonances of the structure (broad peaks in the transmission spectrum). Based on theoretical predictions, we estimate that the force associated with this effect is approximately twice as big as the force in the "flat" part of the spectrum (Fig. 4.1.3c). When the pump laser excites only the even mode, an attractive optical force is generated which reduces the separation between nanobeams and red-detunes the even probe mode. Fig. 4.3.1c shows the experimental detuning of the fundamental even mode with a $6\,mW$ pump (estimated power inside the waveguide just before the photonic crystal) at $1583\,nm$. This detuning is in part due to optomechanical (OM) effects, and in part due to the combination of thermo-optic (Th), free carrier dispersion (FCD) and Kerr effects. The overall detuning of the modes is given by:

$$\Delta_c' = \Delta_c^{Th} + \Delta_c^{FCD} + \Delta_c^{Kerr} + \Delta_c^{OM} \tag{4.1}$$

We modeled our structure by using a two-mode, temporal,

coupled-mode theory [69]:

$$\frac{da_c}{dt} = i\Delta'_c a_c - \frac{\Gamma'_c}{2} a_c + \sqrt{\Gamma_c^{wg} s_c^{in}} \tag{4.2}$$

$$\frac{da_p}{dt} = i\Delta'_p a_p - \frac{\Gamma'_p}{2} a_p + \sqrt{\Gamma_p^{wg} s_p^{in}} \tag{4.3}$$

$$\Gamma'_c = \Gamma_c^0 + \beta_c |a_c|^2 + \beta_{cp} |a_p|^2 + \alpha_c^{cc} N^{cc} + \alpha_c^{pp} N^{pp} + \alpha_c^{cp} N^{cp} \tag{4.4}$$

$$\Delta'_c = \omega_c^l - \omega_c^0 + \Delta_c^{TH} + \Delta_c^{FCD} + \Delta_c^{\chi^{(3)}} + \Delta_c^{Mech} \tag{4.5}$$

$$\Gamma'_p = \Gamma_p^0 + \beta_p |a_p|^2 + \beta_{pc} |a_c|^2 + \alpha_p^{cc} N^{cc} + \alpha_p^{pp} N^{pp} + \alpha_p^{cp} N^{cp} \tag{4.6}$$

$$\Delta'_p = \omega_p^l - \omega_p^0 + \Delta_p^{TH} + \Delta_p^{FCD} + \Delta_p^{\chi^{(3)}} + \Delta_p^{Mech} \tag{4.7}$$

where subscripts c and p refer to the high-Q probe mode and low-Q pump mode, respectively.$|a_{c,p}|^2$ are the energies stored in the respective modes, $|s_{c,p}^{in}|^2$ are equal to the input powers. $\Gamma'_{c,p}$ characterizes the decay rate of the stored energy in the optical modes, whereas $\Delta'_{c,p}$ are the detuning of the input laser frequency with respect to the resonant frequencies of the respective modes. The following effects, which are relevant to silicon at telecommunication wavelengths have been included: degenerate two-photon absorption ($\beta_{c,p}|a_{c,p}|^2$), non-degenerate two photon absorption ($\beta_{cp,pc}|a_{p,c}|^2$), free carrier absorption ($\alpha_{c,p}^{cc} N^{cc} + \alpha_{c,p}^{pp} N^{pp} + \alpha_{c,p}^{cp} N^{cp}$), thermal dispersion $\Delta_{c,p}^{TH}$, free-carrier dispersion ($\Delta_{c,p}^{FCD}$), self-phase and cross-phase modulation ($\Delta_{c,p}^{\chi^{(3)}}$), and optomechanical detuning ($\Delta_{c,p}^{Mech}$) in our

model. Γ_c' includes the cold cavity decay rates (waveguide coupling, scattering, and linear absorption), and non-linear absorption rates (degenerate ($\beta_c|a_c|^2$) and non-degenerate two-photon absorption ($\beta_{cp}|a_p|^2$), and free-carrier absorption rates ($\alpha_{c,p}^{cc}N^{cc} + \alpha_c^{pp}N^{pp} + \alpha_c^{cp}N^{cp}$) due to the free-carriers generated by two-photon absorption of the probe and pump mode photons). The non-linear absorption terms can be expressed in terms of effective mode parameters [70]. For instance, the modal degenerate two-photon absorption coefficient can be written as:

$$\begin{aligned} \beta_c &= \frac{\Gamma_c^{TPA}\beta_{Si}c^2}{V_c^{TPA}n_g^2} \\ \Gamma_c^{TPA} &= \frac{\int_{Si} \epsilon^2(r)E_c^4(r)dv}{\int \epsilon^2(r)E_c^4(r)dv} \\ V_c^{TPA} &= \frac{\left[\int \epsilon(r)E_c^2(r)dv\right]^2}{\int \epsilon^2(r)E_c^4(r)dv} \end{aligned} \tag{4.8}$$

where β_{Si} is the bulk degenerate two-photon absorption coefficient. The modal non-degenerate two photon absorption coefficient can be

written as:

$$\begin{aligned}
\beta_{cp} &= \frac{\Gamma_{cp}^{TPA} 2\beta_{Si} c^2}{V_{cp}^{TPA} n_g^2} \\
\Gamma_{cp}^{TPA} &= \frac{\int_{Si} \epsilon^2(r) E_c^2(r) E_p^2(r) dv}{\int \epsilon^2(r) E_c^2(r) E_p^2(r) dv} \\
V_c^{TPA} &= \frac{\left[\int \epsilon(r) E_c^2(r) dv\right] \left[\int \epsilon(r) E_p^2(r) dv\right]}{\int \epsilon^2(r) E_c^2(r) E_p^2(r) dv}
\end{aligned} \tag{4.9}$$

Note that the bulk non-degenerate two-photon absorption coefficient is twice the degenerate two-photon absorption coefficient [71]. In steady state, the free-carrier absorption rates can be expressed in terms of the stored energies and effective modal parameters. We assume a simplified model of carrier generation and diffusion such that the carriers generated by two-photon absorption of the pump and probe modes are treated independently. For instance, $\alpha_c^{cc} N^{cc}$, the free-carrier absorption rate of the probe mode due to the free-carriers generated by the two photon absorption of the probe photons, can be written as $\gamma_c^{cc} |a_c|^4$, where

$$\begin{aligned}
\gamma_c^{cc} &= \frac{\tau_{fc} \sigma_{Si} c \Gamma_c^{cc,FCA}}{n_g V_c^{cc,FCA}} \frac{\beta_{Si} c^2}{n_g^2 2\hbar\omega_c^0} \\
\Gamma_c^{cc,FCA} &= \frac{\int_{Si} \epsilon^3(r) E_c^6(r) dv}{\int \epsilon^3(r) E_c^6(r) dv} \\
V_c^{cc,FCA} &= \frac{\left[\int \epsilon(r) E_c^2(r) dv\right]^3}{\int \epsilon^3(r) E_c^6(r) dv}
\end{aligned} \tag{4.10}$$

Similarly, $\alpha_c^{pp} N^{pp}$, the free-carrier absorption rate of the probe mode due to the free-carriers generated by the two photon absorption of the pump photons , can be written as $\gamma_c^{pp}|a_p|^4$, where

$$\begin{aligned}
\gamma_c^{pp} &= \frac{\tau_{fc}\sigma_{Si}c\Gamma_c^{pp,FCA}}{n_g V_c^{pp,FCA}} \frac{\beta_{Si}c^2}{n_g^2 2\hbar\omega_p^0} \\
\Gamma_c^{pp,FCA} &= \frac{\int_{Si} \epsilon^3(r) E_c^2(r) E_p^4(r) dv}{\int \epsilon^3(r) E_c^2(r) E_p^4(r) dv} \\
V_c^{pp,FCA} &= \frac{\left[\int \epsilon(r) E_c^2(r) dv\right] \left[\int \epsilon(r) E_p^2(r) dv\right]^2}{\int \epsilon^3(r) E_c^2(r) E_p^4(r) dv}
\end{aligned} \tag{4.11}$$

The detuning term is much more complicated and has a richer structure. The contribution due to the free-carrier dispersion can be decomposed into their respective free-carrier source terms: degenerate two photon absorption of the pump and probe modes, and the non-degenerate two-photon absorption:

$$\Delta_c^{FCD} = \Delta_c^{cc,FCD} + \Delta_c^{pp,FCD} + \Delta_c^{pc,FCD} \tag{4.12}$$

In steady state, we can express eqn. 4.11 as:

$$\Delta_c^{FCD} = g_c^{cc,FCD}|a_c|^4 + g_c^{pp,FCD}|a_p|^4 + g_c^{pc,FCD}|a_c|^2|a_p|^2 \tag{4.13}$$

where,

$$
\begin{aligned}
g_c^{cc,FCD} &= -\frac{\omega_c^0 \zeta_{Si,e} \tau_{fc} \beta_{Si} c^2 \Gamma_c^{cc,FCD}}{2\hbar\omega_c n_{Si} n_g^2 V_c^{cc,FCD}}, & \frac{\Gamma_c^{cc,FCD}}{V_c^{cc,FCD}} &= \frac{\Gamma_c^{cc,FCA}}{V_c^{cc,FCA}} \\
g_c^{pp,FCD} &= -\frac{\omega_c^0 \zeta_{Si,e} \tau_{fc} \beta_{Si} c^2 \Gamma_c^{pp,FCD}}{2\hbar\omega_p n_{Si} n_g^2 V_c^{pp,FCD}}, & \frac{\Gamma_c^{pp,FCD}}{V_c^{pp,FCD}} &= \frac{\Gamma_c^{pp,FCA}}{V_c^{pp,FCA}} \\
g_c^{cp,FCD} &= -\frac{\omega_c^0 \zeta_{Si,e} \tau_{fc} 2\beta_{Si} c^2 \Gamma_c^{cp,FCD}}{\hbar(\omega_p + \omega_c) n_{Si} n_g^2 V_c^{cp,FCD}}, & \frac{\Gamma_c^{cp,FCD}}{V_c^{cp,FCD}} &= \frac{\Gamma_c^{cp,FCA}}{V_c^{cp,FCA}}
\end{aligned}
\tag{4.14}
$$

The above equations explain FCD contribution from electrons. Note that there is a similar contribution from holes with $(N^{-0.8})$ dependence. The contribution due to optomechanical detuning can be written as:

$$
\begin{aligned}
\Delta_c^{Mech} &= -g_{om}^c x \\
\Delta_c^{Mech} &= \frac{(g_{om}^c)^2 |a_c|^2}{\Omega_M^2 m_{eff} \omega_c^0} + \frac{g_{om}^c g_{om}^p |a_p|^2}{\Omega_M^2 m_{eff} \omega_p^0}
\end{aligned}
\tag{4.15}
$$

where x is the displacement amplitude of the optically bright mechanical mode, g_{om} is the optomechanical coupling constant, Ω_M is the mechanical eigen-frequency, and m_{eff} is the effective mass of the mechanical mode. The choice of the displacement amplitude x, is somewhat arbitrary. We have adopted the convention introduced in [72]. The Optomechanical coupling constant is calculated from perturbation theory of shifting boundaries [72, 73]. For the device

under test, g_{om} was found to be 96 GHz/nm for the even mode. Note that we have ignored the beat terms between the pump and probe modes. This is justified within the rotating wave approximation because the frequency separation between the pump and probe modes are much larger than the mechanical frequency. We also verified that the above equation describes the displacement of the nano-beams due to the optical forces correctly. The forces due to an excitation of the pump or probe mode were calculated and applied as a boundary load in FEM simulations. The displacement obtained from the FEM simulations was compared to the above model. Both the methods agree within $2-5\%$, which is well within the numerical accuracy of the calculations.

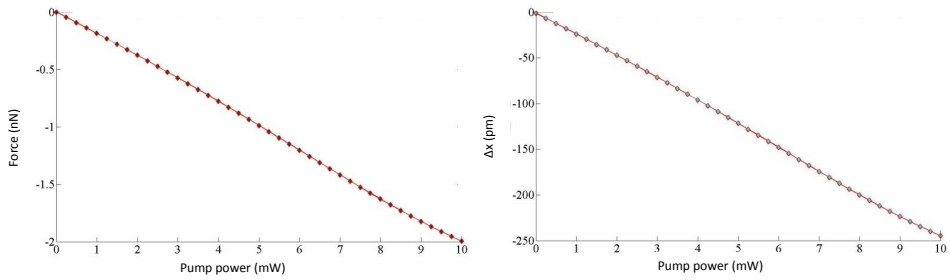

Figure 4.3.2: Estimated force and displacement for various pump power. (power inside the waveguide just before the cavity). Negative value of force indicates its attractive nature. The negative displacement indicates that the separation between the nanobeams us reduced confirming the attractive nature of the force.

We also consider both self-phase modulation and cross-phase

modulation due to the Kerr effect:

$$\Delta_c^{Kerr} = \chi^c |a_c|^2 + \chi^{cp} |a_p|^2 \tag{4.16}$$

where the first term is due to the self-phase modulation and the second term is due to cross-phase modulation. And

$$\begin{aligned} \chi^c &= \frac{\omega_c^0 \Gamma_c^{Kerr} n_{2,Si} c}{n_{Si} V_c^{Kerr} n_g}, \Gamma_c^{Kerr} = \Gamma_c^{TPA}, V_c^{Kerr} = V_c^{TPA} \\ \chi^{cp} &= \frac{\omega_c^0 \Gamma_{cp}^{Kerr} 2 n_{2,Si} c}{n_{Si} V_c p^{Kerr} n_g}, \Gamma_{cp}^{Kerr} = \Gamma_{cp}^{TPA}, V_{cp}^{Kerr} = V_{cp}^{TPA} \end{aligned} \tag{4.17}$$

Finally, the thermal dispersion can be written as:

$$\begin{aligned} \Delta_c^{TH} &= \frac{\omega_c^0 \Gamma_c^{th}}{n_{Si}} \frac{dn_{Si}}{dT} (T_c + T_p) \\ \Gamma_c^{th} &= \frac{\int_{Si} \epsilon(r) E_c^2(r) dv}{\int \epsilon(r) E_c^2(r) dv} \\ T_{c,p} &= R_{c,p}^{th} P_{abs} \left(|a_{c,p}|^2 \right) \end{aligned} \tag{4.18}$$

where, $T_c(T_p)$ is the temperature change due to the absorption of the probe photons (pump photons). $R_{c,p}^{th}$ is the thermal resistance of the structure when the heat is generated due to photons absorbed from the respective probe or pump modes. $P_{abs}(|a_{c,p}|^2)$ is the total power absorbed from the respective modes. The thermal resistances for both modes were estimated from FEM simulations. A thermal conductivity

of 20 W/mK was used in FEM simulations. This value was further confirmed by comparing FEM simulations with thermal time constant measurements shown in Fig. 4.3.3.

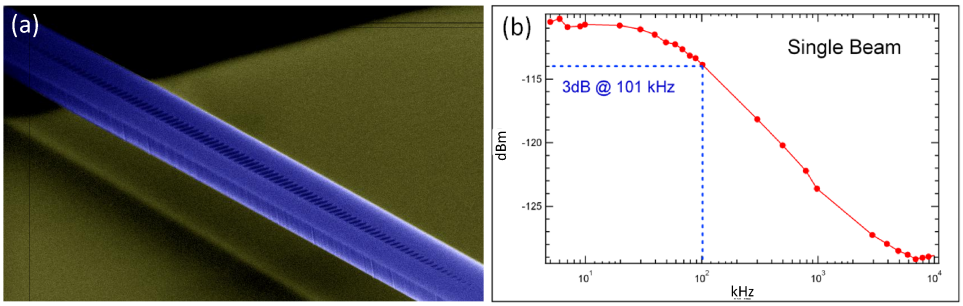

Figure 4.3.3: Thermal response of suspended nanobeam cavities.(a) SEM image of the single PCNC used in the experiment. (b) Amplitude of the frequency response of the device. Thermal cutoff frequency is around 100 kHz.

The thermal conductivity in thin and unpatterned SOI samples was measured by several groups, and it was found that the thermal conductivity strongly depends on the thickness of the sample [74–76]. A thermal conductivity of 40 W/mK has been reported for 115 nm thick silicon samples [74], which is 4 times smaller than that of bulk Si. We expect an even smaller effective thermal conductivity in our devices due to the patterning. A thermal conductivity as low as 15 has been reported for poly-silicon samples with 210 nm grains, which is of a similar length scale as our feature dimensions. In our device, the mean hole-to-hole separation was around 170 nm and the mean distance between the edge of the nano-beam and the holes was 125 nm. The thermal time constant measurements shown in Fig. 4.3.3

were obtained using a single PCNC. The pump was modulated sinusoidally and a probe laser was fixed at the maximum slope of the fundamental resonance. The probe signal was analyzed using an electrical spectrum analyzer. The detuning in this case was caused only due to thermo-optic effects. FEM simulations were used to extract the value of thermal conductivity of $20\,W/mK$ which was ~ 8 times smaller than the bulk value.

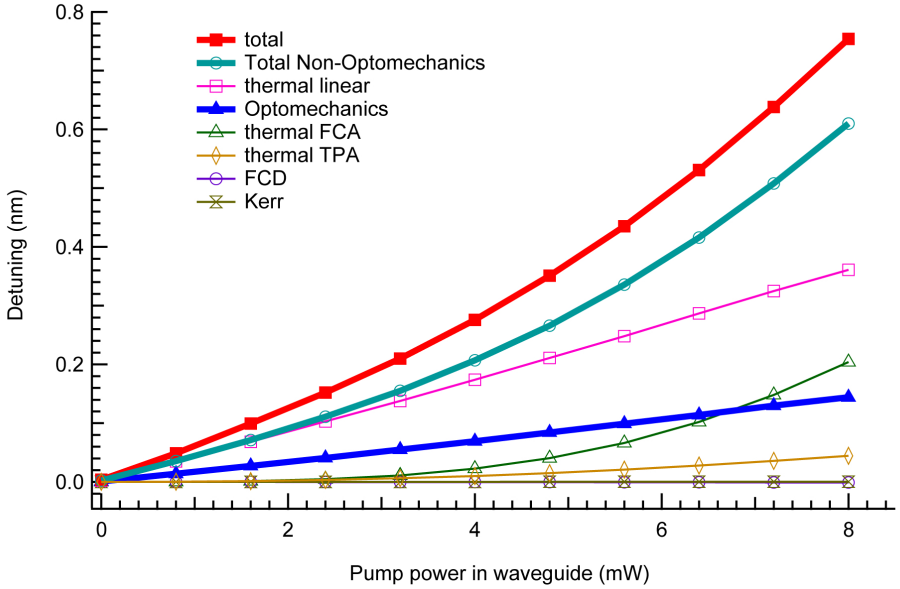

Figure 4.3.4: Estimated probe detuning contributions for different pump powers. (Power in the waveguide just before photonic crystal cavity). The estimated optomechanical contribution is slightly more than 20% of the total detuning. Linear and thermal free carrier absorptions are the most dominant contributors to the detuning.

The transmission properties and the detuning of the probe mode are determined from the steady-state solutions of eqns. 4.2 and 4.3. The

list of parameters used in our calculations is summarized in table 4.6.1 and the estimate for different detuning is plotted in Fig. 4.3.4. We see that in addition to optomechanical detuning, thermo-optic effects play an important role in the detuning of the cavity resonance (both even and odd modes shift towards longer wavelengths with increasing temperature). Due to the nonlinear dependence of thermo-optic effect on pump power, its contribution increases at higher powers, while the optomechanical effect remains linear.

In order to decouple thermal and mechanical effects, we used an odd localized mode of the cavity as an on-chip temperature reference. This is possible since this mode's resonance does not tune with mechanical motion (Fig. 4.1.2b), and tunes only with temperature. This was determined experimentally by measuring the resonance frequency of both the even and odd modes as a function of temperature. The sample was placed on a thermo-electric heater and the temperature on the sample surface was measured. The ratio of wavelength detuning with temperature of the two modes was determined from the slope of the temperature versus detuning curves. The experimentally determined value of tuning ratio of the even mode to the odd mode was found to be 0.93.

Our devices support both highly localized cavity modes with large Q-factors and extended waveguide-like modes with low Q-factors. Due to the symmetry of the structure with respect to mirror plane in the

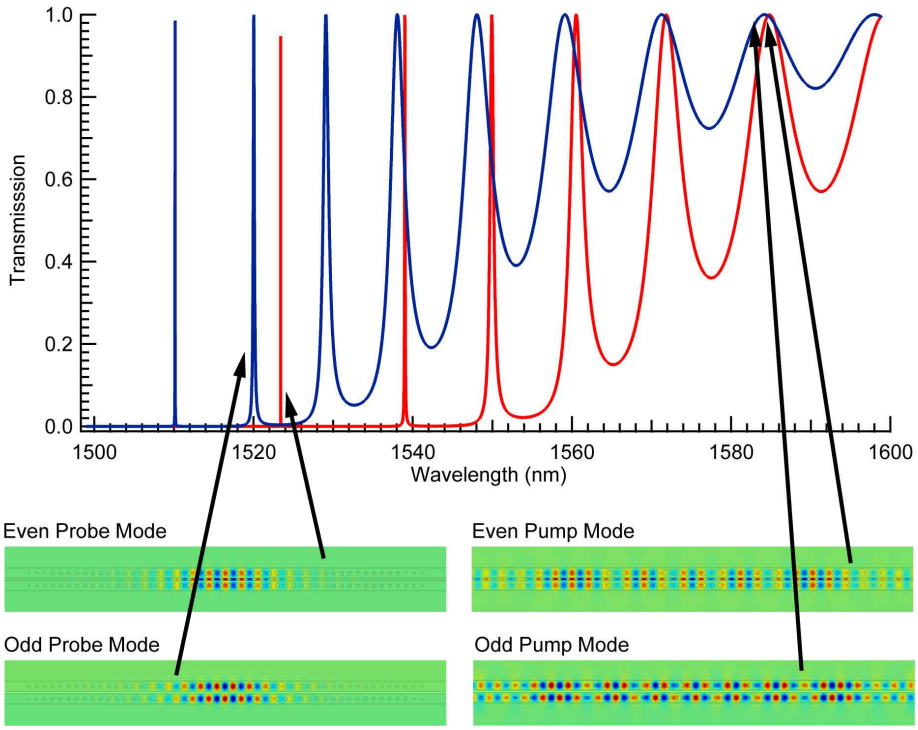

Figure 4.3.5: Theoretical transmission spectrum for even and odd symmetries. Simulation of the optical transmission of an actual device when excited with the even (red) and odd (blue) symmetry mode. The dimensions were determined with scanning-electron microscopy (SEM) measurements, and the measured dimensions were used in finite-element (FEM) simulations. The plots also show the electric fields associated with high-Q probe and low-Q pump modes. The probe modes are localized while the pump modes are extended and resemble waveguide like modes.

middle of the gap (perpendicular to the substrate), both localized and extended modes have either even or odd symmetry (refer Fig. 4.3.5). The bottom plots in Fig. 4.3.5 show the electric fields associated with high-Q probe and low-Q pump modes. The probe modes are localized while the pump modes are extended and resemble waveguide like modes.

In order to simultaneously excite the even and the odd probe modes, and use the odd cavity mode as a built-in temperature reference, we incorporated an unbalanced Mach Zehnder Interferometer (MZI) (refer Fig. 4.3.6a) at the input of the device (200 μm path difference). An unbalanced MZI generates a phase difference between its output arms. This phase difference depends on the wavelength and the difference between the lengths of the MZI arms. When the phase difference is 0, the even mode is excited, and when the phase is π the odd mode is excited. For a phase difference in the range between 0 and π both even and odd modes are excited. The signal at the output (after the cavities) from each of the waveguides was collected without combining them. This allowed us to excite and collect both even and odd modes of the structure. This scheme is also useful to actuate the device using odd pump mode and generate repulsive force. However, the g_{om} resulting from odd modes is extremely small and the repulsive force will cause very small, un-measurable, shifts in cavity resonance due to the optomechanics.

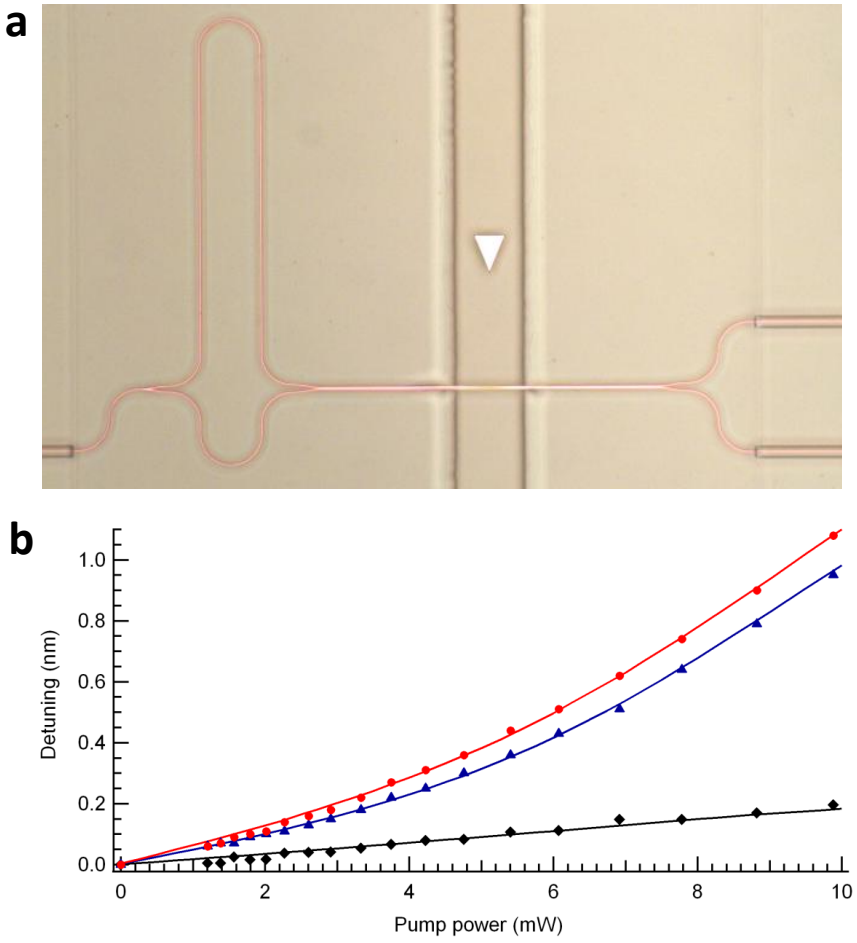

Figure 4.3.6: Evaluation of optomechanical effect using temperature self-referencing. (a) Optical micrograph of a device with an unbalanced MZI for simultaneous measurement of both the even and odd modes. Scale bar corresponds to $20\,\mu m$. (b) Tuning of the cavity resonance for various pump powers and fixed pump wavelength of $1573.5\,nm$. The filled red circles and filled blue triangles correspond to even and odd modes while the filled black diamonds show the optomechanical detuning of the even mode. The latter was obtained by first determining the ratio of detuning for the even and odd modes due to purely thermal effects, by heating the sample (see Methods). Since the odd mode was sensitive only to temperature, it was used as a temperature sensor and the even mode temperature detuning was estimated using the above ratio and subtracted from the total detuning of the even mode. Using this self-referencing technique we estimated that more than $20\,\%$ of the total tuning is due to purely optomechanical effects.

The measured transmission spectrum through a device with an input MZI is shown in Fig. 4.3.7a along with the simulated transmission. The spectrum consists of the even/odd MZI fringes superimposed on the even/odd transmission spectrum of the cavity. The fundamental odd and even modes were found to be at 1510.1 nm and 1524.48 nm, respectively.

Fig. 4.3.6a shows an optical micrograph of the new configuration with unbalanced MZI. In this case the cavity resonance (even mode) was at 1524.9 nm. Fig. 4.3.6b shows the experimentally measured detuning of the probe modes (even and odd) for various pump powers (estimated power inside the waveguide just before the photonic crystal) and pump wavelength of 1573.5 nm. The change in the resonances of both the even and odd modes are denoted with red circles and blue triangles respectively, while the shift resulting solely from the optomechanical effect is shown with black diamonds. The latter was obtained as proportional difference of the shifts of even and odd modes. The solid lines in Fig. 4.3.6b were obtained using Eqn. 4.1. Thermal, FCD, Kerr and optomechanical contributions of the pump and probe along with the cross coupling terms were included. The change in stored energy due to self-detuning of the pump was also computed and included in the estimation. The significance of thermo-optic effects is clearly seen, and 80 % of tuning can be attributed to this effect. Therefore, in contrast to Si_3N_4 based

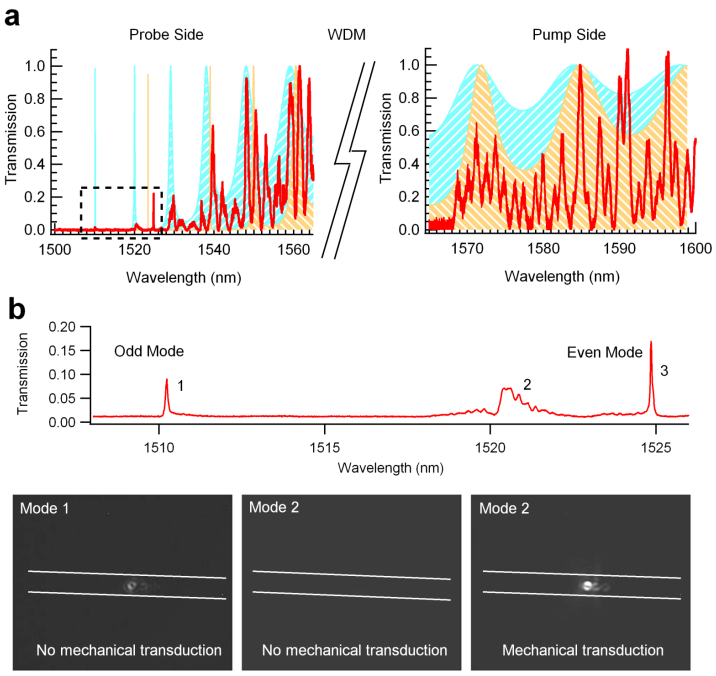

Figure 4.3.7: Even and odd mode excitation using unbalanced Mach Zehnder Interferometer (MZI). (a) Experimental transmission spectrum through a device with an unbalanced MZI at the input. Superimposed on it is the simulated transmission. The actual transmission is the even/odd MZI fringes enveloped by even/odd transmission of the cavity. The two spectra correspond to each side of the WDM filter arm. It should be pointed out that the y-axis in both the cases is different. Hatched blue and orange region denote odd and even mode simulated transmissions respectively while the red curve shows the experimental transmission. (b) Zoomed area denoted by dashed rectangle in panel *a* showing the measured even and odd modes. The fundamental odd and even modes were found to be at $1510.1\,nm$ and $1524.48\,nm$, respectively. The broad resonance around $1520.5\,nm$ is possibly the higher order odd mode. We confirmed the even and odd modes by imaging them from top using a sensitive IR camera. The images show the localized nature of the modes. The two white lines indicate the boundary of the two beams. In order to confirm the symmetry of the localized modes, we used them to transduce mechanical motion of the beams due to Brownian motion. The even mode is expected to have good transduction properties (due to large gom) while the odd mode is expected to have poor transduction property. Mechanical transduction was observed only with the mode at $1524.48\,nm$. In addition, odd mode is expected to be found at shorter wavelengths, based on the FDTD simulations.

optomechanical structures, Si-based ones do suffer from significant two-photon absorption induced thermo-optic effects.

One way of reducing the relative contribution of thermo-optical effects in our devices is to improve g_{om} by using nanobeams with smaller gaps. This however, is challenging with our current fabrication capabilities. Another method is to excite the structure with pulsed pump beam with repetition rates faster than the thermal response (measured value: $100\,kHz$) but lower than the mechanical resonance of the structure (measured: $6.7\,MHz$). In this way, the structure would thermalize and would not be able to respond to changes in temperature, and the optomechanical effects would remain as the dominant tuning mechanism. Importantly, such dynamic, modulated, operation closely resembles the situation found in practice, including optical circuit switching and optical burst switching, where optical circuits are reconfigured with frequencies typically larger than our thermal cut-off frequency. Thermal cut-off and mechanical resonance frequencies define three distinct operating regimes of our structure (refer Fig. 4.3.8). In Region 1 the operating frequency is below the thermal cutoff frequency and both thermo-optical and optomechanical effects can follow the modulation resulting in resonance tuning over wide wavelength range. In Region 2 the operating frequency is larger than the thermal cutoff frequency but smaller than mechanical resonance and the response is entirely

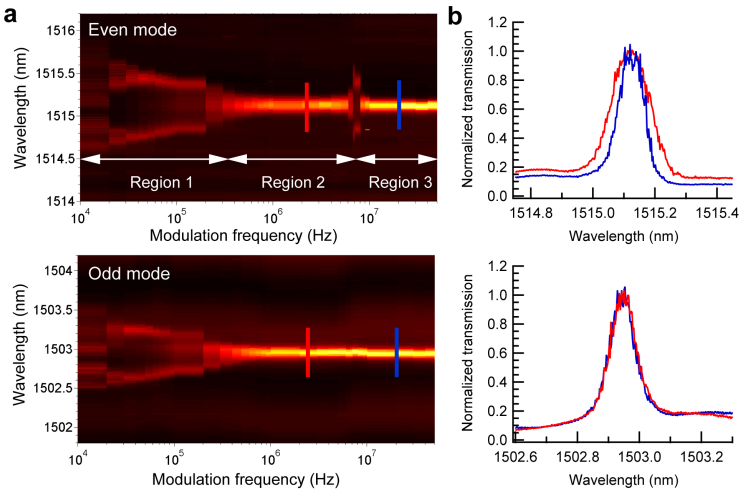

Figure 4.3.8: Detuning of the even and odd modes for pulsed pump operation. (a) Three regions of operation, defined by the thermal cut-off and mechanical cut-off frequencies can be identified. Region 1 denotes the regime where thermo-optic and optomechanical effects are prominent as structure can respond both thermally and mechanically to the modulation signal. This regime extends from dc operation to thermal cut-off frequency. Here cavity resonance is modulated over wide wavelength range, due to combination of thermal and mechanical effects, and it appears smeared-out by the slow detector. Region 2 denotes the regime above the thermal cut-off frequency, where the thermal effects settle to a steady state value and only the optomechanical effects are prominent. This regime extends from thermal cut-off to mechanical cut-off frequency. This is precisely the regime where optomechanics is the dominant tuning mechanism. The wavelength smearing is smaller in this region than in Region 1, which is consistent with the observations that thermal effects cause roughly four times more tuning than mechanical effects in the case of DC actuation. Also, as expected there is no smearing in the odd-mode resonance in this regime since its g_{om} is very low. Region 3 denotes the regime above the mechanical cut-off frequency, where both the thermo-optic and optomechanical effects are too slow to follow the modulation signal. The high detuning in the even mode at the mechanical frequency ($6.7\ MHz$) is due to enhancement of the motion because of mechanical Q but is absent in the case of the odd mode due to its low g_{om}. (b) Normalized (to the maximum value of the individual resonance) line scans for even and odd cavity mode detunings in Region 2 and Region 3.The red and blue curves correspond to red and blue lines drawn in panel *a*. Smearing is observed for the even mode while it is absent for the odd mode, showing the prominence of optomechanical effect in Region 2.

due to optomechanical effects. The wavelength tuning is smaller in this region than in Region 1 which is consistent with our observations that at low frequencies thermal effects cause roughly four times more tuning than mechanical ones. Still, this tuning range is suitable for optical switching applications where it is sufficient to detune the cavity resonance off the wavelength of the optical data signal. Figure 4.3.8b shows the normalized line scans in Region 2 and Region 3 proving the existence of optomechanical effect for the even mode in Region 2 and the absence of any thermo-optical effect in either of the regions (as seen from the corresponding line scans for the odd mode). We note that, as expected at mechanical resonance the tuning range of the even mode is large, since the nanobeam motion is amplified by the mechanical Q ($Q_{mech} = 17$). Finally, in Region 3 the operating frequency is larger than mechanical cutoff frequency, and neither thermal nor optomechanical effects can keep up with the modulation, resulting in negligible tuning.

4.4 High Q Mode Pumping

We also used high-Q modes in order to actuate the beams and tune the resonant wavelength of the filters. The results of these experiments confirm the problems associated with using a high Q mode as pump, and show that broadband operation is not possible

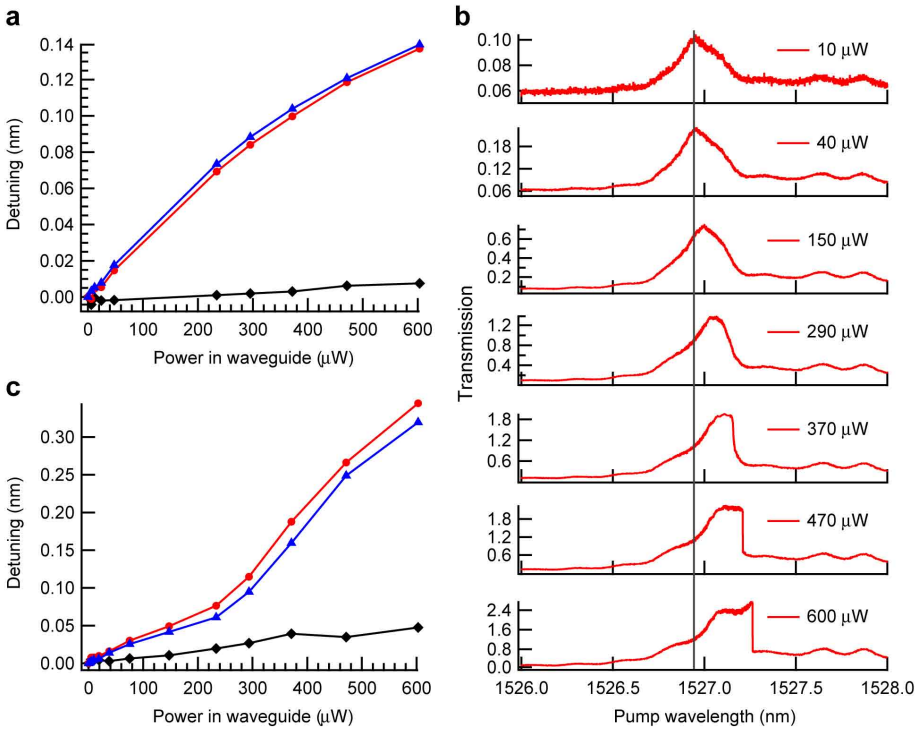

Figure 4.4.1: High Q cavity mode pumping. (a) even and odd mode detuning for various pump powers without pump mode tracking and locking. Filled red circles, filled blue triangles and filled black diamonds correspond to even mode detuning, odd mode detuning and even mode optomechanical detuning respectively. (b) Detuning of the pump mode for various pump powers. Self detuning of the pump mode is observed with increase in pump power. Bistable operation due to optical nonlinearity can be seen for power levels of $370\ \mu W$ and higher (c) even and odd mode detuning for various pump powers and with pump mode tracking and locking. The detuning achieved in this case is 2.5 times larger for the same power levels as compared to panel a. Filled red circles, filled blue triangles and filled black diamonds correspond to even mode detuning, odd mode detuning and even mode optomechanical detuning respectively.

without wavelength tracking and locking. These experiments were conducted on a different device but with comparable gap between the beams. The particular pump mode had a Q of ~ 5500. Figure. 4.4.1a shows the detuning of the even (1515.4 nm) and odd (1508.2nm) modes and the estimated optomechanical detuning as a function of input pump power (power inside the waveguide before the cavities). The pump wavelength was fixed at the maximum transmission point (at low pump powers) of the pump mode at 1526.96 nm. This wavelength corresponds to the 2nd even resonance of the structure. Comparing this with the detuning shown in Fig. 4.3.6b, we see that it requires about 3 times less power to achieve the same detuning when the device is excited with this particular high-Q mode. However, the tuning saturates at large input powers due to self-detuning of the pump mode. Figure 4.4.1b shows the transmission spectrum around the pump mode for various input pump powers. We can clearly see that the pump mode self-detunes towards longer wavelengths with increasing powers. In addition, strong thermo-optic nonlinearity can be observed due to two-photon absorption of Si. Finally, we employed a wavelength tracking and locking technique. The spectrum was measured at each power level, and the laser wavelength was locked to the new resonant wavelength. With this method, 2.5 times larger tuning (Fig. 4.4.1c) is achieved at the same input power levels when compared to Fig. 4.4.1a (no tracking and locking). Hence, in order to

achieve larger tunings the use of wavelength tracking and locking methods are required. The self-detuning has a larger effect at higher input powers, which is necessary for large tunings. The effects of bistability in our devices can be observed from Fig. 4.4.1b for pump powers above $370\,\mu W$. Bistability becomes a large problem for high-Q devices as the power required for bistable operation scales with $(1/Q^2)$. These results clearly illustrate that unless a track and lock method is employed, it is not a feasible choice to use high-Q modes for achieving large tunings in silicon devices.

4.5 Pumping using Broadband Source

In order to explore the possibility of operation using a broadband incoherent source, we pumped the device using a super luminescence diode (SLD) (Thorlabs S5FC1005SXL). The results from this experiment are shown in the inset of Fig. 4.5.1. The power coupled into the waveguide in this case is quite small due to the low saturation power available in the SLD and hence the total tuning is only of the order of $20\,pm$. The x-axis is the power coupled in to the waveguide (just before the photonic crystal) from the SLD source. However, the total SLD power is not a useful quantity to characterize the tuning, and power spectral density (which is much lower in the case of SLD when compared to a laser) would be much more appropriate.

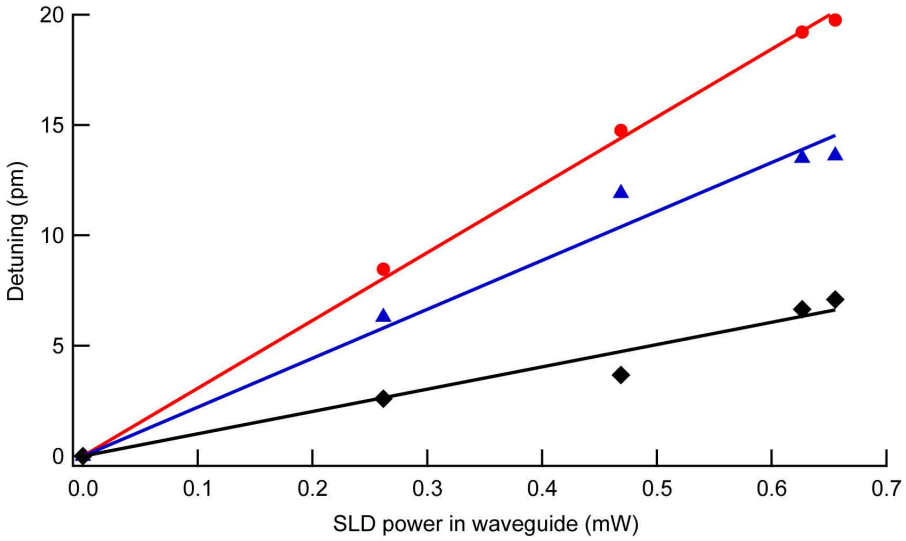

Figure 4.5.1: Broadband excitation using Super Luminescence Diode. The power coupled into the waveguide in this case is quite low due to the low saturation power available in the SLD and hence the total tuning is only of the order of $20\ pm$. The solid lines in this case are just for guidelines. Filled red circles, filled blue triangles and filled black diamonds correspond to even mode detuning, odd mode detuning and even mode optomechanical detuning respectively. The solid lines in the figure are only for guidelines.

Unfortunately, power spectral density of our SLD has large oscillations and is not constant across the spectrum, which makes quantitative comparison with laser excitation challenging. The solid lines in the figure are only for guidelines. However, the results prove that an incoherent broadband source actuation can be used to overcome the issues of wavelength tuning/tracking incase of laser actuation using high Q modes.

4.6 Dynamic Effects

The dynamical response of the system can be determined from the following system of coupled equations:

$$\frac{da_c}{dt} = i\Delta'_c a_c - \frac{\Gamma'_c}{2}a_c + \sqrt{\Gamma_c^{wg} s_c^{in}} \tag{4.19}$$

$$\frac{da_p}{dt} = i\Delta'_p a_p - \frac{\Gamma'_p}{2}a_p + \sqrt{\Gamma_p^{wg} s_p^{in}} \tag{4.20}$$

$$\frac{dT}{dt} = -\frac{T}{\tau_{th}} + c_{th} P_{abs}(|a_p|^2) \tag{4.21}$$

$$\frac{dN}{dt} = -\frac{N}{\tau_{fc}} + \frac{\beta_p |a_p|^4}{2\hbar\omega_p} \tag{4.22}$$

$$\frac{d^2x}{dt^2} + \Gamma_M \frac{dx}{dt} + \Omega_M^2 x = -\frac{g_{OM}^c |a_c|^2}{m_{eff}\omega_c} - \frac{g_{OM}^p |a_p|^2}{m_{eff}\omega_p} + F_L \tag{4.23}$$

Equation 4.23 is written within rotating-wave approximation [77]. Since a very weak probe beam ($0.1\mu W$) was used in our experiments, we have excluded the non-linear effects induced by the probe mode

from this model. These equations can be solved perturbatively using the following ansatz [78]:

$$a_c = \overline{a}_c + \delta a_c \tag{4.24}$$

$$a_p = \overline{a}_p + \delta a_p \tag{4.25}$$

$$T = \overline{T} + \delta T \tag{4.26}$$

$$N = \overline{N} + \delta N \tag{4.27}$$

$$x = \overline{x} + \delta x \tag{4.28}$$

where $(\overline{a}_c, \overline{a}_p, \overline{T}, \overline{N}, \overline{x}\ )$ are the solutions of the steady-state equations. In the perturbative limit, the general procedure to solve these equations is that ansatz 4.6 is substituted in eqns. 4.19-4.23, only the linear dynamical terms are kept, and finally $(\delta a_c, \delta a_p)$ are expressed in terms of δx and substituted in eqn. 4.23 [78]. In the limit of weak probe input and low-Q pump the solution can be simplified and the contribution of each mode can be added separately to the effective mechanical frequency:

$$\Omega_M^2 = \Omega_{M0}^2 - Re(A_0 + B_0), where \tag{4.29}$$

$$A_0 = -\frac{2\Delta_c'(g_{om}^c)^2|a_c|^2}{\omega_c m_{eff} f_c f_c'}, and \quad B_0 = -\frac{2\Delta_p'(g_{om}^p)^2|a_p|^2}{\omega_p m_{eff} f_p f_p'} \tag{4.30}$$

$$f_{c,p} \cong -i\Omega_{M0} - i\Delta_{c,p}' + \frac{\Gamma_{c,p}'}{2} \tag{4.31}$$

$$f_{c,p}' \cong -i\Omega_{M0} + i\Delta_{c,p}' + \frac{\Gamma_{c,p}'}{2} \tag{4.32}$$

$$\Delta_{c,p}' = \Delta_{c,p}^0 + g_{c,p}^{TH}\overline{T} + g_{c,p}^{FCD}\overline{N} + \chi^{c,p}|\overline{a_{c,p}}|^2 + \chi^{cp,pc}|\overline{a_{p,c}}|^2 - g_{OM}^{c,p}\overline{x} \tag{4.33}$$

$$\Gamma_{c,p}' = \Gamma_{c,p}^0 + \alpha_{c,p}\overline{N} + \beta_{c,p}|\overline{a_{c,p}}|^2 + \beta_{cp,pc}|\overline{a_{p,c}}|^2 \tag{4.34}$$

These equations and the effect of the strong pump can be understood in the following way. First, at low probe input powers without an excitation in the pump mode, we observe an optical spring effect. Once the pump mode is excited at a constant wavelength, it first detunes the probe mode, and reduces the energy stored in probe mode because of non-linear absorption (non-degenerate two photon absorption, and free-carrier absorption). Moreover, the pump mode contributes a constant term to the effective mechanical frequency (the pump wavelength is kept constant). Finally, as the pump power is increased there is a self-detuning effect, i.e. the pump mode detunes

itself.

We characterized the Brownian motion of the two free standing beams, in ambient conditions, by detuning the probe to the maximum slope of the cavity resonance (pt. A in Fig. 4.6.1 inset). Since the even mode of the coupled cavity system is extremely dispersive with respect to the gap between the beams, any motion of the beams is transduced onto the transmission of the cavity. This modulated transmission of the probe was analyzed using a spectrum analyzer and is shown in Fig. 4.6.1. Various in-plane and out-of-plane vibrational modes can be identified in the spectrum and their exaggerated motion along with the g_{om} is shown in Fig. 4.6.1. The fundamental in-plane mode which has the maximum g_{om} shows up as a very strong peak at $8\,MHz$. The second and third order in-plane modes can also be well resolved in the spectrum. We note that the peak at $16\,MHz$ does not correspond to any vibrational mode and is an artifact of nonlinear transduction (this was verified by the absence of the peak at $16\,MHz$ when probed using a low Q mode with comparable g_{om}).

We investigated this further by conducting similar experiment on a different sample with similar cavity dimensions (except with a slightly longer suspended length and larger separation $\sim 112\,nm$, $g_{om}\,38\,GHz/nm$). This measurement was done on a different sample since the one used to obtain the data in the main manuscript was

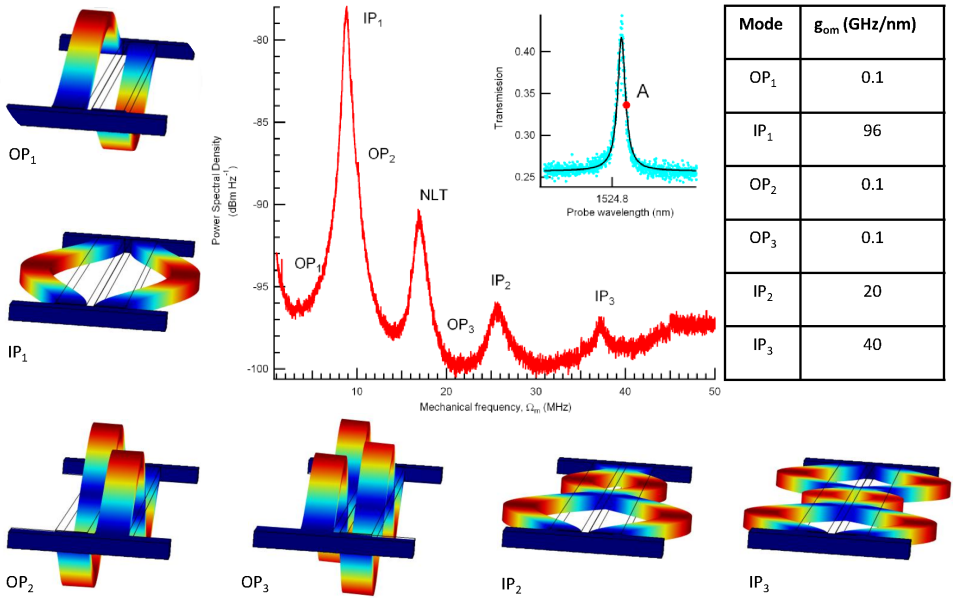

Mode	g_{om} (GHz/nm)
OP_1	0.1
IP_1	96
OP_2	0.1
OP_3	0.1
IP_2	20
IP_3	40

Figure 4.6.1: Noise spectrum showing the Brownian motion of coupled nanobeam cavities in air. The power spectral density spectrum shows the various mechanical modes of the nanobeams. The measured electrical noise floor was $-103\,dBm/Hz$ near $10\,MHz$.The peaks are labeled according to their mechanical deflection which can be in-plane (IP) or out-of-plane (OP). The inset shows the optical spectrum with operating point (pt A), corresponding to the maximum slope of the transmission resonance. The various vibrational modes were identified using FEM simulations. The nanobeam displacements have been exaggerated to show the vibrational motion of the beams. The most efficient transduction is obtained for fundamental in-plane mode IP_1. The peak at $16\,MHz$ does not correspond to any mechanical mode, but is a Fourier component due to nonlinear transduction. This happens when Brownian motion of the beams is large enough to detune the probe laser across the lorentzian line shape of the cavity resonance. In this case, the relation between optical transmission and gap is no longer linear around the operating point A. The table summarizes the g_{om} of various modes for a device with $70\,nm$ gap between the nanobeams.

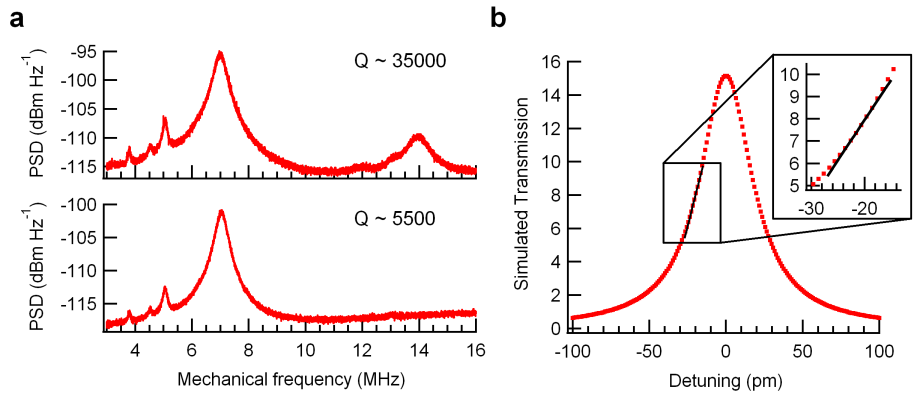

Figure 4.6.2: Non linear transduction. (a) Power spectral density spectrum transduced using a high Q and low Q optical mode. The $14\,MHz$ peak in the plot obtained using high Q (35000) mode is a Fourier component of the fundamental mode at $7\,MHz$. This was due to nonlinear transduction, which was confirmed by analyzing the signal transduced using a low Q (5500) optical mode. The g_{om} of both the optical modes were comparable ($38\,GHz/nm$ and $35\,GHz/nm$). (b) Simulated lorentzian lineshape. Brownian motion of the nanobeams results in $12\,pm$ of detuning around the operating point, which is plotted in black. Inset shows the deviation of the signal from a linear response for the above detuning.

unfortunately destroyed. The plot in Fig. 4.6.2a shows the PSD spectrum transduced using a high-Q (~ 35000) cavity optical mode. Using the equipartition theorem, we estimate that the Brownian motion of the beams gives rise to about 38 pm of motion. With the known gom (38 GHz/nm) this translates approximately 12 pm of change in wavelength. The HWHM of the probe resonance is 21 pm ($Q \sim 35000$). This change in wavelength due to motion results in nonlinear transduction of the signal.

The nonlinear transduction effect is illustrated in Fig. 4.6.2b, where the inset shows the deviation of the measured signal from a linear response due to lorentzian lineshape of the optical mode. This gives rise to the peak at 14 MHz which is a non-linear harmonic of the fundamental mode at 7 MHz The PSD spectrum transduced using a low Q optical mode ($Q \sim 5500$, g_{om} 35 GHz/nm) is also shown in Fig. 4.6.2a where the peak at 14 MHz is missing confirming the nonlinear transduction in the earlier case. Similarly, the resonance at 16 MHz in Fig. 4.6.1 is a harmonic of the fundamental mode due to nonlinear transduction (g_{om} 96 GHz/nm, $Q \sim 25,000$). The effect in this sample is more pronounced due to small nanobeam gap resulting in higher g_{om}.

Fig. 4.6.3a plots the effect of probe detuning on the resonant frequency of the fundamental, mechanical, in-plane mode. The blue curve shows the optical transmission spectrum of the even mode while

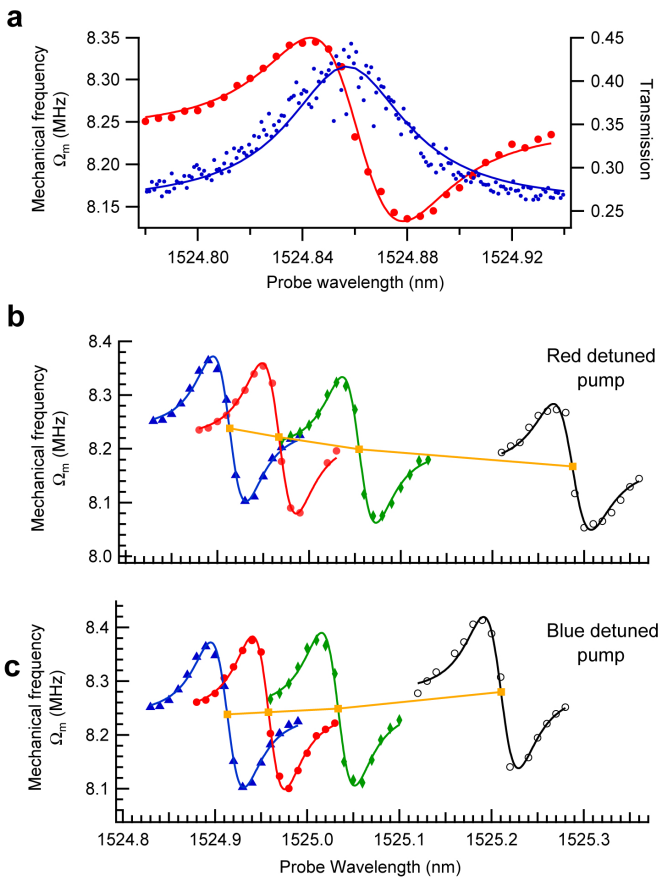

Figure 4.6.3: Dynamic optomechanical effects. (a) Mechanical response of the fundamental in-plane mechanical mode IP_1 - (filled red circles) for various detuning of the probe mode (blue dots) at zero pump power. This effect is due to self stiffening of the nanobeams due to large optical energy stored inside the cavities. The solid red line is the fit given by Eqn. 4.6 and the solid blue line is a lorentzian fit for the optical mode. (b) The shift in mechanical response shown in panel b for various pump power at two different pump detuning. The red detuned pump was set at $1570.5\,nm$, while the blue detuned pump was set at $1573.5\,nm$. The mechanical response moves towards lower frequencies for red detuning and towards higher frequencies for a blue detuned pump. The filled blue triangles, filled red circles, filled green diamonds and the unfilled black circles correspond to $0\,mW$, $0.75\,mW$, $1.6\,mW$ and $3.3\,mW$ of pump power respectively and the corresponding solid lines are the fits given by equation 2. The filled yellow squares represent the mechanical frequency of the probe without self-stiffening from the probe. The solid yellow line is drawn as a guide to the eye.

the red curve plots the detuning of the mechanical resonance for various probe detuning. Since the device operates in the sideband unresolved limit ($\Omega_M << \text{optical } Q$), the response is only due to optical stiffening [1] which is given by Eqn. 4.6. Fig. 4.6.4 confirms this as we do not observe any broadening or narrowing of linewidth signifying cooling and amplification respectively.

Apart from the self-stiffening effect due to the probe mode as seen in Fig. 4.6.3a, stiffening can also be induced by the pump. This effect is studied by pumping at either side of the broad pump mode. As the power in the pump mode is increased the mechanical resonance of the device is detuned due to stiffening. The sign of this mechanical resonance detuning is dependent on the detuning of the pump laser with respect to the pump resonance (Fig. 4.6.3b). For a red-detuned pump the beams are softened and the mechanical resonance frequency decreases, while blue detuning results in an increase of the mechanical frequency. The smooth curves show the fits using Eqn. 4.6 taking into account the presence of the pump. Therefore, our approach allows us to independently control, the optical and mechanical frequencies of our optomechanical filters. This would be of relevance in applications like optical accelerometers where there would be a need to vary the mechanical stiffness to improve the dynamic range and at the same time bias the optical mode at the operating laser wavelength.

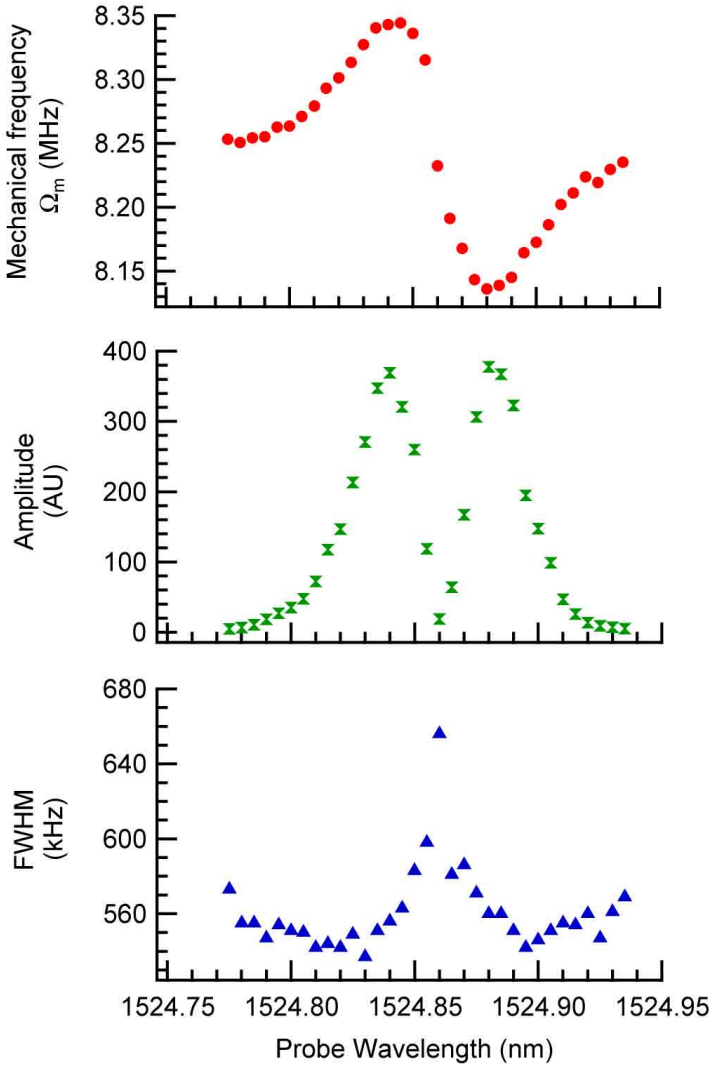

Figure 4.6.4: Optical spring effect for various probe detunings. The fundamental mechanical mode frequency, amplitude and linewidth (full width half max (FWHM)) for various optical detunings of the probe mode. The change in mechanical frequency of the fundamental mode is due to optical spring effect. No parametric instability was observed for the power levels used in this work. Furthermore, thermal instabilities were also absent. No appreciable cooling (broadening of the linewidth) and amplification (narrowing of the linewidth) was observed for red/blue detuning of the probe mode.

Table 4.6.1: Simulation Parameters

Quantity	Value	Unit	Ref
β_{Si}	7.9×10^{-12}	m/W	[79]
V_c^{TPA}	5.81×10^{-19}	m^3	
V_p^{TPA}	4.96×10^{-19}	m^3	
$V_{cp,pc}^{TPA}$	3.18×10^{-18}	m^3	
$V_c^{cc,FCA}$	2×10^{-37}	m^3	
$V_c^{pp,FCA}$	5×10^{-36}	m^3	
$V_c^{cp,FCA}$	1.3×10^{-36}	m^3	
$V_p^{cc,FCA}$	1.3×10^{-36}	m^3	
$V_p^{pp,FCA}$	2.37×10^{-36}	m^3	
$V_p^{cp,FCA}$	5×10^{-36}	m^3	
$\Delta'_{c,p}$	90	GHz	
σ_{Si}	1.45×10^{-21}	m^2	[70]
$n_{2,Si}$	5×10^{-18}	m^2/W	[79]
$\zeta_{Si,e}$	8.8×10^{-28}	m^3	[80, 81]
$\zeta_{Si,h}$	1.45×10^{-29}	m^3	[80, 81]
dn_{Si}/dT	1.86×10^{-4}	K^{-1}	
τ_{fc}	2.2×10^{-9}	s	
m_{eff}	3.059×10^{-15}	kg	
g_{om}^c	96×10^9	GHz/nm	
$R_{c,p}^{th}$	1.17×10^6	K/W	
Q_{abs}	1×10^6		
Q_c	2.5×10^4		
Q_p	3.6×10^2		

4.7 Conclusion

Our devices are fully integrated and made in technologically relevant silicon-on-insulator platform. This comes at an expense of significant two-photon absorption induced thermo-optic effects. Using an on-chip temperature sensing scheme, we successfully elucidate the interplay between optomechanical and thermo-optic effects on the tunability of the silicon based optomechanical filters. We demonstrated that optomechanical effects dominate the thermal ones when the structure is operated at frequencies higher than its thermal cut-off frequency. This is of practical importance for applications in all-optical circuit switching and packet routing. Furthermore, for these applications it is sufficient to detune the resonance of the cavity for a few linewidths only in order to get it off resonance with incoming optical signal.

In conclusion, we demonstrated an all-optical tunable filter employing coupled photonic crystal nanobeam cavities, where a considerable portion of the tuning is affected by mechanical reconfiguration. Specifically, we measured a total tuning of filter resonance of more than 18 line-widths out of which 20 % was due to optomechanical effects. As demonstrated, optomechanical tuning effects are much faster than the thermal ones in our system which is important for practical applications. The operating speed of optomechanical devices could be pushed into the GHz regime by

using smaller and stiffer structures, at the expense of increased optical power needed to actuate them. Our scheme allows for a wide range of pump wavelength selection while overcoming the limitation of self-detuning of the pump and can be used to simultaneously control multiple devices. At the same time, independent control over the mechanical response was also achieved by varying the pump laser s wavelength. Our technique is a promising candidate for realization of reconfigurable and programmable optical devices, including filters and filter banks, routers, and modulators.

Coherent light and mind

will continue to revolutionize science

5

Outlook and Future Work

In times to come, it will be clear to what extent photonic devices can replace electronic devices and form an inherent part of the current integrated circuits technology. Much will depend on the speed of operation, robustness, long period drifts, and system integration and packaging of the devices. Photonic crystal nanobeam cavities

have the potential to fulfill the above requirements and form a building block for achieving on-chip interconnect components for switching and signal routing applications. In the earlier chapters, we have seen that PCNCs are compatible to traditional reconfiguration techniques using thermo-optic and electromechanical effects. Along with the above techniques, they can also be reconfigured using optomechanical effects which allows for faster operational speeds and higher density of devices. Hence, PCNCs are good candidates for achieving reconfigurable photonic devices, which make them suitable for switching applications. Apart from this, PCNCs can also prove to be useful in applications in biochemical analysis due to their easily accessible, ultra high Q modes, enabling stronger light matter interaction.

Optomechanical reconfiguration opens the door for some interesting fundamental research [82, 83] and engineering applications. They serve as an excellent platform to conduct experiments to achieve ground state cooling and study exciting phenomenon like electromagnetically induced transparency [83, 84]. On the engineering front, optomechanical reconfiguration opens up new areas of applications in radio frequency (RF) photonics. Fig. 5.0.1 shows an image of a integrated system where the coupled cavities are reconfigured using dielectrophoretic force. The inset shows the suspended cavity region between two gold electrodes. Using this

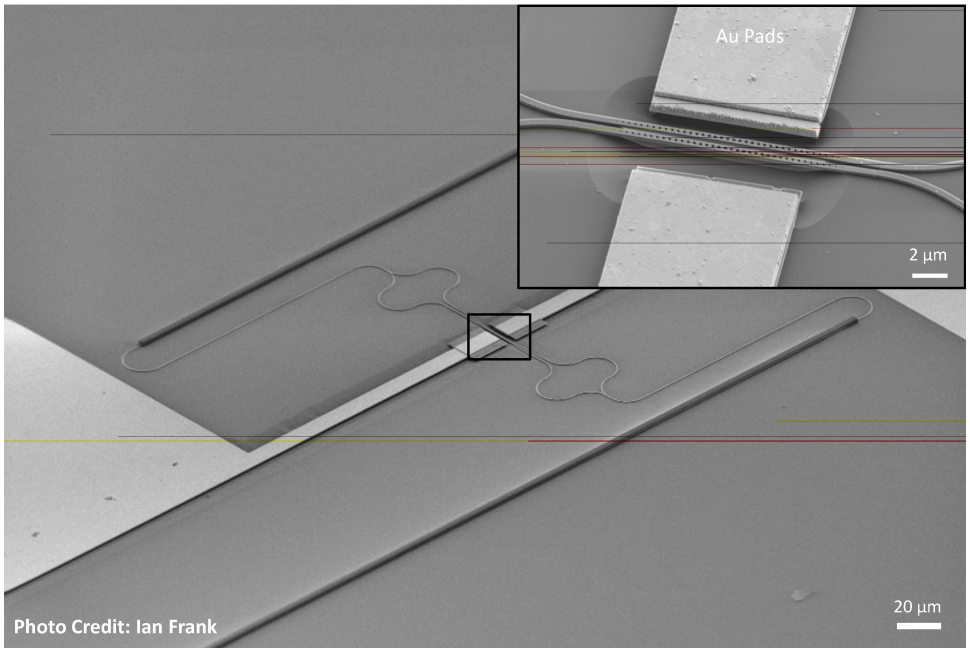

Figure 5.0.1: Reconfiguration of nanobeam cavities using dielectrophoretic force. SEM image of the fabricated device. Inset shows the suspended cavity region with the gold electrodes

technique, RF fields can be used to modulate optical signals by mechanically deforming dielectric materials. This technique overcomes the limitations for high contact resistance and does not require doping of the devices (hence maintaining high Q)

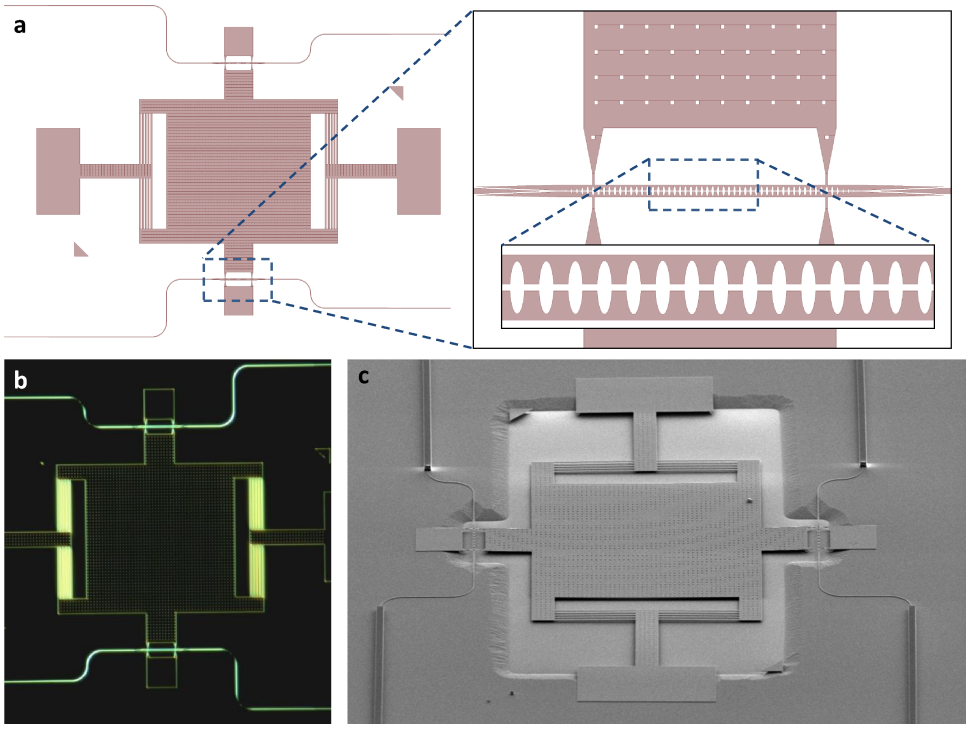

Figure 5.0.2: Accelerometer using nanobeam cavities. (a) Schematic of the optical readout accelerometer. The PCNCs are attached to the large central motion mass, included to increase motion sensing. Insets show the modified PCNCs design to help improve the g_{om} of the device.

Nanobeam optomechanical systems will also be useful in applications related to motion sensing, for example, accelerometers and gyroscopes. Fig. 5.0.2a shows a possible design for an optical accelerometer. The motional mass of PCNCs is extremely small which

limits the detection of acceleration. Hence, PCNCs need to be mechanically attached to a larger mass as shown in the figure to increase motional sensitivity. The insets show the PCNC region with a modified design of nanobeam cavities. The design is adopted to improve the sensitivity of the device (by increasing the g_{om}). The field in this case, is more localized in the gap allowing for a 2 fold improvement in the g_{om} values as compared to the devices used in Chapter 4. Figure 5.0.2b shows an optical image of the fabricated structure while Fig. 5.0.2c shows a SEM image of the final released device. The multiple beam supports are designed to release the in-plane compressive stress in the silicon device layer. Such accelerometers based on optical readouts, are free from electromagnetic interference which is a major concern of failure in applications related to defense and automobiles. Overall, photonic crystal nanobeam cavities will not only prove to be useful for fundamental research but may also find their way into engineering applications.

A

First Appendix

A.1 Fabrication Procedure

A.1.1 Procedure 1 (used for non waveguide structures)

The devices were fabricated on a SOI substrate with a silicon device layer of 220 nm and a buried oxide layer of 2 μm. The patterns were

written using negative ebeam resist $FOx-12$ with a $100\,keV$ ebeam lithography tool. The patterns were then transferred to silicon using ICP-RIE. A HF vapor etch technique was used to etch the sacrificial oxide layer to release the structures.

A.1.2 Procedure 2 (used for waveguide structures)

The devices were fabricated on a SOI substrate with a silicon device layer of $220\,nm$ and a buried oxide layer of $3\,\mu m$. The patterns were written using negative ebeam resist XR-1451-002 with a $100\,keV$ ebeam lithography tool at Cornell Nanofabrication facility to avoid stitching errors (write field of 1 mm) and the use of proximity correction, as it was necessary in order to achieve correct hole sizes at narrow waveguide gaps. The patterns were then transferred to silicon using ICP-RIE. SU-8 polymer coupling pads were then written on each end of the device to couple light in and out of chip. Shipley $1813S$ photoresist was then spun on the sample and only the region over the silicon waveguides was exposed. The remaining resist over the waveguides was then removed by dipping the sample in $7:1$ BOE for 1 minute. The sample was then cleaved through the SU8 pads and another photolithography step was carried out to open the small window to suspend the nanobeam photonic crystal cavities (PCNC). The cavities were under-etched using $7:1$ BOE and then dried in a critical point dryer.

A.2 Fabrication Steps

A.2.1 Patterns for ebeam lithography

All the patterns were drawn in DesignCAD. For structures written using HSQ without proximity correction, and developed in high concentration TMAH (25 %), the pattern dimensions had to be biased in order to obtain the correct dimensions. The waveguide dimensions were increased by 10 % while the holes were reduced by 15 %.

A.2.2 Sample preparation for ebeam lithography

Steps for sample preparation:

- 5 minutes ultrasonication in IPA.
- 5 minutes ultrasonication in Acetone.
- 10 minutes Piranha Clean ($H_2SO_4 : H_2O_2 = 3 : 1$). Piranha solution is prepared by first mixing 1 part of hydrogen peroxide in 3 parts of Sulphuric acid. Hydrogen peroxide should be added slowly to the acid.
- Rinse in deinonized (DI) water
- 20 minutes bake on hot plate at 180 $^{\circ}C$
- 1 minute clean in O_2 plasma cleaner
  ($O_2 : 20\ sccm, Power : 70\ W$)

- Spin $XR-1451-006$ $(FOx-12, FOx-16)$ immediately at $4000\,rpm$
- 5 minutes bake at $90\,^{\circ}C$

A.2.3 Ebeam Lithography (ELS-7000)

The beam current and dosages for different patterns are summarized in Table. A.2.1. The patterns written using ELS-7000 were developed in 25 % Tetramethylammoniumhydroxide (TMAH) for $14\,s$ and thoroughly rinsed in DI water. It is important that the rinsing and blow drying process is gentle, as the adhesion of the ebeam resist with silicon is poor.

Table A.2.1: Ebeam Lithography Parameters (Elionix)

	Chip Size $(\mu m \times dots)$	**Current** (pA)/ **Dose** $(\mu C/cm^2)$
Nanobeams	$150 \times 60,000$	$100/(1000-1200)$
Waveguide Coupled Nanobeams	$300 \times 60,000$	$100/(1200-1600)$
SU-8 Waveguide	$600 \times 60,000$	$40/(10-12)$

A.2.4 Reactive Ion Etching (STS ICP RIE)

A 6" silicon wafer was used as a carrier. Thermal paste (AOS 340 WC) was used to achieve good thermal contact between the sample and the carrier. Two recipes were developed for etching silicon

(*Recipe*1) and silicon - silicon oxide stack (*Recipe*2). Before etching the patterns the chamber was cleaned using 'O_2 clean' recipe for 20 minutes. Then *Recipe*1 was run for 10 minutes to precondition the chamber. A small silicon and silicon oxide piece patterned with a small drop of photoresist as a mask was etched for 2 minutes using *Recipe*1. The sample as then cleaned and the etch depth was measured using a profilometer. The exact etch rate was calculated and the time required to etch 210 nm of silicon was noted. The actual etching process of the sample as carried out in three steps. The first step was a 5 s descum to remove any undeveloped resist from the pattern. The second step was carried out using *Recipe*1 for the time calculated to etch 210 nm of silicon. A final step using *Recipe*2 was carried out for an additional 25 s. This third step was necessary to prevent undercutting of silicon due to high selectivity of *Recipe*1 to oxide. The etching parameters for the two recipes are summarized in table A.2.2 and table A.2.3.

Table A.2.2: Recipe 1

Gas	**Value**
C_4F_8	80 $sccm$
SF_6	130 $sccm$
Platten Power	12 W
RF Power	1000 W

Table A.2.3: Recipe 2

Gas	Value
C_4F_8	30 $sccm$
SF_6	65 $sccm$
H_2	15 $sccm$
Platten Power	17 W
RF Power	1000 W

A.2.5 HF VAPOR ETCH

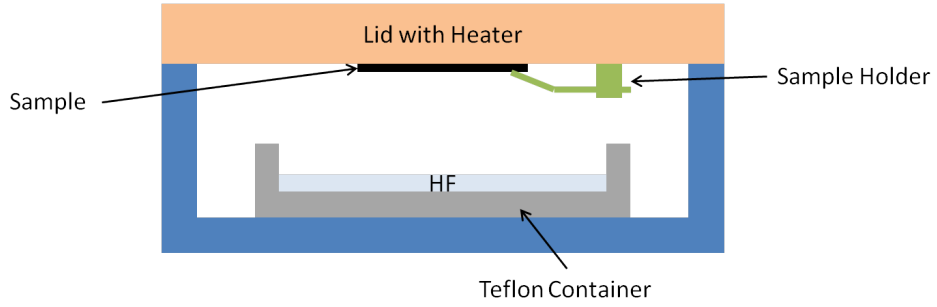

Figure A.2.1: Schematic of the HF vapor etching tool. It primarily consists of a closed chamber with a Teflon container for HF. The lid of the chamber is fixed with a heater to control the sample temperature.

HF vapor etching technique was used to remove the sacrificial layer (SiO_2) for the non-waveguide structures. Under proper operating condictions, this process completely avoids stiction and has a very high yield rate.

The etching chemistry is as follows:

$SiO_2 + 2H_2O \rightarrow Si(OH)_4$

and

$Si(OH)_4 + 4HF \rightarrow SiF_4 + 4H_2O$

We see that water is involved as a reactant as well as a resulting product. It is required to start the initial reaction, which means that the surface to be etched must have some amount of water to begin with. $Si(OH)_4$ then reacts with HF to form SiF_4 which is extremely volatile and water. This complicates the situation a bit. If too much of water is left on the surface then the release process is no more in vapor phase and the structure collapses due to stiction. An easy way to avoid this is to heat the substrate to evaporate the water. However, excessive heating of the substrate can result into reduced etch rate or no etching at all. Hence, it is important to control the temperature of the sample to achieve a desired etch rate along with vapor phase etching. The best etching was achieved for substrate temperatures of $34 - 35\,^{\circ}C$ with relative humidity around 40%. Typical etch rates achieved were $\sim 150\,nm/min$.

A schematic of the commercially available HF vapor etching (AMMT) apparatus used for the fabrication is shown in Fig. A.2.1. It consists of a container with an air tight lid. The lid consists of a silicon wafer which is heated by an underlying resistive heater. The sample is clamped on the silicon substrate holder. The temperature of the substrate can be precisely controlled within $0.1\,^{\circ}C$ using the control unit of the apparatus.

48% concentrated HF is poured into the Teflon container and the HF vapors resulting from room temperature evaporation are utilized

for etching. The sample is clamped on the substrate holder and the required temperature is set using the control unit depending on the room temperature. Once the desired temperature is reached, the etching process is initiated by placing the lid is over the HF container. The only way to stop the process is by removing the lid and placing it away from the HF vapors. The sample is monitored from time to time to avoid over etching of the sample.

A.2.6 Polishing

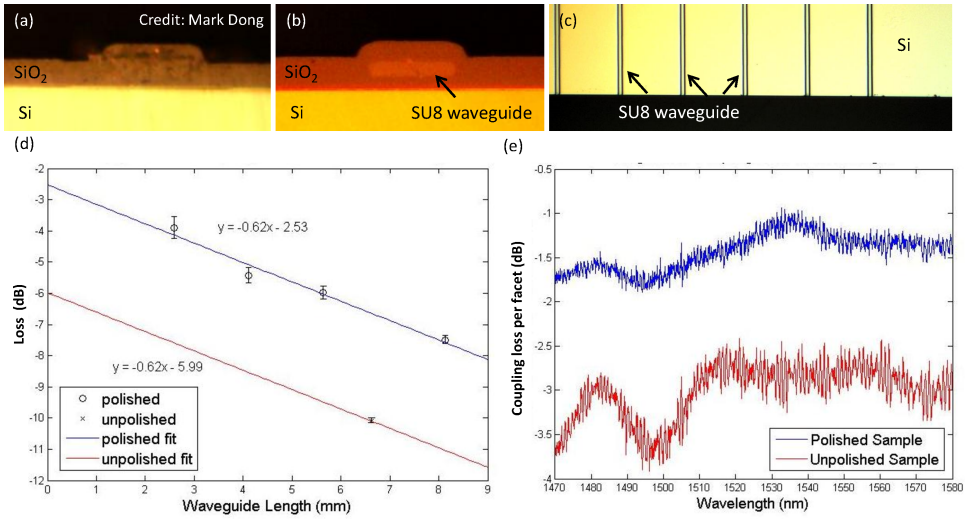

Figure A.2.2: Device facet polishing for efficient fiber-waveguide coupling. Optical images of the end facets before (a) and after (b) polishing process. (c) Top view of the edge of a polished facet. (d) Coupling and propagation loss characterization using cut-back method. (e) Coupling loss per facet over S, C and L band

The insertion losses for the waveguide coupled devices can be significantly improved by polishing the facets of the samples.

Polishing also helps prevent scrambling of the polarization of light while coupling light from the fiber to the SU-8 waveguide. Polishing was carried out on a standard polishing tool (Allied High Tech) consisting of a rotating polishing table with various grades of lapping paper. Prior to polishing, the sample were capped with a $2\mu m$ layer of PECVD SiO_2. This capping is necessary to prevent chipping of the SU-8 waveguides. A photoresist layer is then spun on the sample to protect the sample from the polishing residue. The sample is then cleaved through the SU-8 waveguides and mounted on the sample holder using crystal bond. Polishing is carried out by moving the sample in a figure '8' motion path on the rotating polishing table, keeping in mind that the waveguide surface forms the leading edge to rotating lapping paper. The various papers and the respective polishing time is summarized in the table A.2.4.

Table A.2.4: Polishing steps for Silicon Carbide (SiC) and Aluminium Oxide (Al_2O_3) abrasives

Paper	**Time**	**Rotation Speed**
400 grit SiC ($25\mu m$)	Until edge is flat	$70\,rpm$
800 grit SiC ($6.5\mu m$)	2 minutes	$70\,rpm$
1200 grit SiC ($2.5\mu m$)	2 minutes	$70\,rpm$
1 micron Al_2O_3	$8-10$ minutes	$70\,rpm$
0.3 micron Al_2O_3	3 minutes	$70\,rpm$
0.05 micron Al_2O_3	3 minutes	$70\,rpm$

Figure A.2.2a and b show the optical image of the facet before and after the polishing process. A distinct difference in the polished

surface can be seen. (It should be noted that the images correspond to $SU-8$ waveguides with cross section of $3\mu m \times 5\mu m$, slightly wider than those used in experiments). Figure A.2.2c shows the same facet when seen from top of the sample. Figure A.2.2d plots the total loss through waveguides with polished end facets for various lengths. The intersection of the linear fit with the y-axis gives the total insertion loss of the device of $2.5\,dB$ ($1.25\,dB/facet$). The slope of the line gives the propagation loss of the waveguide. The graph also plots data for one waveguide with unpolished facets. Since the propagation loss of the waveguide remains constant, we fit a line through the measured data point, with the slope obtained from the measurement of polished facets and estimate the insertion loss to be $6\,dB$ ($3\,dB/facet$). This data shows more than 2 times improvement in the coupling efficiency for the polished facets when compared to unpolished facets.
Figure A.2.2e plots the loss per facet over the S, C and L band.

B

Second Appendix

B.1 Characterization

B.1.1 Resonant Scattering

Single and coupled nanobeam cavities were probed using cross polarization technique popularly known as resonant

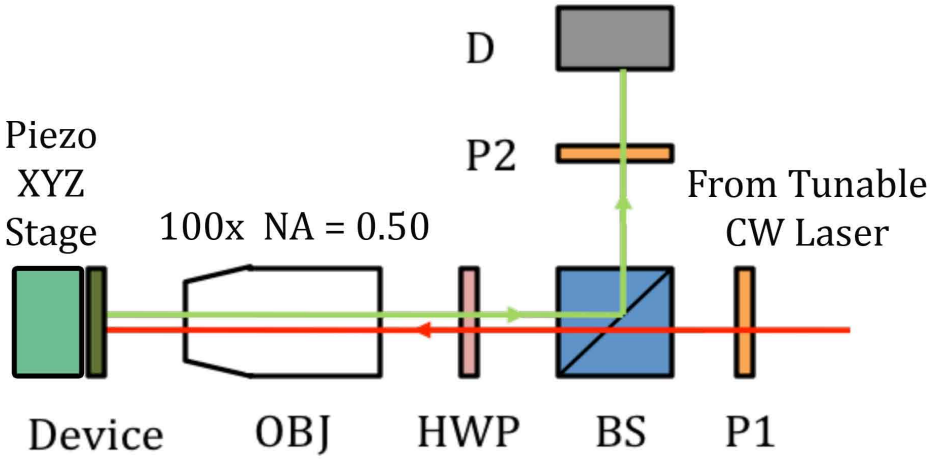

Figure B.1.1: Schematic of resonant scattering experimental setup. (OBJ: microscope objective, HWP: half-wave plate, BS: beamsplitter, P1 and P2: polarizers, D: detector)

scattering [85, 86]. Fig. B.1.1 shows the schematic of the setup. Prior to entering the objective lens (OBJ), the polarization of the incident laser beam is rotated by 45° using a half-wave plate (HWP), so that the E-field of the focused laser spot and the major component of the cavity mode (Ey) form a 45° angle. Light coupled in and subsequently re-emitted (backscattered) by the cavity is collected using the same objective lens, and then its polarization is rotated by −45° after passing through the same HWP. The backscattered signal is then split using a beam splitter (BS), analyzed using a polarizer (P2) that is cross polarized with respect to the polarization of the incoming laser beam, and finally detected using an InGaAs detector. This combination of polarizers and wave plates enhances the ratio between

the resonantly scattered signal from the cavity, and the coherent background due to nonresonant reflections. The spectra are normalized by a nonresonant background taken away from the cavity. Because of the coherent relationship of the scattered signal to the background, resonances appear as dips or peaks (depending on the geometry) and can have an asymmetric Fano lineshape depending on the relative phase of the scattered signal. In this scheme, the cavity plays the role of a wavelength selective polarization rotator. This experimental approach therefore allows for resonant spectroscopy of the cavity and does not require integration of additional waveguides to couple light in and out of the cavity. Therefore, this method measures the intrinsic Q factor of the cavity without "loading" effects due to the presence of coupling waveguides.

B.1.2 Butt Coupling

Figure B.1.2 shows the setup used for characterizing the devices using butt coupling method. This technique was used to characterize waveguide coupled devices. Light was coupled using PM tapered lensed fiber (Oz optics, NA $0:4$) into the SU-8 waveguide (refer Fig. B.1.3). An inverse taper geometry was used as a mode-size converter to efficiently couple the light from SU-8 waveguides into the silicon waveguides [87]. This was necessary due to the mode size mismatch between the fiber and the silicon waveguide. SU-8

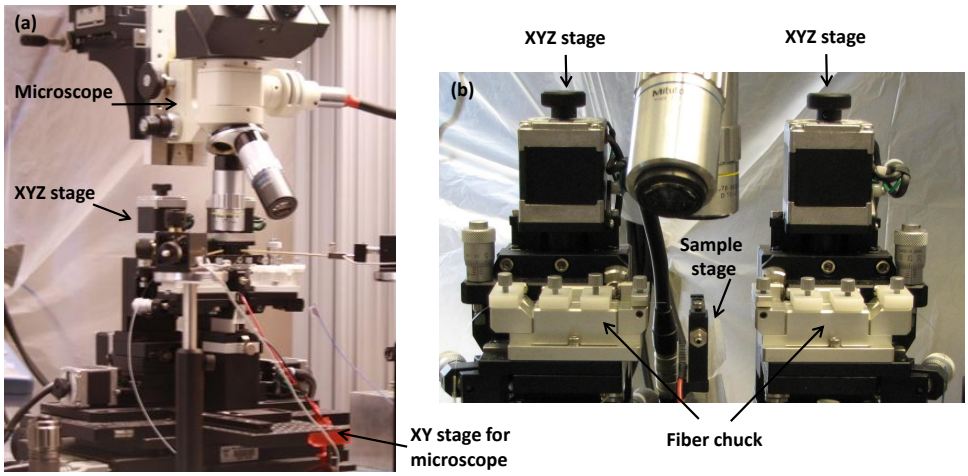

Figure B.1.2: Setup for characterization using butt coupling technique.(a) Setup used for characterization of devices using butt coupling technique. (b) Zoomed image showing the XYZ stages, sample stage, fiber chuck and the tapered lensed fiber.

waveguides had significantly larger cross section dimensions ($3 \times 3\,\mu m$) when compared to silicon waveguides ($440\,nm$ by $220\,nm$) which allowed for efficient coupling between the fiber mode and the SU-8 waveguide mode. At the output, a similar coupling method was used except the light was collected with a SM tapered lensed fiber (refer Fig. B.1.3b) (SM tapered fibers have lower taper conversion loss).

The propagation loss of the silicon waveguides and the maximum bend loss for $10\,\mu m$ bend radius were measured to be $4.5\,dB/cm$ and $1.0\,dB$, respectively. The measurement was carried out by imaging the light scattered from the waveguide from top with a sensitive IR camera (Fig. B.1.4). The slope of the linear fit on the scattered intensity obtained from the image gives the propagation loss in the

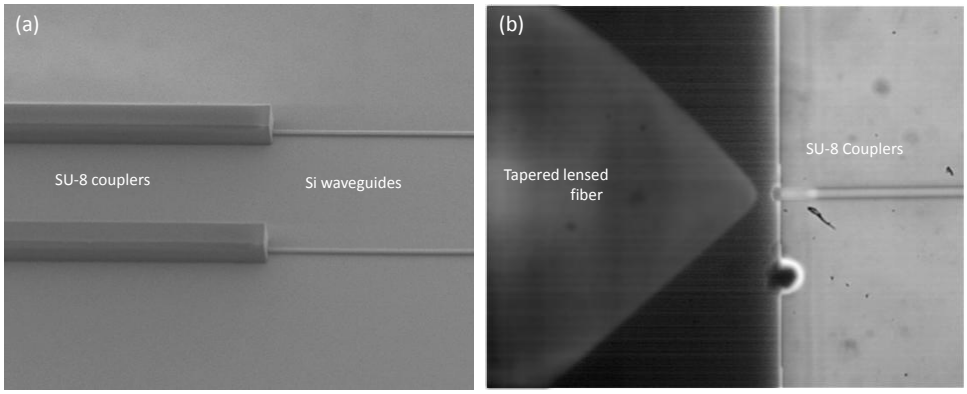

Figure B.1.3: Inverse taper geometry based mode converters for efficient broadband coupling. (a) SEM image of the mode converter showing SU-8 coupler and Si waveguides (b) Optical micrograph of the cleaved facet of the silicon chip showing the tapered lensed fiber and the SU-8 coupler

waveguides. The effect of stitching errors associated with ebeam lithography is also apparent from Fig. B.1.4. The SU-8 waveguide propagation loss was measured with the same method and found to be $7\,dB/cm$. This is likely due to the excitation of higher order modes of the SU8 waveguides that are less confined and prone to higher losses. By measuring the insertion loss for the waveguide samples and using the measured propagation losses of the waveguides, we estimated the coupling loss associated with the spot-size converters to be $2 \pm 0.5\,dB$. This was further confirmed by reversing the input signal direction. The power in the waveguide just before the cavity was estimated using the above measured values of coupling and propagation losses and the known device dimensions. The energy stored inside the cavity (W) is determined by taking into account the total $Q(Q_t)$ and the waveguide coupling $Q(Q_c)$ for the particular mode: $W = 4Q_t 2P_{in}/(\omega_0 Q_c)$.

The devices were characterized using tunable lasers (Agilent 81682, Santec TSL-510) and a sensitive InGaAs detector (EO systems, $IGA-010-TE2-H$). For mechanical measurements, a fast InGaAs detector (Newport $1811-FC$) was used along with an external amplifier (Stanford Research Systems) before analyzing the signal using an electrical spectrum analyzer (Tektronix $RSA3003$). The pump laser signal was amplified using an L band $1\,W$ EDFA (Manlight). The EDFA output was filtered for ASE emissions using a tunable filter (Agiltron). The pump and probe signals were multiplexed and de-multiplexed using a WDM (Microoptics Inc).

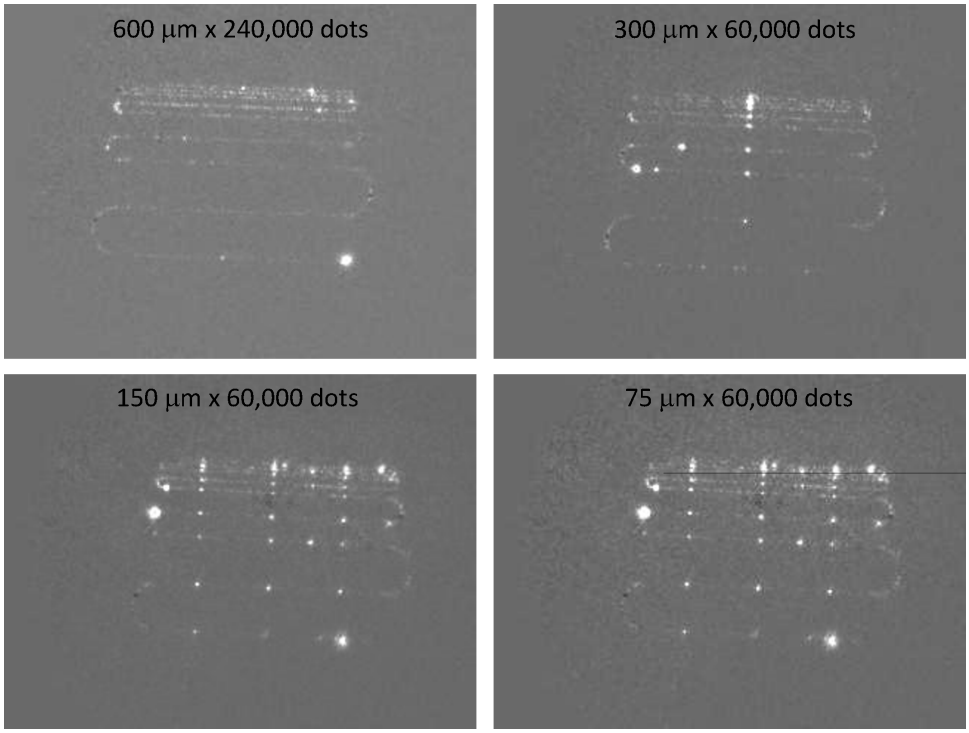

Figure B.1.4: Estimation of propagation loss in waveguides. Light scattering from silicon waveguides fabricated using different ebeam dot-pitch map. The waveguides were imaged from top using a sensitive IR camera. The slope of the linear fit on the scattered intensity gives the propagation loss in the waveguides. Scattering due to stitching errors during ebeam lithography is apparent from the periodic scattering centers.

References

[1] K. J. Vahala. Optical microcavities. *Nature*, 424(6950):839–846, 2003.

[2] Jun Pan, Yijie Huo, Kazuhiko Yamanaka, Sunil Sandhu, Luigi Scaccabarozzi, Rolf Timp, Michelle L. Povinelli, Shanhui Fan, M. M. Fejer, , and James S. Harris. Aligning microcavity resonances in silicon photonic-crystal slabs using laser-pumped thermal tuning. *Applied Physics Letters*, 92:103114, 2008.

[3] Iwan M rki, Martin Salt, Hans Peter Herzig, Ross Stanley, L. El Melhaoui, P. Lyan, and J. M. Fedeli. Optically tunable microcavity in a planar photonic crystal silicon waveguide buried in oxide. *Optics Letters*, 31(4):513–515, 2006.

[4] Fushman Ilya, Waks Edo, Englund Dirk, Stoltz Nick, Petroff Pierre, and Vuckovic Jelena. Ultrafast nonlinear optical tuning of

photonic crystal cavities. *Applied Physics Letters*, 90(9):091118, 2007.

[5] Murray W. McCutcheon, Andras G. Pattantyus-Abraham, Georg W. Rieger, and Jeff F. Young. Emission spectrum of electromagnetic energy stored in a dynamically perturbed optical microcavity. *Optics Express*, 15(18):11472, 2007.

[6] M. Eichenfield, R. Camacho, J. Chan, K. J. Vahala, and O. Painter. A picogram- and nanometre-scale photonic-crystal optomechanical cavity. *Nature*, 459(7246):550, 2009.

[7] M. Eichenfield, J. Chan, R. M. Camacho, K. J. Vahala, and O. Painter. Optomechanical crystals. *Nature*, 462(7269):78–82, 2009.

[8] M. Li, W. H. P. Pernice, and H. X. Tang. Tunable bipolar optical interactions between guided lightwaves. *Nature Photonics*, 3(8):464–468, 2009.

[9] A Schliesser, P Del'Haye, N Nooshi, KJ Vahala, and TJ Kippenberg. Radiation pressure cooling of a micromechanical oscillator using dynamical backaction. *Physical Review Letters*, 97(24):24390, 2006.

[10] GS Wiederhecker, L Chen, A Gondarenko, and M Lipson.

Controlling photonic structures using optical forces. *Nature*, 462(7273):633, 2009.

[11] M Li, WHP Pernice, C Xiong, M Baehr-Jones, Tand Hochberg, and HX Tang. Harnessing optical forces in integrated photonic circuits. *Nature*, 456(7221):480, 2008.

[12] J Roels, I De Vlaminck, L Lagae, B Maes, D Van Thourhout, and R Baets. Tunable optical forces between nanophotonic waveguides. *Nature Nanotechnolgy*, 4(8):510–513, 2009.

[13] Kippenberg T. J and Vahala K. J. Cavity optomechanics: Back-action at the mesoscale. *Science*, 321(5893):1172–1176, 2008.

[14] Y Li, JJ Zheng, J Gao, J Shu, MS Aras, and CW Wong. Design of dispersive optomechanical coupling and cooling in ultrahigh-q/v slot-type photonic crystal cavities. *Optics Express*, 18(23):23844–23856, 2010.

[15] E. Yablonovitch. Inhibited spontaneous emission in 3 dimensionally modulated periodic dielectric structures. *Journal De Physique*, 48(C-5):615–616, 1987.

[16] S. John. Strong localization of photons in certain disordered dielectric superlattices. *Physical Review Letters*, 58(23):2486–2489, 1987.

[17] John D. Joannopoulos, Steven G. Johnson, Joshua N. Winn, and Robert D. Meade. *Photonic Crystals:Molding the Flow of Light*. Princeton University Press, 2008.

[18] C. Sauvan, G. Lecamp, P. Lalanne, and J. P. Hugonin. Modal-reflectivity enhancement by geometry tuning in photonic crystal microcavities. *Optics Express*, 13(1):245–255, 2005.

[19] P. Velha, E. Picard, T. Charvolin, E. Hadji, J. C. Rodier, P. Lalanne, and D. Peyrad. Ultra-high q/v fabry-perot microcavity on soi substrate. *Optics Express*, 15(24):16090 –16096, 2007.

[20] A. R. M. Zain, N. P. Johnson, M. Sorel, and R. M. De la Rue. Ultra high quality factor one dimensional photonic crystal/photonic wire micro-cavities in silicon-on-insulator (soi). *Optics Express*, 16(16):12084–12089, 2008.

[21] M. W. McCutcheon and M. Loncar. Design of a silicon nitride photonic crystal nanocavity with a quality factor of one million for coupling to a diamond nanocrystal. *Optics Express*, 16(23):19136–19145, 2008.

[22] Chan Jasper, Eichenfield Matt, Camacho Ryan, and Painter Oskar. Optical and mechanical design of a zipper photonic crystal optomechanical cavity. *Optics Express*, 15(5):3802–3817, 2009.

[23] Q. M. Quan, I. B. Burgess, S. K. Y. Tang, D. L. Floyd, and M. Loncar. High-q, low index-contrast polymeric photonic crystal nanobeam cavities. *Optics Express*, 19(22):22191–22197, 2011.

[24] Y. Gong and J. Vuckovic. Photonic crystal cavities in silicon dioxide. *Applied Physics Letters*, 96(3):031107, 2010.

[25] S. Mandal, X. Serey, and D. Erickson. Nanomanipulation using silicon photonic crystal resonators. *Nano Letters*, 10(1):99–104, 2010.

[26] Q. M. Quan, P. B. Deotare, and M. Loncar. Photonic crystal nanobeam cavity strongly coupled to the feeding waveguide. *Applied Physics Letters*, 96(20):203102, 2010.

[27] Murray W. McCutcheon, Parag B. Deotare, Yinan Zhang, and Marko Lončar. High-q transverse-electric/transverse-magnetic photonic crystal nanobeam cavities. *Applied Physics Letters*, 98, 2011.

[28] P. R. Villeneuve, S. H. Fan, J. D. Joannopoulos, K. Y. Lim, G. S. Petrich, L. A. Kolodziejski, and R. Reif. Air-bridge microcavities. *Applied Physics Letters*, 67(2):167–169, 1995.

[29] J. S. Foresi, P. R. Villeneuve, J. Ferrera, E. R. Thoen, G. Steinmeyer, S. Fan, J. D. Joannopoulos, L. C. Kimerling, H. I.

Smith, and E. P. Ippen. Photonic-bandgap microcavities in optical waveguides. *Nature*, 390(6656):143–145, 1997.

[30] P. Lalanne and J. P. Hugonin. Bloch-wave engineering for high-q, small-v microcavities. *IEEE Journal of Quantum Electronics*, 39(11):1430–1438, 2003.

[31] M. Notomi, E. Kuramochi, and H. Taniyama. Ultrahigh-q nanocavity with 1d photonic gap. *Optics Express*, 16(15):11095–11102, 2008.

[32] B. H. Ahn, J. H. Kang, M. K. Kim, J. H. Song, B. Min, K. S. Kim, and Y. H. Lee. One-dimensional parabolic-beam photonic crystal laser. *Optics Express*, 18(6):5654–5660, 2010.

[33] Q. M. Quan and M. Loncar. Deterministic design of wavelength scale, ultra-high q photonic crystal nanobeam cavities. *Optics Express*, 19(19):18529–18542, 2011.

[34] Y. N. Zhang, M. W. McCutcheon, I. B. Burgess, and M. Loncar. Ultra-high-q te/tm dual-polarized photonic crystal nanocavities. *Optics Letters*, 34(17):2694–2696, 2009.

[35] McCutcheon M. W., Chang D. E., Zhang Y., Lukin M. D., and Marko Loncar. Broadband frequency conversion and shaping of single photons emitted from a nonlinear cavity. *Optics Express*, 17(25):22689–22703, 2009.

[36] Burgess I. B., Zhang Y., McCutcheon M. W., Rodriguez A. W., Abad J. B., Johnson S., and Loncar M. Design of an efficient terahertz source using triply resonant nonlinear photonic crystal cavities. *Optics Express*, 17(22):20099–20108, 2009.

[37] Marin Soljacic, Mihai Ibanescu, Steven G. Johnson, Yoel Fink, and J. D. Joannopoulos. Optimal bistable switching in nonlinear photonic crystals. *Physical Review E*, 66:055601, 2002.

[38] M. L. Povinelli, M. Loncar, M. Ibanescu, E. J. Smythe, S. G. Johnson, F. Capasso, and J. D. Joannopoulos. Evanescent-wave bonding between optical waveguides. *Optics Letters*, 30(22):3042–3044, 2005.

[39] M. L. Povinelli, Steven G. Johnson, Marko Loncar, Mihai Ibanescu, Elizabeth J. Smythe, Federico Capasso, and J. D. Joannopoulos. High-q enhancement of attractive and repulsive optical forces between coupled whispering-gallery-mode resonators. *Otpics Express*, 13(20):8286, 2005.

[40] Masaya Notomi, Hideaki Taniyama, Satoshi Mitsugi, and Eiichi Kuramochi. Optomechanical wavelength and energy conversion in high-q double-layer cavities of photonic crystal slabs. *Physical Review Letters*, 97:023903, 2006.

[41] M. A. Popovic, C. Manolatou, and M. R. Watts.

Coupling-induced resonance frequency shifts in coupled. *Optics Express*, 14(3):1208 –1222, 2006.

[42] K Srinivasan, PE Barclay, M Borselli, and O Painter. Optical-fiber-based measurement of an ultrasmall volume high-q photonic crystal microcavity. *Physical Review B*, 70(8):081306, 2004.

[43] Notomi M, Shinya A, Mitsugi S, Kuramochi E, and Ryu H. Waveguides, resonators and their coupled elements in photonic crystal slabs. *Optics Express*, 12(8):1551–1561, 2004.

[44] Zhixuan Xia, Ali Asghar Eftekhar, Mohammad Soltani, Babak Momeni, Qing Li, Maysamreza Chamanzar, Siva Yegnanarayanan, and Ali Adibi. High resolution on-chip spectroscopy based on miniaturized microdonut resonators. *Optics Express*, 19(13):12356–12364, 2011.

[45] Fukazawa T, Fumiaki Ohno, and Toshihiko Baba. Very compact arrayed-waveguide-grating demultiplexer using si photonic wire waveguides. *Jpn. J. Appl. Phys.*, 43:L673–L675, 2004.

[46] Momeni B., Hosseini E. S., Askari M., Soltani M., and A. Adibi. Integrated photonic crystal spectrometers for sensing applications. *Optics Communications*, 282(15):3168 –3171, 2009.

[47] *Silicon-on-Insulator Echelle Grating WDM Demultiplexers With Two Stigmatic Points*, volume 21, 2009.

[48] J. Song and N. Zhu. Design and fabrication of compact etched diffraction grating demultiplexers based on -si nanowire technology. *Electron Letters*, 44(13):816 –818, 2008.

[49] Kyotoku B. B. C., Chen L., and M. Lipson. Sub-nm resolution cavity enhanced microspectrometer. *Optics Express*, 18(1):102 –107, 2010.

[50] Gan F., Barwicz T., Popovic M.A., Dahlem M.S., Holzwarth C.W., Rakich P.T., Smith H.I., Ippen E.P., and Kartner F.X. Maximizing the thermo-optic tuning range of silicon photonic structures. *Photonics in Switching*, pages 67 – 68, 2007.

[51] Xiaodong Yang, Charlton J. Chen, Chad A. Husko, and Chee Wei Wong. Digital resonance tuning of high-q/vm silicon photonic crystal nanocavities by atomic layer deposition. *Applied Physics Letters*, 91:161114, 2007.

[52] Andrei Faraon, Dirk Englund, Douglas Bulla, Barry Luther-Davies, Benjamin J. Eggleton, Nick Stoltz, Pierre Petroff, , and Jelena Vuckovic. Local tuning of photonic crystal cavities using chalcogenide glasses. *Applied Physics Letters*, 92:043123, 2008.

[53] S. Mosor, J. Hendrickson, B. C. Richards, J. Sweet, G. Khitrova, H. M. Gibbs, T. Yoshie, A. Scherer, O. B. Shchekin, and D. G. Deppe. Scanning a photonic crystal slab nanocavity by condensation of xenon. *Applied Physics Letters*, 87:141105, 2005.

[54] Brett Maune, Marko Loncar, Jeremy Witzens, Michael Hochberg, Thomas Baehr-Jones, Demetri Psaltis, Axel Scherer, and Yueming Qiu. Liquid-crystal electric tuning of a photonic crystal laser. *Applied Physics Letters*, 85:360, 2004.

[55] M. C. M. Lee and M. C. Wu. Tunable coupling regimes of silicon microdisk resonators using mems actuators. *Optics Express*, 14(11):4703– 4712, 2006.

[56] M. Galli, S. L. Portalupi, M. Belotti, L. C. Andreani, L. O Faolain, , and T. F. Krauss. Light scattering and fano resonances in high-q photonic crystal nanocavities. *Applied Physics Letters*, 94(7):071101, 2009.

[57] C. Liu. *Foundations of MEMS*. (Prentice Hall, 2005.

[58] Q. P. Unterreithmeier, E. M. Weig, and J. P. Kotthaus. Universal transduction scheme for nanomechanical systems based on dielectric forces. *Nature*, 458(7241):1001 –1004, 2009.

[59] P. B. Deotare, M. W. McCutcheon, I. W. Frank, M. Khan, and

M. Loncar. High quality factor photonic crystal nanobeam cavities. *Applied Physics Letters*, 94(12):121106, 2009.

[60] I. W. Frank, P. B. Deotare, M. W. McCutcheon, and M. Loncar. Programmable photonic crystal nanobeam cavities. *Optics Express*, 18(8):8705–8712, 2010.

[61] BS Song, T Asano, Y Akahane, Y Tanaka, and S Noda. Multichannel add/drop filter based on in-plane hetero photonic crystals. *Journal of Lightwave Technology*, 23(3):1449–1455, 2005.

[62] Manolatou C and Lipson M. All-optical silicon modulators based on carrier injection by two-photon absorption. *Journal of Lightwave Technology*, 24(3):1433–1439, 2006.

[63] P. B. Deotare, M. W. McCutcheon, I. W. Frank, M. Khan, and M. Loncar. Coupled photonic crystal nanobeam cavities. *Applied Physics Letters*, 95(3):031102, 2009.

[64] Rakich Peter T., Davids Paul, and Wang Zheng. Tailoring optical forces in waveguides through radiation pressure and electrostrictive forces. *Optics Express*, 18(14):14439–14453, 2010.

[65] M Eichenfield, CP Michael, R Perahia, and O Painter. Actuation of micro-optomechanical systems via cavity-enhanced optical dipole forces. *Nature Photonics*, 1(7):416–422, 2007.

[66] RM Camacho, J Chan, M Eichenfield, and O Painter. Characterization of radiation pressure and thermal effects in a nanoscale optomechanical cavity. *Optics Express*, 17(18):15726–15735, 2009.

[67] GS Wiederhecker, S Manipatruni, S Lee, and M Lipson. Broadband tuning of optomechanical cavities. *Optics Express*, 19(3):2782–2790, 2011.

[68] ML Gorodetksy, A Schliesser, G Anetsberger, S Deleglise, and TJ Kippenberg. Determination of the vacuum optomechanical coupling rate using frequency noise calibration. *Optics Express*, 18(22):23236–23246, 2010.

[69] Fan SH, Suh W, and Joannopoulos JD. Temporal coupled-mode theory for the fano resonance in optical resonators. *Journal of Optical Society of America A - Optics Image Science and Vision*, 20(3):569–572, 2003.

[70] HS Rong, AS Liu, R Jones, O Cohen, D Hak, R Nicolaescu, A Fang, and M Paniccia. An all-silicon raman laser. *Nature*, 433:292–294, 2005.

[71] R. Dekker, N. Usechak, M. Forst, and A. Driessen. Ultrafast nonlinear all-optical processes in silicon-on-insulator waveguides. *Journal of Physics D - Applied Physics*, 40:R249–R271, 2007.

[72] M. Eichenfield, J. Chan, A. H. Safavi-Naeini, K. J. Vahala, and O Painter. Modeling dispersive coupling and losses of localized optical and mechanical modes in optomechanical crystals. *Optics Express*, 17:20078–20098, 2009.

[73] C. Kottke, A. Farjadpour, and S. G. Johnson. Perturbation theory for anisotropic dielectric interfaces, and application to subpixel smoothing of discretized numerical methods. *Physical Review E*, 77:036611, 2008.

[74] A. D. McConnell A. K. E. G. Thermal conduction in silicon micro and nanostructures. *Annual Review of Heat Transfer*, 14:129–168, 2005.

[75] W. J. Liu and M Asheghi. Thermal conduction in ultrathin pure and doped single-crystal silicon layers at high temperatures. *Journal of Applied Physics*, 98:123523, 2005.

[76] W. J. Liu and M. Asheghi. Thermal conductivity measurements of ultra-thin single crystal silicon layers. *Journal of Heat Transfer - Transactions of ASME*, 128(1):75–83, 2006.

[77] C. K. Law. Interaction between a moving mirror and radiation pressure - a hamiltonian-formulation. *Physical Review A*, 51:2537–2541, 1995.

[78] Claude Cohen-Tannoudji, Jacques Dupont-Roc, and Gilbert

Grynberg. *Atom-Photon Interactions: Basic Processes And Applications*. WILEY-VCH, 1998.

[79] Bristow Alan D., Rotenberg Nir, and van Driel Henry M. Two-photon absorption and kerr coefficients of silicon for 850-2200 nm. *Applied Physics Letters*, 90:191104, 2007.

[80] P. Barclay, K. Srinivasan, and O. Painter. Nonlinear response of silicon photonic crystal microresonators excited via an integrated waveguide and fiber taper. *Optics Express*, 13(20):801–820, 2005.

[81] R. A. Soref and B. R Bennett. Electrooptical effects in silicon. *IEEE Journal of Quantum Electronics*, 23:123–129, 1987.

[82] G Anetsberger, O Arcizet, QP Unterreithmeier, R Riviere, A Schliesser, EM Weig, JP Kotthaus, and TJ Kippenberg. Near-field cavity optomechanics with nanomechanical oscillators. *Nature Physics*, 5(12):909–914, 2009.

[83] S Weis, R Riviere, S Deleglise, E Gavartin, O Arcizet, A Schliesser, and TJ Kippenberg. Optomechanically induced transparency. *Science*, 330(6010):1520–1523, 2010.

[84] A. H. Safavi-Naeini, T. P. M. Alegre, J. Chan, M. Eichenfield, M. Winger, Q. Lin, J. T. Hill, D. E. Chang, and O. Painter. Electromagnetically induced transparency and slow light with optomechanics. *Nature*, 472(7341):69–73, 2011.

[85] Murray W. McCutcheon, Georg W. Rieger, Iva W. Cheung, Jeff F. Young, Dan Dalacu, Simon Frédérick, Philip J. Poole, Geof C. Aers, and Robin L. Williams. Resonant scattering and second-harmonic spectroscopy of planar photonic crystal microcavities. *Applied Physics Letters*, 87, 2005.

[86] H. Altug and J. Vuckovic. Polarization control and sensing with two-dimensional coupled photonic crystal microcavity arrays. *Optics Letters*, 30(9):982 –984, 2005.

[87] S. J. McNab, N. Moll, and Y. A. Vlasov. Ultra-low loss photonic integrated circuit with membrane-type photonic crystal waveguides. *Optics Express*, 11:2927–2939, 2003.